

Counter Rotating Open Rotor

Parametric source noise
model development

L. Klespe

Delft University of Technology



Counter Rotating Open Rotor

Parametric source noise model development

by

L. Klespe

to obtain the degree of Master of Science
at the Delft University of Technology,
to be defended publicly on Friday March 24, 2017 at 02:00 PM.

Student number: 4192117

Project duration: June 29, 2016 – March 24, 2017

Thesis committee: Prof. Dr. D. G. Simons, TU Delft, Committee Chair

Dr. Ir. A. Sahai, TU Delft, Supervisor

Dr. Ir. A. H. van Zuijlen, TU Delft

Dr. M. Snellen, TU Delft

This thesis is confidential and cannot be made public until December 31, 2017.

An electronic version of this thesis is available at <http://repository.tudelft.nl/>.

Abstract

Counter Rotating Open Rotors are a possible response to the demands of future aviation propulsion. Their benefit of low fuel consumption grants operation particularly for rising kerosene price. Detrimental is the high level of noise emission, especially tonal sound. For prospective development and implementation to modern aviation, noise prediction tools are essential.

Delft University of Technology currently develops an automated aircraft design tool, which considers different disciplines. One of which is the noise prediction tool called INSTANT, already capable to predict noise emissions of turbofan engines. This thesis report presents and explains the development of an in-design noise prediction tool for Counter Rotating Open Rotors as a starting point for an advancement in application variability of INSTANT.

A two-system approach, based on an analytical and a semi-empirical tool, is implemented to increase the tool's fidelity and optionally keep its computation time minimum. The analytical tool relies on blade discretisation and aerodynamic properties, while the semi-empirical tool is based on empirical analogies. To a certain extend, the user is able to choose the algorithm of evaluation. Both tools show good predictive performance, however the analytical tool offers potential to further refine its capabilities of prognosis.

Don't trust the thesis too
much if the abstract already
contains grammatical errors...

Acknowledgement

I first like to thank my thesis supervisor Dr. A. Sahai, who was always available when needed. Any time, even if he was up to his ears in work, he gave me the possibility to walk in his office and ask for advice. He was pleased to help and was fully focused on the challenges to face.

Secondly, I would like to thank Prof. Dr. D. G. Simons for his time. He attended all important meetings and improved my work by asking challenging questions. Moreover, I thank Dr. Ir. A. H. van Zuijlen and Dr. M. Snellen for their readiness of attending the thesis defence as committee members.

Special thankfulness goes to my girlfriend, who had to miss me for the last five and a half years. Thanks to all of my friends, family and anyone who, in some way, has contributed to my academic and private life in Delft. I made great friends in Delft and will always return with good memories and a smile on my face.

L. Klespe

Delft, March 2017

Contents

List of Figures	xi
List of Tables	xvii
Nomenclature	xix
1 Introduction	1
I Research Background	5
2 Interest in CROR Technology	7
3 Noise Characteristics of CROR	9
3.1 Core Noise	9
3.2 Noise of Counter Rotating Rotors.	10
3.2.1 Rotor alone Tones.	11
3.2.2 Interaction Tones	11
3.2.3 Incidence Tones.	12
3.2.4 Broadband Noise	12
4 Demand for CROR Noise Prediction Tool	13
4.1 Need for Noise Prediction Tool	13
4.2 Potential Tools	15
II Methodology	17
5 Lewy Method	19
5.1 OASPL - Directivity	19
5.2 Third Octave Frequency Spectrum.	21
5.3 Tonal Directivity	22
5.3.1 Bessel Function of First Kind	23
6 PARTNER Computations	25
6.1 Tonal Noise	25
6.2 Broadband Noise	26

7 Hanson Model	29
8 Atmospheric Attenuation	35
9 JBlade	37
 III Noise Prediction Tool	 39
10 Tool Initiation	41
10.1 Initiator	41
11 Input Definition	45
12 Semi-Empirical Tool	49
12.1 Generation of OASPL-Directivity	50
12.2 Lewy 1/3-Octave Band Frequency Spectrum	50
12.3 Tonal Noise	55
12.4 Tonal-Directivity	57
13 Analytical Tool	59
13.1 XFOIL Execution.	60
13.2 Computational Database	60
13.3 Hanson's Formulation	61
14 Verification & Validation	63
14.1 Lewy	64
14.1.1 OASPL-Directivity	64
14.1.2 Third Octave Frequency Spectrum	65
14.1.3 Conclusion	66
14.2 PARTNER	66
14.2.1 Frequency Spectrum	67
14.2.2 Tonal-Directivity	69
14.2.3 Conclusion	70
14.3 Analytical Tool	72
14.3.1 OASPL-Directivity	72
14.3.2 Frequency Spectrum	73
14.3.3 Conclusion	77
 IV Concluding Remarks	 81
15 Conclusion & Recommendation	83

V Bibliography	87
Bibliography	89
VI Appendix	95
A Final Result Display	97
A.1 Semi-Empirical Tool	97
A.2 Analytical Tool	101
B Supporting Figures	107

List of Figures

1.1	A Counter Rotating Open Rotor developed by CFM International in pusher configuration [13]	2
2.1	Propulsive efficiency of different engine types[40]	7
3.1	Decomposition of noise sources for a high bypass turbofan in a polar plot at high thrust rating [43]	10
3.2	Noise sources of an exhaust [43]	10
3.3	Broadband frequency spectrum of an exhaust [43]	10
3.4	Interaction of second row blade with upstream element wake [27]	12
3.5	Lobed standing wave pattern at blade passing frequency [16]	12
4.1	Noise simulation and assessment module INSTANT of RWTH Aachen [46]	14
4.2	Tool's updated engine noise subdivision	15
5.1	Example of <i>OASPL</i> -directivity estimation for CROR [28]	20
5.2	Example of a 1/3-octave spectrum due to interaction tones [28]	21
5.3	Tone directivity along a 137cm sideline (90° is aft rotor plane) [54]	23
5.4	Directivity described by Bessel function [28]	23
5.5	Bessel function for $0 \leq m \leq 5$	24
6.1	Broadband noise prediction of CROR noise based on [32]	27
7.1	Forward movement of loading noise lobe peak value for a CROR	30
7.2	Effect of axial induction on local blade angle of attack [44]	32
7.3	Blade pressure distribution first four loading harmonics [49]	32
7.4	Normalised loading distribution function from [19]	33
7.5	Normalised lift and drag loading distribution function applied	33
9.1	F7 blade from literature [22]	38
9.2	Mockup in JBlade for F7 blade	38
9.3	Patented blade from literature [50]	38
9.4	Mockup in JBlade for patent blade	38
10.1	Initiation instant of prediction tool	41

10.2	Computational structure of initiation instant	43
11.1	F7 blade from literature [22]	47
11.2	F7 blade reproduced in Matlab	47
11.3	Patented blade from literature [50]	47
11.4	Patented blade reproduced in Matlab	47
11.5	SR3 from literature [51]	48
11.6	SR3 blade reproduced in Matlab	48
12.1	System structure of semi-empirical tool	49
12.2	Effect of <i>in_funda</i> on 1/3-octave band frequency spectrum for $B_1 = B_2$ after [28]	51
12.3	Effect of <i>in_funda</i> on 1/3-octave band frequency spectrum for $B_1 = B_2 + 2$ after [28]	52
12.4	Effect of <i>increase</i> on 1/3-octave band frequency spectrum for $B_1 = B_2$ after [28]	53
12.5	Effect of <i>increase</i> on 1/3-octave band frequency spectrum for $B_1 = B_2 + 2$ after [28]	53
12.6	Effect of <i>threshold</i> on 1/3-octave band frequency spectrum for $B_1 = B_2$ after [28]	54
12.7	Effect of <i>threshold</i> on 1/3-octave band frequency spectrum for $B_1 = B_2 + 2$ after [28]	54
12.8	Effect of <i>threshold</i> on 1/3-octave band frequency spectrum for $B_1 = B_2$ after [28]	55
12.9	Effect of <i>threshold</i> on 1/3-octave band frequency spectrum for $B_1 = B_2 + 2$ after [28]	55
12.10	Increase <i>SPL</i> of higher tones for 1/3-octave band frequency spectrum for $B_1 = B_2 + 2$ after [28]	56
12.11	Increase <i>SPL</i> of fundamental tones for 1/3-octave band frequency spectrum for $B_1 = B_2 + 2$ after [28]	56
12.12	Tonal directivity for $B_1 = B_2$ after [28]	58
12.13	Tonal directivity for $B_1 = B_2 + 2$ after [28]	58
13.1	System structure of analytical tool	59
14.1	Results compared to figure 197 of [22]	64
14.2	Results compared to figure 199 of [22]	65
14.3	Results compared to figure 208 of [22]	65
14.4	1/3-Octave band results from [28]	66

14.5	Exact reproduction with settings from table 5.2	66
14.6	Tonal SPL compared to [22] with $D_2 = 0.622$ m, $\frac{X}{D_2} = 0.169$, and $CF = 0.83$ based on Lewy+PARTNER	67
14.7	Narrowband compared to [22] with $D_2 = 0.622$ m, $\frac{X}{D_2} = 0.169$, and $CF = 0.83$ based on Lewy+PARTNER	68
14.8	$B_1 = B_2$ prediction for 1/3-octave band at $\theta = 91^\circ$ compared to [22]	69
14.9	$B_1 = B_2$ prediction for 1/3-octave band at $\theta = 68^\circ$ compared to [22] reduced thrust	69
14.10	$B_1 = B_2$ prediction for 1/3-octave band at $\theta = 91^\circ$ compared to [22] reduced thrust	70
14.11	$B_1 = B_2$ prediction for 1/3-octave band at $\theta = 107^\circ$ compared to [22] reduced thrust	70
14.12	$B_1 = B_2$ prediction for 1/3-octave band at $\theta = 120^\circ$ compared to [22] reduced thrust	71
14.13	$B_1 = B_2 + 2$ prediction for 1/3-octave band at $\theta = 96^\circ$ compared to [22]	71
14.14	Predictions based on PARTNER method compared to [54] with $D_1 = 0.622$ m, $D_2 = 0.607$ m, $\frac{X}{D_2} = 0.14$, and $CF = 0.9$	72
14.15	<i>OASPL</i> -directivity based on Hanson compared to figure 197 of [22] for 8+8 CROR	73
14.16	<i>OASPL</i> -directivity based on Hanson compared to Soulat [49] for 8+8 CROR	74
14.17	<i>OASPL</i> -directivity based on Hanson compared to figure 199 of [22] for 8+8 CROR	74
14.18	<i>OASPL</i> -directivity based on Hanson compared to Soulat [49] for 8+8 CROR	75
14.19	<i>OASPL</i> -directivity based on Hanson compared to figure 208 of [22]	75
14.20	<i>OASPL</i> -directivity based on Hanson compared to Soulat [49]	76
14.21	Frequency spectrum at $\theta = 91^\circ$ based on Hanson compared to figure 198 of [22] for 8+8 CROR	76
14.22	Frequency spectrum at $\theta = 105^\circ$ based on Hanson compared to figure 198 of [22] for 8+8 CROR	77
14.23	Frequency spectrum at $\theta = 90^\circ$ based on Hanson compared to figure 200 of [22] for 8+8 CROR	77
14.24	Frequency spectrum at $\theta = 105^\circ$ based on Hanson compared to figure 200 of [22] for 8+8 CROR	78
14.25	Frequency spectrum at $\theta = 95^\circ$ based on Hanson compared to figure 209 of [22] for 11+9 CROR	78
14.26	Frequency spectrum at $\theta = 105^\circ$ based on Hanson compared to figure 209 of [22] for 11+9 CROR	79

A.1	Display if plot_LewyDirectivity = 1 in <i>Initiate.m</i>	97
A.2	Display if plot_LewyThirdOctave = 1 in <i>Initiate.m</i>	98
A.3	Display if plot_Lewy3DThirdOctave = 1 in <i>Initiate.m</i>	98
A.4	Display if plot_tonal_Directivity = 1 in <i>Initiate.m</i>	99
A.5	Example display if plot_Bessel_Directivity = 1 in <i>Initiate.m</i>	99
A.6	Display if plot_Frequency_Spectrum = 1 in <i>Initiate.m</i> example of 90°	100
A.7	Display if plot_PARTNER3D = 1 in <i>Initiate.m</i>	100
A.8	Display if plot_PARTNER_Lewy = 1 in <i>Initiate.m</i>	101
A.9	Display if plot_PressureSignal = 1 in <i>Initiate.m</i> example of 65°	101
A.10	Display if plot_PressureSignal = 1 in <i>Initiate.m</i> example of 90°	102
A.11	Display if plot_FFTattenuated = 1 in <i>Initiate.m</i> example of 65°	102
A.12	Display if plot_FFTattenuated = 1 in <i>Initiate.m</i> example of 90°	103
A.13	Display if plot_FrequencySpectra = 1 in <i>Initiate.m</i> example of 65°	103
A.14	Display if plot_FrequencySpectra = 1 in <i>Initiate.m</i> example of 90°	104
A.15	Display if plot_Directivity = 1 in <i>Initiate.m</i>	104
A.16	Display if plot_3DFrequencySpectrum = 1 in <i>Initiate.m</i> example of 90°	105
A.17	Display if plot_3DThirdOctave = 1 in <i>Initiate.m</i> example of 65°	105
B.1	1/3-octave band from [22] figure 200 b	107
B.2	Tonal noise prediction based on PARTNER for $B_1 = B_2$, $TS_f = 1$, $TS_a = 2$, and $TS_s = 3$	108
B.3	Tonal noise prediction based on PARTNER for $B_1 = B_2$, $TS_f = 1.5$, $TS_a = 2$, and $TS_s = 3$	108
B.4	Tonal noise prediction based on PARTNER for $B_1 = B_2$, $TS_f = 2$, $TS_a = 2$, and $TS_s = 3$	109
B.5	Tonal noise prediction based on PARTNER for $B_1 = B_2 + 2$, $TS_f = 1$, $TS_a = 2$, and $TS_s = 3$	109
B.6	Tonal noise prediction based on PARTNER for $B_1 = B_2 + 2$, $TS_f = 1.5$, $TS_a = 2$, and $TS_s = 3$	110
B.7	Tonal noise prediction based on PARTNER for $B_1 = B_2 + 2$, $TS_f = 2$, $TS_a = 2$, and $TS_s = 3$	110
B.8	Tonal noise prediction based on PARTNER for $B_1 = B_2$, $TS_f = 1.5$, $TS_a = 1$, and $TS_s = 3$	111
B.9	Tonal noise prediction based on PARTNER for $B_1 = B_2$, $TS_f = 1.5$, $TS_a = 3$, and $TS_s = 3$	111
B.10	Tonal noise prediction based on PARTNER for $B_1 = B_2 + 2$, $TS_f = 1.5$, $TS_a = 1$, and $TS_s = 3$	112

B.11	Tonal noise prediction based on PARTNER for $B_1 = B_2 + 2$, $TS_f = 1.5$, $TS_a = 3$, and $TS_s = 3$	112
B.12	Tonal noise prediction based on PARTNER for $B_1 = B_2$, $TS_f = 1.5$, $TS_a = 2$, and $TS_s = 1$	113
B.13	Tonal noise prediction based on PARTNER for $B_1 = B_2$, $TS_f = 1.5$, $TS_a = 2$, and $TS_s = 1$	113

List of Tables

4.1	List of requirements for CROR noise prediction tool	15
4.2	Leading scientist for analytical investigation of CROR noise and their work	16
5.1	Correction on <i>OASPL</i> due to CROR configuration [28, 29]	21
5.2	General settings of 1/3-octave band function from [28]	22
6.1	McCurdy relative attenuation factors [32]	25
6.2	Coefficients for broadband noise from [32]	26
7.1	Correction of higher load harmonics	33
8.1	Relation between δ and η [43]	36
9.1	Analysis conditions for propeller in JBlade	37
10.1	List of settings for CROR noise prediction tool	42
10.2	List of warnings for CROR noise prediction tool if Eval_Op = 2	43
11.1	Required input data of prediction tool	46
12.1	Input and output data of Lewy-OASPL-directivity function	50
12.2	Input and output data of Lewy 1/3-octave frequency spectrum function	51
12.3	Input and output data of PARTNER tones function	57
12.4	Input and output data of tonal directivity function	57
13.1	Input and output data of XFOIL execution function	60
13.2	Syntax of <i>generateNAME.m</i>	60
13.3	Input and output data of Hanson's formulation functions	61
14.1	General input for verification and validation process	63
15.1	Overview of accordance with data in temporal perspective	84

Nomenclature

Acronyms

BBL	Broadband Noise Level
BPF	Propeller Blade Passage Frequency
CAA	Computational Aeroacoustics
CFD	Computational Fluid Dynamics
CROR	Counter Rotating Open Rotor
FFT	Fast Fourier Transform

Symbols

α_{at}	Sound Attenuation Coefficient [dB/100m]
Δ_{SPL}	Atmospheric Attenuation [dB]
$\frac{X}{D_2}$	Normalised Rotor Spacing [-]
Ω_1	First Rotor Angular Speed [Hz]
Ω_2	Second Rotor Angular Speed [Hz]
Ω_{12}	Ratio of Rotational Speeds $\frac{\Omega_1}{\Omega_2}$ [-]
Φ	Overall Directivity [dB]
ϕ	Angular Observer Angle [rad]
ϕ^2	Angular Blade Angle at Initial Time [rad]
ϕ_o	Phase Angle Associated with Offset [rad]
ϕ_s	Phase Angle Associated with Sweep [rad]
ψ_{Dk}	Normalised Drag Loading Distribution Function [-]
ψ_{Lk}	Normalised Lift Loading Distribution Function [-]

ρ	Density of Air [kg m^{-3}]
θ	Observer Angle [rad]
a	Axial Induction Factor [-]
B	Total Blade Count [-]
B_1	Numbers of Blades on First Rotor [-]
B_2	Numbers of Blades on Second Rotor [-]
c	Speed of Sound in Air [m s^{-1}]
C_{Dk}	k th Drag Harmonic Coefficient [-]
C_{Lk}	k th Lift Harmonic Coefficient [-]
$cdr1$	Chord to Diameter Ratio Front Rotor [-]
$cdr2$	Chord to Diameter Ratio Aft Rotor [-]
CF	Fraction of Engine's Rotational Speed [-]
D	Rotor Diameter [m]
D_2	Second Rotor Propeller Diameter [m]
$D_{in,1}$	Hub Diameter of Front Rotor [m]
$D_{in,2}$	Hub Diameter of Aft Rotor [m]
FA	Face Alignment [m]
H	Ambient Air Humidity [%]
k	Order of Load Harmonic [-]
k_x, k_y	Wavenumber [-]
m	Order of Sound Harmonic [-]
M_n	McCurdy Relative Attenuation Value of Tone n [-]
M_r	Second Rotor Blade Section Relative Mach Number [-]
M_T	Second Rotor Blade Tip Rotational Mach Number [-]
M_x	Flight Mach Number [-]

<i>MCA</i>	Mid Chord Alignment [m]
<i>OAPWL</i>	Overall A-Weighted Power Watt Level [dBA]
<i>OASPL</i>	Overall A-Weighted Sound Pressure Level [dBA]
<i>R</i>	Rotor Radius [m]
<i>r</i> ₁	Observer Constant Sideline Distance [m]
<i>T</i>	Engine Thrust [N]
<i>t</i>	Evaluation Time [s]
<i>TS</i> _p	Tone Scalar for either Front or Rear Rotor [-]
<i>TS</i> _p	Value for every Third Tone in Narrowband [-]
<i>v</i> ₀	Flight Speed [ms^{-1}]
<i>W</i> ₀	Threshold of Hearing [W]
<i>W</i> _{ac}	Acoustic Power [W]
<i>W</i> _{mec}	Shaft Mechanical Power [W]
<i>z</i> ₀	Ratio of Source over Tip Radius [-]
OSPL	Overall Sound Pressure Level [dB]
SPL	Sound Pressure Level [dB]

1

Introduction

Probably, conventional aircraft designs are predominantly pictured when talking about planes. Immediately, fuselage, empennage, wings, and engines are the components imagined. Perhaps, the most fascinating subsystem is the propulsion unit. Currently, turbofan and turboprop engines are commonly used on airliners. Stricter policies and the desire for higher profit compel aircraft manufacturers to enhance fuel efficiency of planes. Recent volatility in fuel prices and environmental impact of aircraft emissions support that development. Already in the 1970s and 80s increased fuel prices caused the aeronautical research to focus on fuel efficient transport aircraft and alternative propulsion systems.

Typically, cruise Mach numbers of airliners range from 0.7 to 0.9. For the higher speeds, the efficiency of propellers drops rapidly [38]. In 1951, Brady suggested to use thin and/or swept blades to overcome the degradation in efficiency at transonic speeds [38]. ‘However, because of low fuel costs and the advent of the turbofan this idea was not pursued’ [38]. Some 30 years later, for propeller engines Mitchell and Mikkelsen [34] suggested to implement a second propeller, which rotates in the opposite direction to the forward propeller and thus corrects the introduced swirl of the upstream rotor, known as counter rotating propeller. Mitchell and Mikkelsen amounts the swirl loss to a range from about 7 to 11 % [34]. Further, [38] refers to Strack (1982), who supports the statement of [34] by concluding that a counter rotating propeller provides an improvement of 8 % in propulsive efficiency compared to a single-rotating propeller. However, in the end choice was made to use turbofan engines, which outperformed former propeller technology for high subsonic and transonic flight.

Down to the present day, high subsonic propulsion is based on the technology of high-bypass turbofan engines. Although, it seems that alternative propulsion systems have to be

reconsidered, since turbofan technology appears to hit its limits and the impact of technical enhancements stagnates. Open Rotor propulsion appears to be a promising solution. More precisely, the answer to future demands is found in the technology of Counter Rotating Open Rotor (CROR). A concept design of a CROR is shown in figure 1.1, in which the thin and swept blades proposed by Brady in 1951 are evident. Main advantages are (i) the reduced nacelle diameter, which results in decreased weight and skin friction drag, (ii) the possible increase in rotor diameter and therewith raise in bypass ratio, and (iii) the avoided swirl loss due to the second rotor as compared to the fan. However, the acoustic characteristics of a CROR change drastically when compared to turbofan or single-rotating propeller.



Figure 1.1: A Counter Rotating Open Rotor developed by CFM International in pusher configuration [13]

Hubbard was one of the pioneers investigating acoustics of a CROR already in 1948 [23, 38]. Sound measurements for static conditions were executed and compared with a theoretical analysis. Mutual interference has been detected and its relation to Propeller Blade Passage Frequency (BPF) and rotor spacing. Additionally, he discovered ‘lobular azimuthal directivities’[38] for which ‘the maximum sound pressures occur at the axis of overlap’[23]. In 1952, Roberts and Beranek were one of the first to identify a difference in noise emission for installed propeller engines in pusher or tractor configuration as the pylon’s aerodynamics influences the flow field around the blades. The pusher configuration ‘radiates sound more uniformly in all directions in flight than do the tractor-type’[41]. Some 30 years later, based on his application of the acoustic analogy to propellers, Hanson [16] provided an analytical description of noise generation by (un-)steady forces on blades of counter rotation propellers in frequency domain. Same year at NASA Langley, Block [2] investigated noise radiation patterns of counter rotation and unsteadily loaded single-rotation propellers. Further, Block was the leading researcher in exploring installed

propeller engines. The results obtained from the experimental study of the effects of installation on single- and counter rotation propeller noise are presented in [3]. Block et al. further investigated the directivity and trends of noise generated by single and counter rotation propeller in a wake [4, 5]. Maglizzio et al. at Hamilton Standard conducted parametric experiments on counter rotation prop-fans. The modelled blades inherit same characteristics as nowadays installed blades, that is being thin and swept [30].

During the 1980's, at Lewis Research Center, Dittmar discovered an increase in noise emission of counter rotation propeller at positive angles of attack [7]. Moreover, the noise emission of the slim, high sweep SR-3 Propeller was a preceding study in 1981 [8]. In order to reduce noise, the idea of decreasing the aft-propeller diameter, called rotor clipping, was investigated [9]. During the 1980's and 1990's, Farassat strongly focused on the noise prediction of propeller using the Ffowcs Williams-Hawkins equation, requiring long computational time, and Computational Fluid Dynamics (CFD) data [10, 11, 31].

At NASA Lewis Research Center, Whitfield, Mani, and Gliebe developed a high speed turboprop aeroacoustic computer program to predict the noise of counter rotating turboprops [52, 53]. The data for comparison was found in a model scale test executed by Janardan and Gliebe to understand the acoustic characteristics of unducted fans [25] and Hoff et al. [22] investigating different blade concepts.

One of the latest researchers examining noise of CROR are Kingan, Parry, and Lewy. Kingan and Parry are pioneers in investigating the importance and dependence of CROR broadband noise, as they were convinced that only tonal noise examination is not sufficient to characterise the noise emissions of CROR [26, 39]. ‘The results show that the noise levels vary substantially with blade speed’ [39]. Further Parry strives to predict the broadband noise of CROR [37]. In 2010, Lewy developed a semi-empirical prediction of tone noise due to CROR. The developed model also predicts the overall noise and the tonal directivity [28]. The well known Bessel Function of the First Kind is frequently used to determine the directivity of CROR noise, so it is in [28].

In the past, several studies indicated the problem of noise generation for CROR. Nevertheless, for future aircraft development it is important to predict the noise and incorporate the gained knowledge into the exploration and design of new (concept) aircraft. The engine installation and propeller configuration strongly depends on the aircraft composition. This work aims to provide a prediction technique and program for counter rotating propeller noise. The focus lies on far field noise, since any airliner equipped with CROR has to comply to certification containing stringent community noise regulations. Although there exist some concern over cabin noise it is not issued in this work.

This work is divided into four main parts, which are subdivided in chapters. Part I treats

the research background and gives a motivation for this work. Chapter 2 explains the need for novel propulsion technologies, in particular CROR engines, and presents a list of challenges to be solved for future implementation. Noise characteristics of CROR engines are described in chapter 3. In particular core and rotor tonal noise are explained. Chapter 4 presents the motivation of this work and justifies the demand for a CROR noise prediction tool. Moreover, the requirements for and capabilities of the tool are defined, which leads to a list of literature forming the tool's basis.

Part II presents the methodologies incorporated in the noise prediction tool. Firstly, chapters 5, 6, and 7 explicitly treat the literature mentioned in chapter 4. Tonal noise and directivity of CROR on the basis of Lewy's theory are formulated in chapter 5. The frequency spectrum using Lewy's outputs can be generated based on the content of PARTNERS project. Chapter 6 presents the relevant results for this work. Both, methods together will compile the semi-empirical tool. Chapter 7 examines Hanson's formulation of CROR far-field noise and presents assumptions made. Next, chapter 8 describes the theory of atmospheric attenuation, which is applied to the results from chapter 7. For Hanson's formulation, the blade's aerodynamic properties have to be known. JBlade is used for data generation. Its functioning is presented in chapter 9.

The tool routine and its functions are explained in part III. Firstly, the tool initiation and settings are presented in chapter 10. Next, the input file and its syntax is explained in chapter 11. After the input was imported, the tool will execute the semi-empirical or analytical noise prediction, which are discussed in chapters 12 and 13, respectively. Verification and validation of both tools are conducted in chapter 14.

The report is concluded in chapter 15, which is contained in part IV.

I

Research Background

2

Interest in CROR Technology

Propulsion systems are selected according to the cruise speed of an aircraft. Each engine's maximum propulsive efficiency is achieved at different speeds. Figure 2.1 illustrates the difference in performance for turboprop (indicated by turbo-prop), turbofan (by-pass turbo-jet), and turbojet (pure turbo-jet) engines.

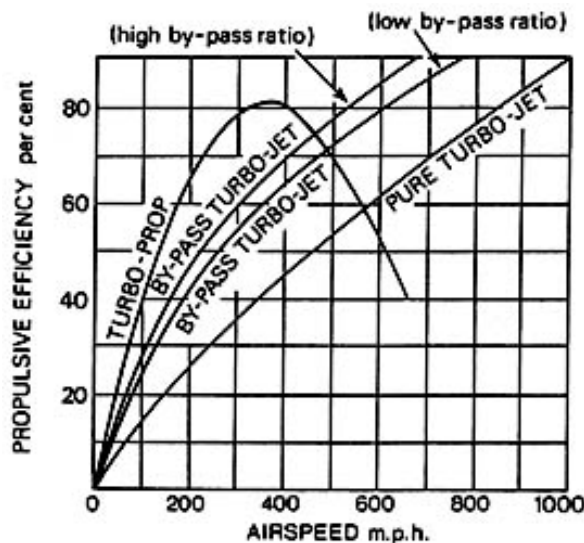


Figure 2.1: Propulsive efficiency of different engine types[40]

High subsonic propulsion is based on the technology of high-bypass turbofan engines. Higher propulsive efficiency is achieved by increasing the fan diameter, which leads to a growth in bypass ratio. A diminishing return to this improvement is the enlarged nacelle diameter and consequently a raise in weight and drag. Open rotor engines do not feature a surrounding nacelle, thus enabling ultra high bypass ratios. Therefore, technology of CROR

grants access to further improvements in propulsive efficiency. Another supporting factor is the second row of propeller blades, which removes the swirl induced by the front row, thus correcting the thrust in axial direction [42]. Concluding, ‘CROR technologies offer the potential for significant reductions in fuel burn and CO₂ emissions relative to turbofan engines of equivalent thrust’ [42].

Nevertheless, reasons exist for disregarding novel technologies like CROR. Rolls-Royce defines the principal technical challenges of CROR engines accordingly [42]:

- ‘Reduction of the noise created by the propeller blades to counter the loss of attenuation provided by a turbofan nacelle.’
- ‘Definition of the propeller system to reduce the noise created by the counter rotating blades.’
- ‘Complexity of communications and blade pitch control through the counter rotating power transmissions system.’
- ‘Installation of the open rotor engine on the airframe. Turbofans are isolated from the airframe by the nacelle but the airflow through open rotor propellers interacts with the supporting airframe structure and so the installation impacts on the engine system noise and efficiency’.

Hereafter, the work focuses on noise issues only. In order to successfully tackle the challenges of noise reduction the sources have to be defined and the characteristics need to be identified. The following chapter deals with the acoustic attributes of a CROR.

3

Noise Characteristics of CROR

Initially, CROR noise is emitted by two different engine components. The CROR core inherits a gas turbine, based on the principles of a conventional turbojet, which drives the rotors. Both, the core engine and propeller produce broadband noise. Additionally, individual rotor tones but also interaction tones of the blade rows are present in the frequency spectrum. This chapter investigates the traits of CROR noise. The impact and importance of every aspect for the overall noise generation is evaluated. Both, the core noise and rotor tones are treated individually.

3.1 Core Noise

The primary task of the core engine in a CROR is the generation of mechanical power for the rotors. Usually, the core is composed of compressor, combustor, turbine, and nozzle, each one being a noise source on its own. The counter rotating rotors create a bypass flow around the core engine. Bypassing the core at high thrust levels reduces the overall noise of the core exhaust. Turbofan engines benefit from the same principle. A typical noise polar plot showing the component breakdown for high bypass turbofan is depicted in figure 3.1, where the core exhaust is indicated by 'jet'.

Accelerated exhaust gases produce broadband noise as it is distributed through all frequencies within the audible range [43]. The mechanisms of noise generation due to accelerated exhaust gases are depicted in figure 3.2. Any fluctuations in pressure is directly related to noise emission. The shear between ambient airflow and exhaust gas introduces small vortices that will grow in downstream direction. Small vortices generate high frequency sound, for increasing vortex size, frequency reduces.

For any engine a reduction in speed of the exhaust gas results in lower broadband noise.

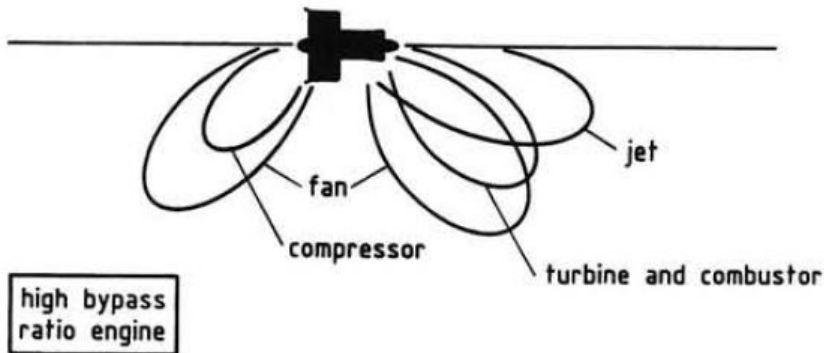


Figure 3.1: Decomposition of noise sources for a high bypass **turbofan** in a polar plot at high thrust rating [43]

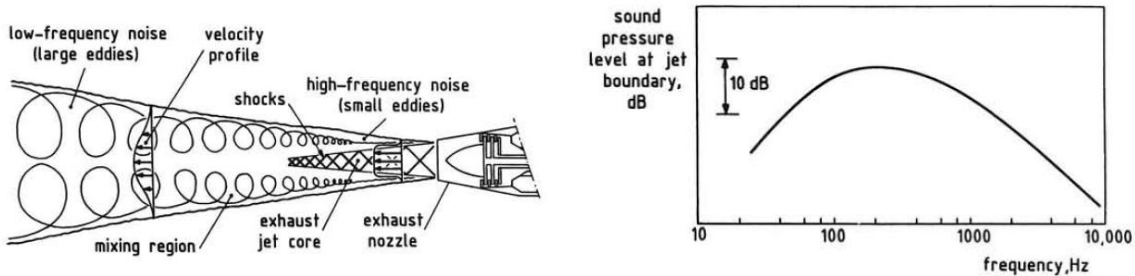


Figure 3.2: Noise sources of an exhaust [43] Figure 3.3: Broadband frequency spectrum of an exhaust [43]

In other words, **for turbofan engines an increased fan diameter (decrease in exhaust speed) reduces the noise emission**. This simplification does not necessarily hold for CROR. Contrary to turbofan engines, **the absence of a nacelle for CROR does not shield of the rotor noise**. Moreover, **not the same acoustic theories apply for single and counter rotating blade rows**. In figure 3.1 the indicated fan noise is therefore wrong in direction of propagation and low in level, which means that the core noise is less pronounced for a CROR as it is for a high bypass turbofan. It must be clear, that the bypassed airflow of CROR shows the same acoustic characteristics as it does for turbofan engines. However, the counter rotating rotors produce distinct noise, which is elaborated on in the next section.

3.2 Noise of Counter Rotating Rotors

In the following, sound generation due to the rotors is explained. In total four different types of noise can be identified, which can be explained with different theories:

1. Rotor alone tones

Steady loading noise [16, 27, 38, 52]

Thickness loading noise, or volume displacement noise [16, 27, 38, 52]

2. Interaction tones

Aerodynamic interference, or unsteady loading noise [16, 27, 38, 52]

Acoustic interference [16]

3. Incidence tones [27]

4. Broadband noise [27]

3.2.1 Rotor alone Tones

When investigating propeller rotors individually, noise generation is inevitable. Rotor alone tones are composed of steady and thickness loading [27]. Individually, each propeller blade creates aerodynamic force distribution in blade fixed coordinates (steady loading). Moreover, the blades have finite thickness resulting 'in a continuous extraction and injection of fluid across the boundary of any control volume' [38]. These effects create sound pressure which, 'for a fixed observer means that the fluid forces fluctuate at blade passing frequency, resulting in acoustic dipole radiation' [38] for steady loading noise and monopole for thickness loading noise [38]. Since the fluctuations only occur at blade passing frequency it is referred to tones.

3.2.2 Interaction Tones

The two types of interaction tones can be explained separately, since the theory of origin is clearly different. Firstly the unsteady loading, emerging from aerodynamic effects, is explained. Secondly acoustic interference, arising from the physical principles of sound generation is presented.

Unsteady Loading

The aerodynamic performance of isolated blades differs from a set of blades. Following aerodynamic theories any element in a stream introduces circulation [48]. While a downstream blade cause a favourable increase in velocity for the upstream element, also known as upwash or slat effect, the upstream blade causes circulation which is counteracting the velocities of downstream blades, called downwash or circulation effect [48]. Additionally, tip vortices are inherent to finite blade wakes, which induce unsteady loading on the downstream element. The aforementioned erratic fluctuations interfere with the isolated pressure distribution of the rotor blades, which results in increased noise generation [16, 38]. The interference with the wake of the upstream blade is shown in figure 3.4.

Acoustic Interference

Assuming linear superposition, the CROR noise field is the summation of fields from each rotor. Noise with same frequency generates ‘standing wave patterns around the axis of rotation through the constructive and destructive process of acoustic interference. Moreover, two spinning modes from the same rotor can also produce a circumferential standing wave pattern. These two acoustic interference cases (inter-rotor and intermode) can produce circumferential directivity patterns whose differing characteristics may be useful for noise source diagnosis’ [16]. An example for a CROR with identical two-blade rotors is depicted in figure 3.5.

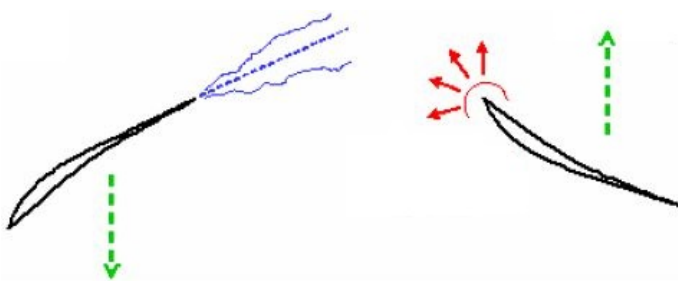


Figure 3.4: Interaction of second row blade with upstream element wake [27]

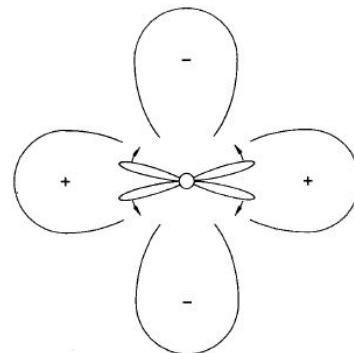


Figure 3.5: Lobed standing wave pattern at blade passing frequency [16]

3.2.3 Incidence Tones

The incidence tones, originate from an unsteady loading on the blades due to propeller’s operation at angle of incidence [27]. This unsteady loading adds to the previously mentioned unsteady loading.

3.2.4 Broadband Noise

Rotor broadband noise is generated in the same principle as it is for the core. Here, the rotor wake has an increased speed compared to the ambient air. Sheer between them generates atmospheric turbulence noise [27]. A basic example of broadband noise is depicted in figure 3.3. For further explanation refer to section 3.1.

This can come from (TE and tip) vortices and boundary layer

4

Demand for CROR Noise Prediction Tool

More than ever, industry relies on computer systems that are able to process jobs automatically. Computations become faster with each new generation of computer systems. Today's aircraft manufacturers use the advancement in computational technology to more efficiently design aircraft and evaluate the performance. Therefore, knowledge of new technologies need to be incorporated in design and evaluation tools.

The renewed interest in CROR demands programs that are capable of predicting the performance. Thus far, one of the greatest identified threats of CROR is the acoustic performance, especially the tonal noise. Engineers are concerned about its formation already at the design stage of aircraft. This chapter expounds the demand for a CROR noise prediction tool. Moreover, the requirements for and capabilities of the tool to be developed are defined.

4.1 Need for Noise Prediction Tool

Nowadays, design automation and its assessment is more important than ever. In aviation, automated computer programs support the development of aircraft. Since any design modification may result in performance changes, fast executable evaluation tools monitor the algorithms and if necessary restrict the effective design space. For integration of novel technologies into industry, updates to current algorithms have to be implemented. For CROR the change in noise characteristics compared to today's engines demand this update.

In aviation, strict noise regulations oblige aircraft manufacturers and operators to follow stringent procedures. Airliners and engines have to obey certain noise limits. To guar-

to guarantee the compliance to regulations, noise emission simulations are executed during aircraft design. The obtained information on noise emission is also used to generate noise contours, which reveal airport community noise. The so generated data is the starting point for any aircraft routing optimisation.

Engine noise is an essential part of the overall aircraft noise. Therefore, for any kind of propulsion system, accurate noise prediction is important. Currently, Delft University of Technology possesses an aircraft noise prediction tool called INSTANT from [46]. Its flow chart is depicted in figure 4.1. INSTANT inherits an unit to predict turbofan noise, which is indicated by a red circle in figure 4.1. With renewed interest in CROR, the demand for a package containing algorithms to predict noise emission of any CROR arose. A reliable simulation increases the range of application for aircraft noise assessment and allows for the analysis of more innovative designs and their performance at airfields. The update to unit 'Engine Noise' is depicted in figure 4.2, where the calculations for either 'Turbofan Noise' or 'CROR Noise' are performed.

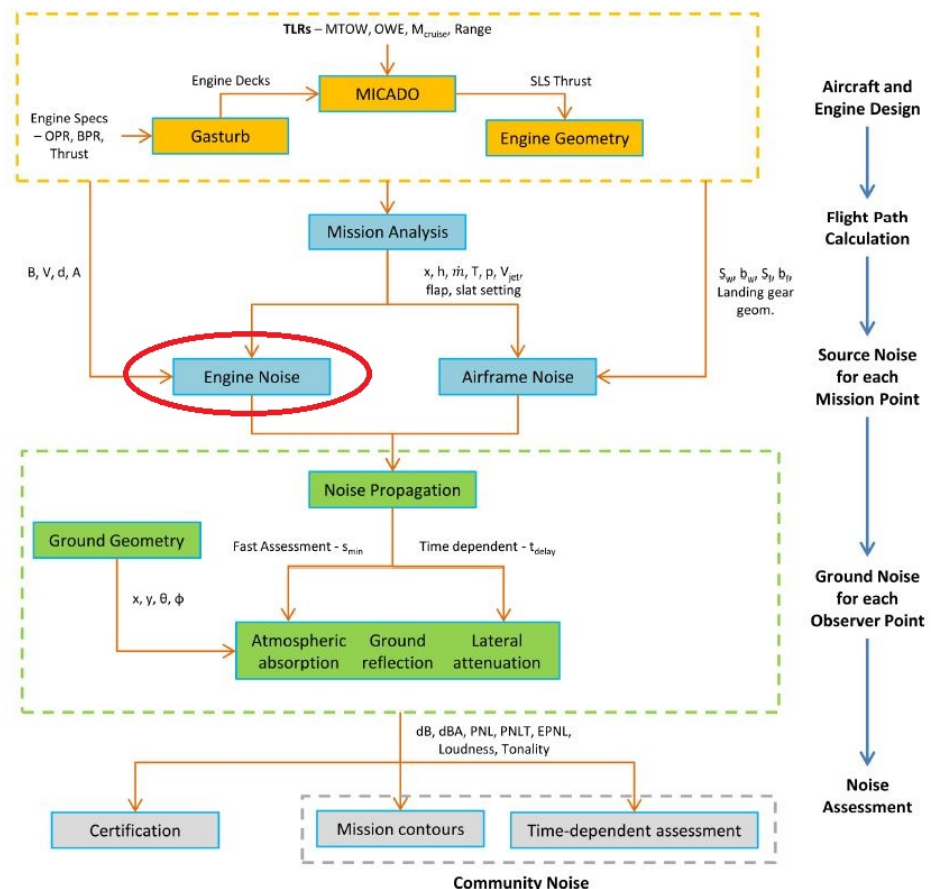


Figure 4.1: Noise simulation and assessment module INSTANT of RWTH Aachen [46]

The developed tool will be used in the environment of an aircraft design instrument.

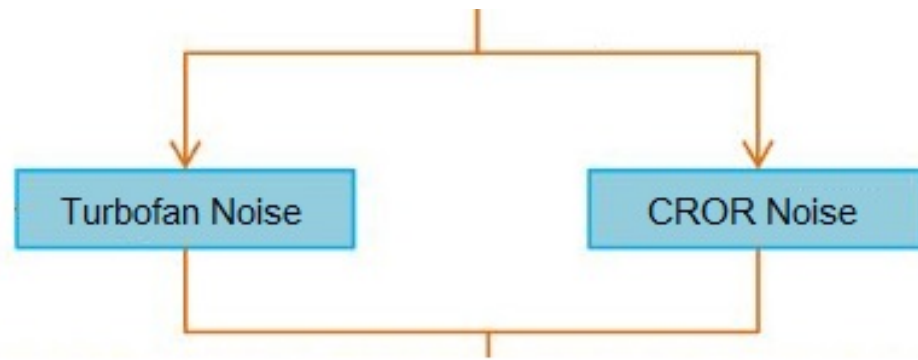


Figure 4.2: Tool's updated engine noise subdivision

Therefore, amongst other requirements, the tool should quickly accept inputs and in short computation time return reliable output. A complete list of requirements can be found in table 4.1.

Table 4.1: List of requirements for CROR noise prediction tool

Small amount of input data
Fast import of input data
Fast return of output data
Vast range of application
High accuracy and reliability

After defining the requirements, potential tools and their routines can be investigated.

4.2 Potential Tools

User demands drive the tool development. Basically, the design is bounded to two extrema. On the one hand, a purely empirical solution can be intended, on the other hand, it can be striven for fully theoretic computation. For a combination of both, it is referred to semi-empirical evaluation. When deciding on the share, a trade off amongst accuracy, computing time, and applicable range is run through. Empirical solutions are fast, however their accuracy/fidelity plus range are impaired (high degree of simplification) and often only valid for existing configurations. To the contrary, a theoretic approach is chosen if the computing time is not an important driver, but the accuracy and range of application is of high value. Generally, if the program solution range is extended the fidelity is reduced [36]. Summarising, prediction methods can be either numerical or analytical. However, 'analytic methods can be used to produce quick noise predictions which makes them ideal for use as a design tool.' [27]

Usually high fidelity tools are based on blade aerodynamics and aeroacoustic. Thus it

requires implementation of CFD and Computational Aeroacoustic (CAA), introducing long processing time. Contrary, semi-empirical tools quickly return results and are associated with less extensive amount of input data. Since computation time is a driving factor for the prospective tool, further investigation focuses on semi-empirical and analytical instruments.

Special attention is paid to take-off and approach conditions, as they are crucial during certification. Moreover, the tool should be able to also predict flyover noise at one instance of time, to fulfil the demand of certification routines (regulations can be found under [24]). In this work, the cabin noise is not examined, therefore the focus is on far-field noise in the free field.

Lastly, outputs need to be defined for the tools. Consequently, the relevance of any knowledge can be classified. The tool will provide the following outputs:

- Noise directivity, i.e. Overall Sound Pressure Level (OSPL) vs. observer angle
- Frequency spectrum for different observer angle, i.e. Sound Pressure Level (SPL) vs. frequency

At this stage, the characteristics are well defined and the most relevant researchers are selected. The leading scientists and their work for CROR analytical prediction method are listed in table 4.2.

Table 4.2: Leading scientist for analytical investigation of CROR noise and their work

Author and most relevant Work	Analytical prediction of
Lewy, S. [28]	Tone noise and directivity of CROR
Mavris, D.; Tai, J.; Young, R.; Havrilesko, B. [32]	CROR noise frequency Spectrum
Hanson, D. B. [16, 18–21]	Far-field CROR noise

In the following chapters, all above listed theories are explained in detail. Their mathematical formulations are presented.

II

Methodology

5

Lewy Method

This chapter presents the developed noise prediction methods by Lewy [28]. Firstly, the equations to predict the directivity of Overall A-Weighted Sound Pressure Level (*OASPL*) are presented (section 5.1). The theory to predict 1/3-octave frequency spectrum for any given *OASPL* is explained in section 5.2. Fast predicting methods for directivity of individual tones based on Bessel Function of First Kind is concluding this chapter (section 5.3).

5.1 OASPL - Directivity

Initial computations on basis of [28] quickly return a directivity plot that presents an estimation of the *OASPL* at any observer location required. Simple input parameters are related to an *OASPL* for specified observer angles, θ . At a constant sideline distance, r_1 , the *OASPL* is determined by equation 5.1 leading to figure 5.1:

$$OASPL = -20 \cdot \log_{10} \left(\frac{r_1}{\sin(\theta)} \right) + \Phi + OAPWL - 8.9 \quad (5.1)$$

with the overall directivity, Φ , defined by equation 5.2:

$$\Phi = -0.002 \cdot (\theta \cdot (\theta - 180) + 90^2) \quad (5.2)$$

The Overall A-Weighted Power Watt Level, *OAPWL*, is related to the threshold of hearing, $W_0 = 10^{-12}$ W, and computed from equation 5.3:

$$OAPWL = 10 \cdot \log_{10} \left(\frac{W_{ac}}{W_0} \right) \quad (5.3)$$

where the acoustic power, W_{ac} , is determined using equation 5.4:

$$W_{ac} = \frac{1}{B} \cdot \frac{W_{mec}}{D_2^2} \quad (5.4)$$

with the total blade count, $B = B_1 + B_2$, shaft mechanical power, W_{mec} , and the diameter of second rotor, D_2 . The total blade count is the summation of numbers of blades on first rotor, B_1 , and second rotor, B_2 . Further details on the process of estimating W_{mec} if thrust is the given engine parameter instead, can be found in chapter 11. Note, it was found that Lewy generally over-predicts the directivity sound level. To scale the acoustic radiation of the rotors and to predict the noise values accordingly, the directivity graphs need adaptation. The solution was found in the dependence of W_{mec} in normalised rotor spacing, $\frac{X}{D_2}$, which is written in equation 5.5:

$$W_{mec,true} = W_{mec,in} \cdot \left(1 - \frac{X}{D_2}\right) \quad (5.5)$$

with spacing as fraction of absolute spacing between both rotors, X in m, over the tip diameter of the second rotor, D_2 in m. Moreover, the SPL can be scaled by the fraction of engine's rotational speed (equation):

$$CF = \frac{RPM_{true}}{RPM_{nom}} \quad (5.6)$$

which finally leads to $OASPL_{true} = OASPL_{Lewy} \cdot CF$

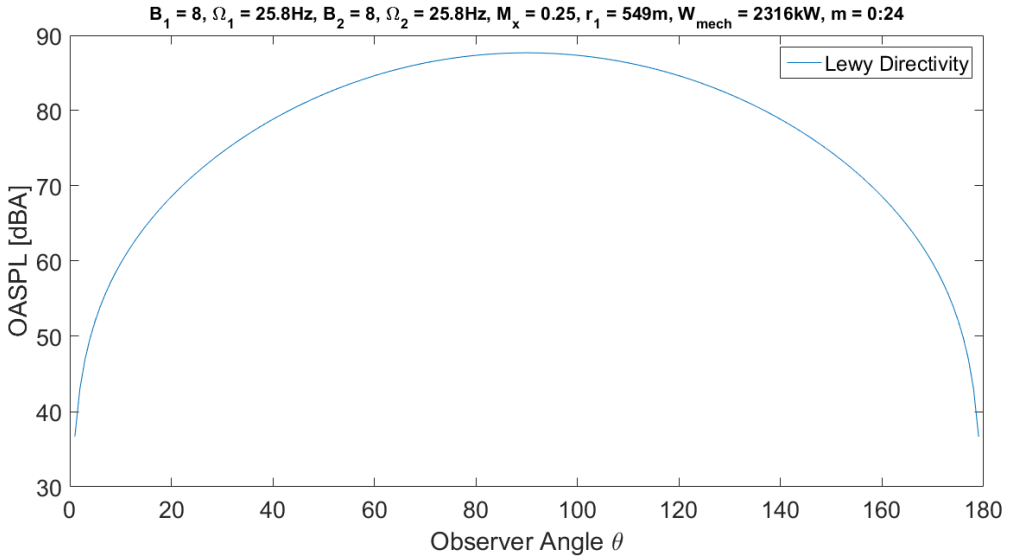


Figure 5.1: Example of OASPL-directivity estimation for CROR [28]

Since the $OASPL$ is computed for a tractor configuration at zero angle of attack, the determined values may be corrected by the sound levels of table 5.1.

The computed results can be used as reference value for the solutions of other methods,

Table 5.1: Correction on OASPL due to CROR configuration [28, 29]

CROR	Angle of attack	
	Zero degree	Non-zero
Tractor	Reference = 0 dB	+ 3.5 dB
Pusher	+ 1.5 dB	+ 2.5 dB

or as input to any secondary computation, for example to generate the third octave band frequency spectrum.

5.2 Third Octave Frequency Spectrum

Third octave band frequency spectrum can be generated by further theories provided in [28]. The theory is based on experimental results, which showed that third octave spectra decrease in high frequency range by approximately 10 dB per octave. According to [28] that is ‘a slope of the squared sound pressure in $(1/f)^3$.’ Further [28] explains, that ‘this shape is duplicated in the prediction if the amplitude of each tone is proportional to $(1/f)^5$ in case of $(n_1 + n_2) > 5$.’ For harmonics $(n_1 + n_2) \leq 5$ ‘the amplitudes are assumed to remain constant’ [28]. A third octave frequency spectrum is depicted in figure 5.2. Note: Harmonics of *BPF* are indicated by n_1 and n_2 for BPF_1 and BPF_2 , respectively. For example, the interaction tone composed of the first harmonic of BPF_1 and fundamental of BPF_2 is hence indicated by $n_1 = 2$ and $n_2 = 1$.

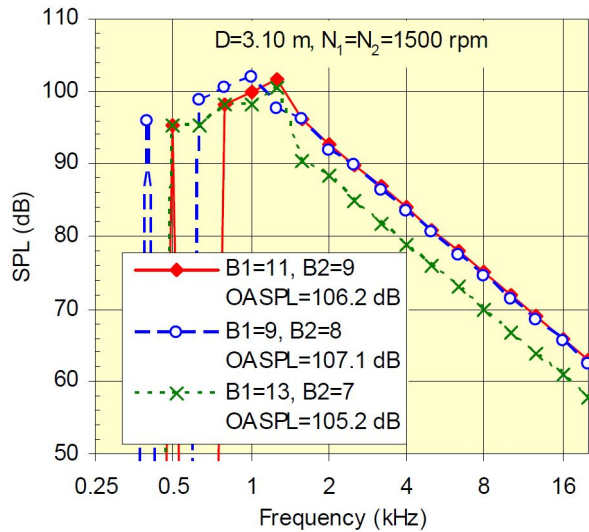


Figure 5.2: Example of a 1/3-octave spectrum due to interaction tones [28]

To generate the third octave frequency spectrum in its shape, at first the *BPF* and their harmonics plus interaction tones are sorted into third octave bands and a two step iteration

is executed. Its results are depending on four pre-set values:

1. *in_funda*: For every fundamental *BPF* ($n_1 = 1$ or $n_2 = 1$) *in_funda* is added to the containing third octave band.
2. *increase*: The value is added to the third octave band for every contained harmonic or interaction tone. However, only tones with $n_1 + n_2 \leq \text{threshold}$ are considered
3. *threshold*: Value defining how many harmonic or interaction tones are increased by *increase*. In [28] *threshold* equals five.
4. *fac_slope*: Factor adjusting proportionality from [28] to $(\text{fac_slope}/f)^5$.

Following the two step iteration, the final *SPL* is obtained by increasing all values by 0.001 dB until the primary computed *OASPL* (see section 5.1) is reached. This allows to estimate the third octave frequency spectrum for every observer angle.

Table presents the setting used hereafter to compute third octave band frequency, if not mentioned otherwise.

Table 5.2: General settings of 1/3-octave band function from [28]

<i>in_funda</i>	1
<i>increase</i>	1
<i>threshold</i>	5
<i>fac_slope</i>	$5 \cdot \text{BPF}_2$

5.3 Tonal Directivity

The noise emission of CROR is defined by various tonal components. However, each tone shows different characteristics in directivity. Figure 5.3 clearly shows that noise propagation strongly depends on the tone. For different observer locations, various noise levels are achieved for every tone. This section will present the directivity traits of CROR noise.

The directivity of individual tones can be predicted based on the Bessel Function of First Kind. Approximations of the directivity for the tones of fundamental BPF (first and second rotor) and the first interaction are shown in figure 5.4. Note: The graphs can be shifted in y-direction to adapt the dB-correction.

In order to replicate figure 5.4 the Bessel Function in form of equation 5.7 is applied:

$$J_m\left(\frac{kR\sin\theta}{1 - M_x\cos\theta}\right) \quad (5.7)$$

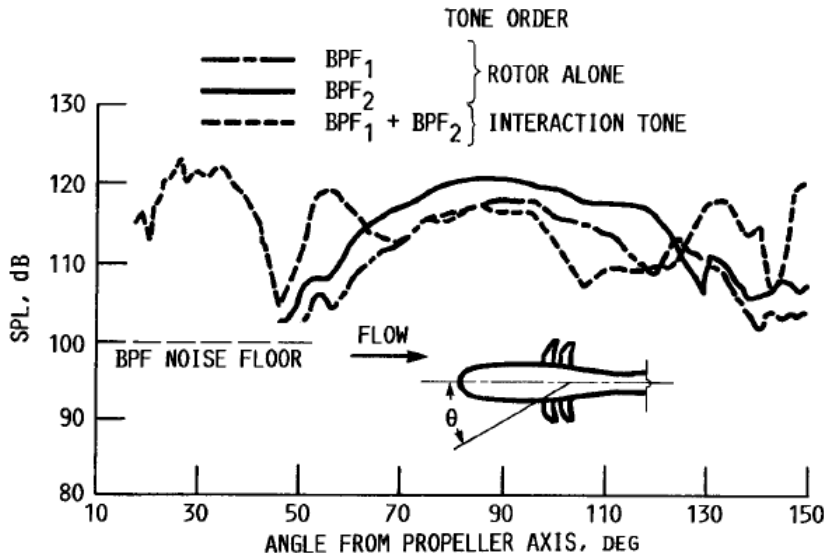


Figure 5.3: Tone directivity along a 137cm sideline (90° is aft rotor plane) [54]

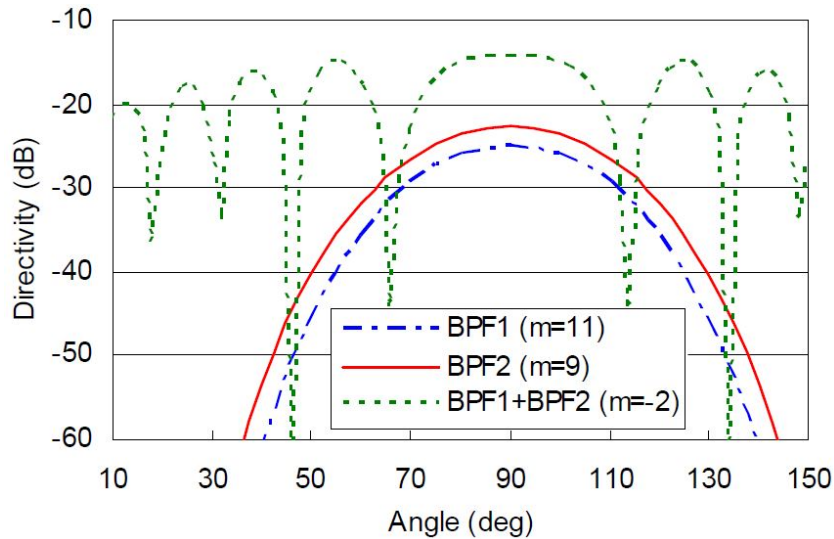


Figure 5.4: Directivity described by Bessel function [28]

with rotor radius, R , mode, m , and wave number, $k = 2\pi f/c$. Consequently, the Bessel Function of First Kind needs to be defined.

5.3.1 Bessel Function of First Kind

This subsection briefly presents the Bessel Function of the First Kind based on [1]. It is written in equation 5.8 and is crucial to noise simulation, as it approximates the directivity analysis of tonal sound propagation [28].

$$J_m(x) = \left(\frac{x}{2}\right)^m \sum_{k=0}^{\infty} \frac{(-1)^k}{k! \Gamma(m+k+1)} \left(\frac{x}{2}\right)^{2k} \quad (5.8)$$

The Bessel Function inherits the Γ -Function, which is presented in equation 5.9 [1]:

$$\Gamma(m+k+1) = (k+m)! \quad (5.9)$$

Hence, the final form of the Bessel Function is found to be equation 5.10:

$$J_m(x) = \left(\frac{x}{2}\right)^m \sum_{k=0}^{\infty} \frac{(-1)^k}{k!(k+m)!} \left(\frac{x}{2}\right)^{2k} \quad (5.10)$$

Figure 5.5 depicts the behaviour of $J_m(x)$ for $0 \leq m \leq 5$. The argument x is dependent on observer location and its relative speed to the noise source, when referred to equation 5.7 [1, 28].

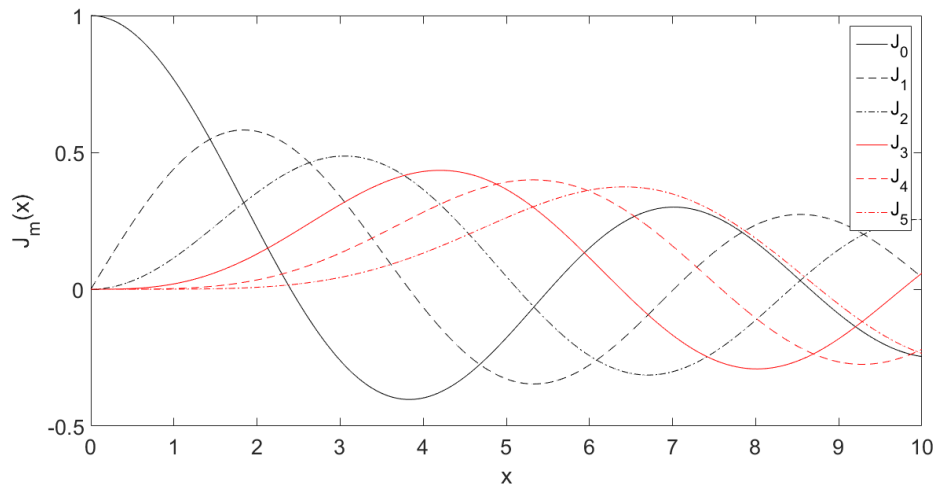


Figure 5.5: Bessel function for $0 \leq m \leq 5$

6

PARTNER Computations

The estimation of *OASPL* and tonal directivity are the essence of [28]. Nevertheless, CROR generate large numbers of tonal sound components, which are predominant and characteristic for the sound generation. These tones are the fundamental *BPF* of the front and rear rotor, their harmonics, and interaction tones. This chapter is divided in two sections. Section 6.1 explains the method developed in [32] to generate narrowband frequency spectra for CROR to clearly present the tonal noise emission. The broadband noise prediction developed in [32] is presented in 6.2.

6.1 Tonal Noise

This method is based on the work of McCurdy [33] in the late 80's and early 90's, when he experimentally defined the so called attenuation factor, M_n [32]. For tone numbers 1 to 30 the attenuation factors are listed in table 6.1. Higher tones are computed using the equation $\text{AttenuationFactor} = -58 - (\text{NumberOfTone} - 30) \cdot 2$.

Table 6.1: McCurdy relative attenuation factors [32]

Tone Number	Relative Attenuation										
1-10	0	-10	-4	-10	-7	-12	-18	-24	-20	-22	
11-20	-26	-28	-32	-26	-28	-30	-32	-34	-36	-38	
21-30	-40	-42	-44	-46	-48	-50	-52	-54	-56	-58	

Once the relative attenuation factor is defined, the initial *SPL* for each tone can be calculated using equation 6.1:

$$SPL = M_n \cdot TS_p \cdot TS_s \quad (6.1)$$

with the **tone scalar** for either front or rear rotor, TS_p (TS_f for front and TS_a for aft), and the given value for every third tone, TS_s , which is set to zero otherwise. The values for TS_p is either 1, 1.5, or 2 and for TS_s 1, 2, or 3 [32]. The final $OASPL$ is achieved through recurrent addition of 0.001 dB to the initial value. Therefore, it is necessary to calculate the $OASPL$ presented in section 5.1 prior the narrowband computations. Moreover, the theory of [32] is only used to generate the spectrum for an observer angle of 90 degrees. The properties of tonal directivity, based on the Bessel Function, presented in section 5.3 allows to correct the SPL level for every tone and any observer angle. Various examples of the prediction on basis of [32] are depicted in figure B.2-B.13 in appendix B.

6.2 Broadband Noise

It was found that the broadband noise can be resembled using a two system approach, based on **parabolic functions in logarithmic scale**. The formulation is presented in equation 6.2:

$$SPL = a \cdot \log(f)^2 + b \cdot \log(f) + c \quad (6.2)$$

The values a , b , and c are dependent on the BPF and Broadband Noise Level, BBL . ‘These two variables were used to determine the equation that would be used to govern the shape of the broadband noise. Based on the spectra published by Hoff et al., the broadband noise shape was approximated by a parabola on the logarithmic frequency scale with a modification made to the level at the frequency range before the peak of the parabola’ [32]. In that case a first order function in logarithmic scale is used to predict broadband noise ‘before the peak of the parabola’ [32]. This modification applies for BPF higher than 1000 Hz. Since it is unlikely to evaluate $BPF \geq 1000$ Hz with this tool, it can be neglected. Normally, BPF of 1 kHz or higher are achieved only in model scale experiments to ensure the blade tip Mach number complies to real size operation. The parabolas shaped with equation 6.2 for BBL of 65 and 80 are depicted in figure 6.1. Coefficients a , b , and c are retrieved from [32] and listed in table 6.2.

Table 6.2: Coefficients for broadband noise from [32]

BBL	a	b	c
65	-27	124.25	-85.95
80	-50.51	241.33	-216.27

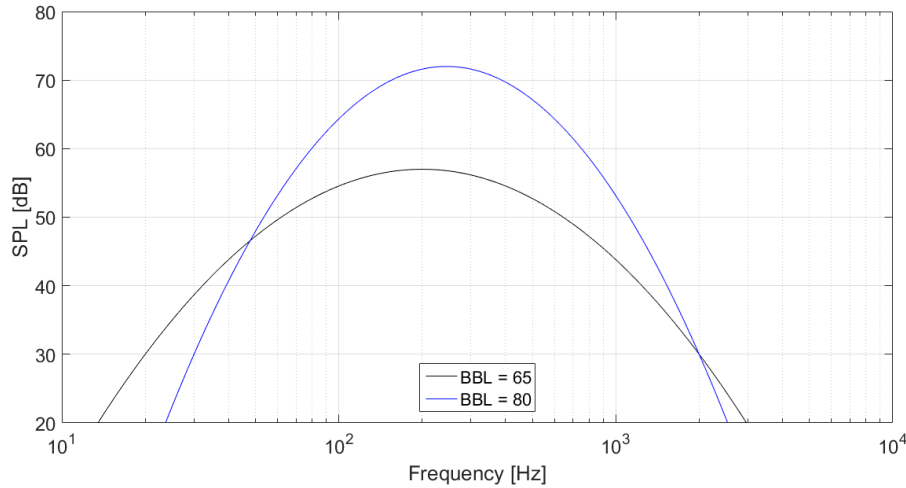


Figure 6.1: Broadband noise prediction of CROR noise based on [32]

In order to not be limited to two *BBL* values, a determination of coefficients can be achieved by optimising the function to fit through the data points given by tonal noise. The initial values are chosen such that they are in between the coefficients from table 6.2: $a = -40$, $b = 180$, and $c = -150$.

Once the graph is determined for observer angle of 90° , random noise of ± 4 dB is added. After that, the broadband noise is reduced such that its maximum value is 20 dB below the peak value of *BPF*. Subsequently, for any observer angle evaluated, the same broadband noise shape is applied. However, its *SPL* is reduced by the difference determined between the observer angle under investigation and 90° of the *OASPL* previously calculated.

7

Hanson Model

This chapter presents Hanson's formulation to compute the noise emission for any given CROR. The motivation of choosing this analytical prediction theory is found in [49]: 'Hanson's prediction recovers the levels and its shape goes through the experimental scatter.' Therefore, **Hanson**'s formulation promises to return good results for an in-design tool.

Sound pressure generation in time domain was analysed by Hanson [14–17], who defines the acoustic pressure signal for general counter rotating far-field case by (un)steady loading noise or aerodynamic noise. **Quadrupole noise due to non linear effects, which is significant at transonic and supersonic tip speeds is neglected** [12]. Hanson discretises the blade radially to **match the input of quasi-steady aerodynamic loads** [12]. This leads to the discrete noise at the blade passing frequency and its higher harmonics in the frequency-domain. Hanson theory is captured in equation 7.1, which defines the acoustic pressure signal:

$$p = \frac{-i\rho c^2 B_2 \sin\theta}{8\pi(r_1/D_2)(1-M_x \cos\theta)} \cdot \sum_{m=-\infty}^{\infty} \sum_{k=-\infty}^{\infty} e^{i[(mB_2 - kB_1)(\phi - \phi^{(2)} - \frac{\pi}{2}) + (mB_2\Omega_2 + kB_1\Omega_1)(\frac{t}{c} - t)]} \\ \int_{root}^{tip} M_r^2 e^{i(\phi_d + \phi_s)} \cdot J_{mB_2 - kB_1} \left(\frac{(mB_2 + kB_1\Omega_{12})z_0 M_T \sin\theta}{1 - M_x \cos\theta} \right) \\ \left(k_x \frac{C_{Dk}}{2} \psi_{Dk}(k_x) + k_y \frac{C_{Lk}}{2} \psi_{Lk}(k_x) \right) dz_0 \quad (7.1)$$

with constant parameters, density of air, ρ , speed of sound in air, c , observer constant sideline distance, r_1 , propeller diameter of second rotor, D_2 , flight Mach number, M_x , num-

bers of blades on first rotor, B_1 , and second rotor, B_2 , first and second rotor angular speed, Ω_1 and Ω_2 respectively, ratio of rotational speeds Ω_{12} , angular observer angle, ϕ , angular blade angle at initial time, $\phi^{(2)}$, for a definite CROR.

Dividing equation 7.1 into two parts, a leading factor and a summation of an exponential function multiplied by an integral are obtained. The leading factor is dependent on observer angle, θ , only, whereas the summation over the order of sound harmonic, m , and load harmonic, k , is also a function of the evaluation time, t , and the ratio of source over tip radius, z_0 .

If the leading factor of Hanson's formulation is investigated for a definite CROR individually, the information captured in equation 7.2 can be considered:

$$g(\theta) = \frac{\sin\theta}{1 - M_x \cos\theta} \quad (7.2)$$

Equation 7.2 shows that the observer angle for which maximum value of $g(\theta)$ is achieved, depends on Mach number only. For a stationary aircraft ($M_x = 0$) the maximum acoustic pressure is radiated at an angle of 90 degrees, which is perpendicular to flight direction, i.e. in plane of rotation. For increasing Mach number, the radiation angle reduces at which the maximum value of equation 7.2 is obtained, hence it is expected that the maximum acoustic pressure value moves upstream with increasing flight Mach number. Figure 7.1 depicts the results of equation 7.2 for different flight Mach numbers. The maximum value is indicated by 'x' in the graphs of figure 7.1.

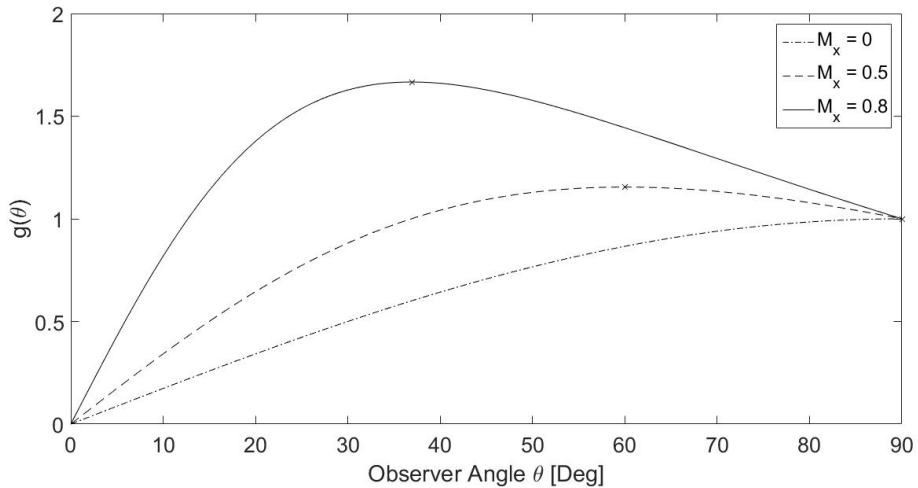


Figure 7.1: Forward movement of loading noise lobe peak value for a CROR

In agreement, the analysis of prop fan directivity patterns in [14] shows the forward movement of the loading noise peak value for higher flight Mach number.

Further, the directivity is described by the integral contained in summation over m and k . The exponential is a function of phase angles, which are associated with sweep and offset, ϕ_s and ϕ_o , respectively. ‘Blade sweep and offset appear explicitly as phase lag effects’[15], whose influence on sound pressure varies depending on observer position. Both parameters are defined in equations 7.3 and 7.4. The blade section relative Mach number of rotor two, M_r , is evaluated in dependence of z_0 .

$$\phi_s = 2 \frac{M_T}{M_r} \left(\frac{mB_2 + kB_1\Omega_{12}}{1 - M_x \cdot \cos(\theta)} - kB_1(1 + \Omega_{12}) \right) \frac{MCA}{D_2} \quad (7.3)$$

$$\phi_o = \frac{2}{M_r} \left(\frac{(mB_2 + kB_1\Omega_{12})M_T^2 z_0 \cos(\theta)}{1 - M_x \cdot \cos(\theta)} - \frac{(mB_2 - kB_1)M_x}{z_0} \right) \frac{FA}{D_2} \quad (7.4)$$

where the Mid Chord Alignment, MCA , defines the sweep and the Face Alignment, FA , the offset or change due to dihedral angle of the blade on rotor two.

The Bessel Function of First Kind is explained in subsection 5.3.1. It is incorporated to characterise the directivity of sound and is further dependent on blade tip rotational Mach number of rotor two, M_T . Lastly, the aerodynamic properties of the CROR are evaluated. The wavenumbers, k_x and k_y , are defined in equations 7.5 and 7.6, respectively:

$$k_x = 2 \frac{M_T}{M_r} \left(\frac{mB_2 + kB_1\Omega_{12}}{1 - M_x \cdot \cos(\theta)} - kB_1(1 + \Omega_{12}) \right) B_D \quad (7.5)$$

$$k_y = -\frac{2}{M_r} \left(\frac{(mB_2 + kB_1\Omega_{12})M_T^2 z_0 \cos(\theta)}{1 - M_x \cdot \cos(\theta)} - \frac{(mB_2 - kB_1)M_x}{z_0} \right) B_D \quad (7.6)$$

For $C_{Dk} = C_{Lk} = 0$ and $k \neq 0$ equation 7.1 presents steady loading. Factors C_{Dk} and C_{Lk} are the k th drag and lift harmonic coefficient, respectively. [16] Both are dependent on the aerodynamic characteristics of both, the first and second rotor. The wake created by the first rotor impinges on the second rotor, changing the aerodynamic pressure distribution due to change in local angle of attack and turbulence, i.e. tip vortices. The obtained change in pressure on the second blade set is related to the aerodynamic properties of the second rotor. The first rotor’s influence onto the second rotor is known as aerodynamic interference. These ‘unsteady effects are accounted for by taking into account the angular inflow on the propeller’[12]. In equation 7.1 ‘the blade is discretised radially to match the input of the quasi-steady aerodynamic loads’ [12], and is represented by z_0 in the integration over z_0 with lower and upper boundaries blade hub and tip, respectively. The angular correction is approximated using the axial induction factor obtained from JBlade (more information on JBlade see chapter 9). The axial induction factor, a , is defined in equation 7.7 [44]:

$$V = V_\infty \cdot (1 + a) \quad (7.7)$$

which ultimately leads to the new angle of attack for blades in an upstream wake, as depicted in figure 7.2.

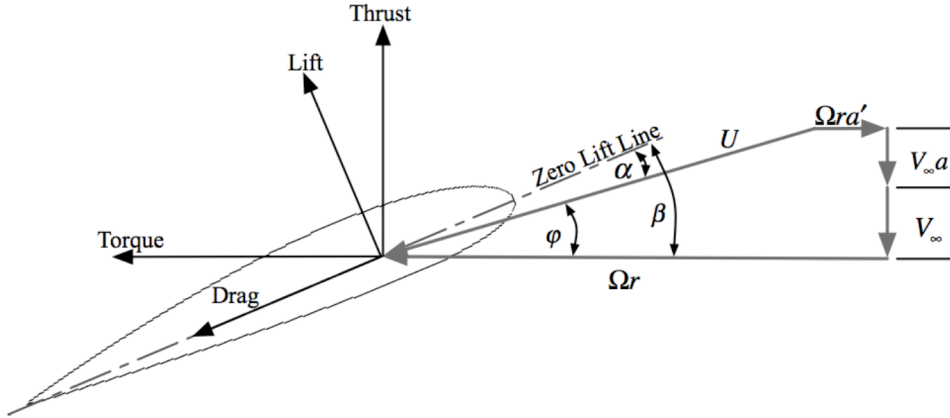


Figure 7.2: Effect of axial induction on local blade angle of attack [44]

The change in angle of attack influences the value of C_{Lk} and C_{Dk} directly. However, [49] showed that the harmonic loading is strictly dependent on its order. ‘The first four loading harmonics, thereafter noted 0BPF, 1BPF, 2BPF, and 3BPF are presented in [figure 7.3] for each rotor blade’ [49]. ‘Load harmonic 0BPF is the steady loading of the blade. [...] Soulard et al. showed that all higher harmonics had the same shape and order of magnitude as the third harmonics 3BPF’ [49].

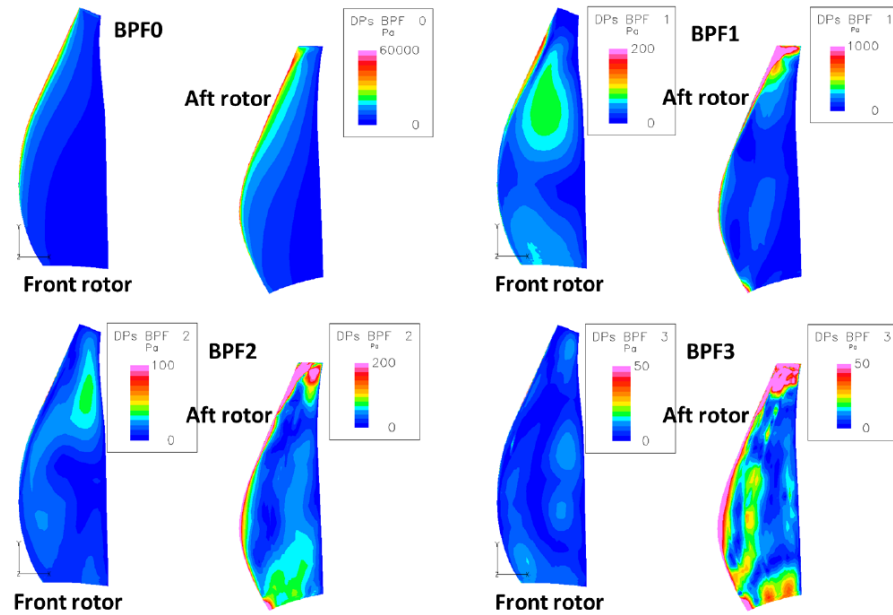


Figure 7.3: Blade pressure distribution first four loading harmonics [49]

Approximating the content of figure 7.3 for the entire blade, leads to correction factors for the value of C_{Lk} and C_{Dk} inserted in equation 7.1 according to the harmonic in evaluation. All multiplication factors of C_{Lk} and C_{Dk} are listed in table 7.1.

Table 7.1: Correction of higher load harmonics

Order of Load Harmonic	Multiplication Factor
0	Reference = 1
1	$\frac{1}{60}$
2	$\frac{1}{300}$
≥ 3	$\frac{1}{1200}$

Further, equation 7.1 depends on the normalised loading distribution functions ψ_{Lk} and ψ_{Dk} , modelling the lift and drag, respectively. In [19] Hanson gives the lift distribution which is depicted in figure 7.4. The incorporated lift loading distribution is shown in figure 7.5. The drag loading distribution is assumed to be constant throughout the chord length and also depicted in figure 7.5.

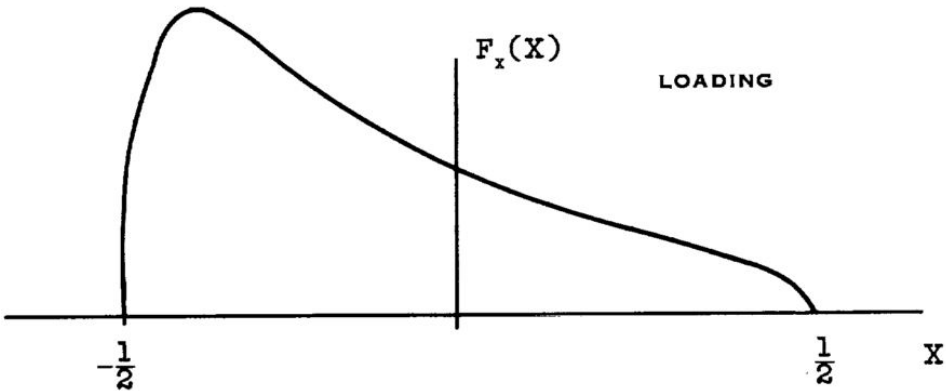


Figure 7.4: Normalised loading distribution function from [19]

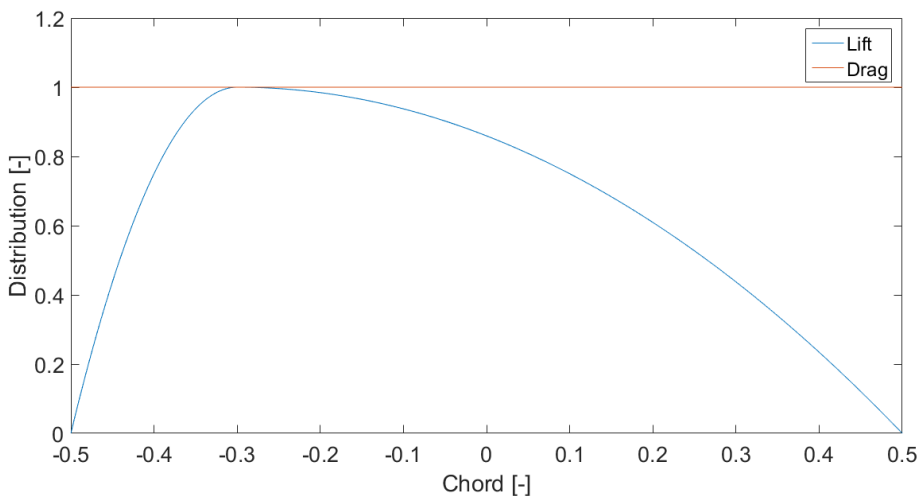
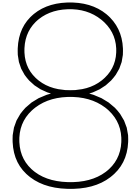


Figure 7.5: Normalised lift and drag loading distribution function applied

Finally, the pressure signal is dependent only on observer angle and evaluation time.

After applying a Fast Fourier Transform (FFT) for the observer angle of interest, the frequency spectrum is obtained.

Aircraft noise certification and airport measurements are performed at distances of some hundred meter, at which atmospheric attenuation is a major noise reduction factor for high frequencies. **Hanson's method does not include this attenuation of sound. Therefore, the change in SPL needs to be incorporated.**



Atmospheric Attenuation

Atmospheric attenuation describes the process of sound energy absorption as sound is travelling through atmosphere. The atmospheric attenuation in sound pressure level, Δ_{SPL} in the unit of dB is given by equation 8.1:

$$\Delta_{SPL} = \alpha_{at} \cdot \frac{r}{100}; \quad (8.1)$$

where r is the distance between observer and sound source. The sound attenuation coefficient, α_{at} , of unit dB/100m is dependent on the atmospheric properties, that is ambient air temperature, T , in degrees Celsius, and humidity, H , in percent. Moreover, the sounds frequency is a mayor factor of the magnitude of atmospheric attenuation. The sound attenuation coefficient is defined in equation 8.2:

$$\alpha_{at} = 10^{2.05 \cdot \log_{10}\left(\frac{f_0}{1000}\right) + 1.1394 \cdot 10^{-3} \cdot T - 1.916984} + \eta \cdot 10^{\log_{10}(f_0) + 8.42994 \cdot 10^{-3} \cdot T - 2.755624} \quad (8.2)$$

with the applied frequency, f_0 , and multiplication factor, η , which is solely a function of the parameter δ (equation 8.3):

$$\delta = \sqrt{\frac{1010}{f_0}} \cdot 10^{\log_{10}(H) - 1.328924 + 3.179768 \cdot 10^{-2} \cdot T} \cdot 10^{-2.173716 \cdot 10^{-4} \cdot T^2 + 1.7496 \cdot 10^{-6} \cdot T^3} \quad (8.3)$$

For a computed δ , a corresponding value of η can consequently be extracted from table 8.1.

The applied frequency, f_0 , varies depending on the sound frequency. Based on [43] for frequencies below 4000Hz the relation $f_0 = f$ is assumed to be applicable. For the interval

Table 8.1: Relation between δ and η [43]

δ	η	δ	η	δ	η	δ	η
0.000	0.000	1.000	1.000	2.30	0.495	4.450	0.245
0.250	0.315	1.100	0.970	2.50	0.450	4.800	0.230
0.500	0.700	1.200	0.900	2.80	0.400	5.250	0.220
0.600	0.840	1.300	0.840	3.00	0.370	5.700	0.210
0.700	0.930	1.500	0.750	3.30	0.330	6.050	0.205
0.800	0.975	1.700	0.670	3.60	0.300	6.500	0.200
0.900	0.996	2.000	0.570	4.15	0.260	7.000	0.200

of $4000 \text{ Hz} < f \leq 5000 \text{ Hz}$ it is assumed $f_0 = f \cdot 0.5 + 2000 \text{ Hz}$. At higher frequency values relation $f_0 \approx f \cdot \frac{9}{10}$ is applied. Therefore, f_0 is computed using equation 8.4:

$$f_0 = \begin{cases} f, & f \leq 4000 \text{ Hz} \\ f \cdot 0.5 + 2000 \text{ Hz}, & 4000 < f \leq 5000 \text{ Hz} \\ f \cdot \frac{9}{10}, & 5000 \text{ Hz} < f \end{cases} \quad (8.4)$$

9

JBlade

The aerodynamic properties of the first rotor, that will effect the operations of the second rotor are computed using JBlade. It is an open source propeller analysis program ‘based on David Marten’s QBLADE and André Deperrois’ XFLR5’ [35]. JBlade estimates ‘the performance curves of a given propeller design’ [35].

JBlade generates the airfoil aerodynamic characteristics using XFLR5, which includes ‘XFOIL’s Direct and Inverse analysis capabilities’ [6]. In 2013, [47] found that ‘XFOIL does not show a significant difference in the resulting airfoil polars’, for more than 200 airfoil coordinates. Therefore in JBlade, ‘each airfoil should be redefined to that number of points’ [47].

The simulation is executed for two 9-bladed propeller with twist of 37.5° and blade length of 1 m. The chosen airfoils are NACA0012 (symmetric) and NACA1412 (cambered). All initial settings are kept, including a Reynolds number of 10^6 . The airfoils were analysed for angles of attack from -4° to 8° with a step size of 0.2° . The propeller was then evaluated for the data given in table 9.1.

Table 9.1: Analysis conditions for propeller in JBlade

Airspeed [m/s]	Rotational Speed [rpm]	Blade Pitch [$^\circ$]
30-60	1000	0
60-80	1000	10
80-90	1000	15
90-110	1000	20
110-160	1500	20

The rotational speed and blade pitch were chosen such that the maximum propulsive efficiency was obtained for the next airspeed interval. The width also depends on the performance of propeller, i.e. the propulsive efficiency. For the given inputs a span wise distribution of the axial induction factor is obtained, which in conclusion leads to the new angle of attack for the downstream propeller blade, as explained in chapter 7.

Lastly, after setting all input parameters, the final blade plan forms have to be shaped. The mockup of F7 and patented blades resembled and analysed in JBlade are shown in figures 9.2 and 9.4. Both plan forms are generated with 13 sections. The spacing between two subsequent sections is maximum at root and minimum at tip. Accordingly, figure 9.1 and 9.3 original blade model. Due to the close resemblance of F7 to SR3 blade, the axial induction factor data generation for SR3 is ignored. Instead the data produced for F7 blade is used.

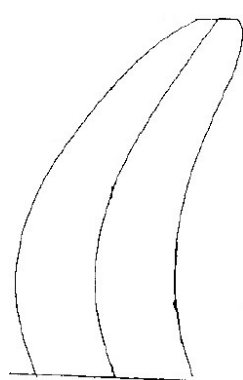


Figure 9.1: F7 blade from literature [22]

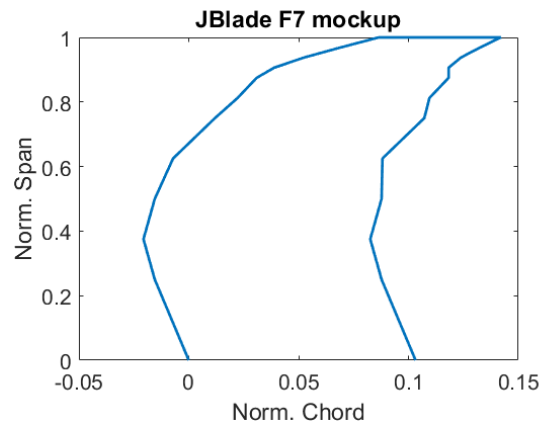


Figure 9.2: Mockup in JBlade for F7 blade

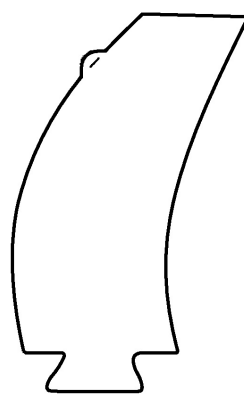


Figure 9.3: Patented blade from literature [50]

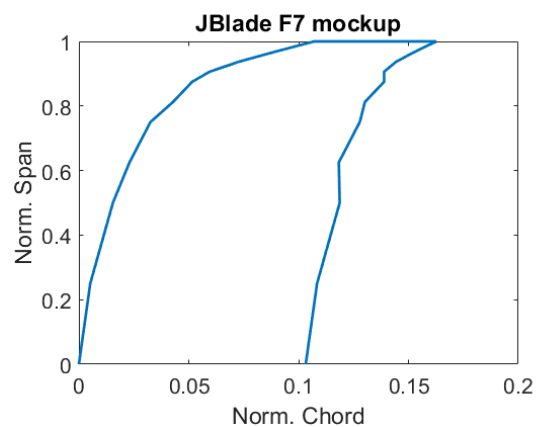


Figure 9.4: Mockup in JBlade for patent blade

III

Noise Prediction Tool

10

Tool Initiation

In the forgoing chapters, the program's methodologies for computing CROR noise emission are presented. The methods are incorporated in the tool and can be executed electively. The election is dependent on the users interest and/or input data. This chapter presents the operation principle of the developed program and the scenarios for choice of method. Flow charts help to understand the computational process. The tool developed during this project is written in Matlab-software version R2015b.

In general, the tool is based on the methods of Lewy, PARTNER, and Hanson. A two way computation is chosen to increase the range of applicability and allow for fast and accurate computations. Lewy and PARTNER lead to a semi-empirical tool, whereas Hanson gives the theory for a generally valid analytical tool predicting (un-)steady aerodynamic loading noise. The execution of either tool's routine is started by the initiator, see figure 10.1.

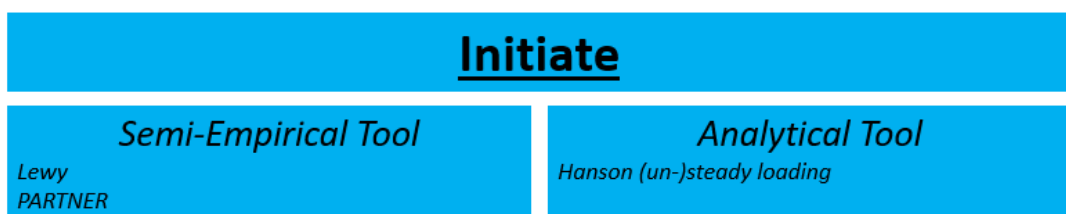


Figure 10.1: Initiation instant of prediction tool

10.1 Initiator

The initiator (*Initiate.m*) is the starting point of evaluation. According to user settings and input data, it launches the computational routine to be executed. In total two different

evaluation methods are available. If the semi-empirical model is wished to be evaluated, $\text{Eval_Op} = 1$. In order to evaluate the analytical tool, Eval_Op is defined to be 2. The methodology of both routines is found in part II.

The program has different analysis setting that are to be changed in the tool's initiator. Always true is the reference value of sound pressure, $p_{e0} = 2 \cdot 10^{-5}$. Further settings are user adaptable and listed with the proposed value in table 10.1. The upper half of table 10.1 is generally valid. If the analytical routine is chosen to be evaluated, the bottom half of table 10.1 is additionally used and the value of m is updated accordingly. Since the Nyquist frequency (half of sample frequency f_s) is the upper limit of the to be produced frequency spectrum, also the upper limit of sound harmonic is dependent on Nyquist frequency. Therefore, two dependencies for the upper value of sound harmonics are found, which are BPF and Nyquist frequency. In table 10.1, let parameter a define the upper limit of sound harmonics. Then a is defined by the Nyquist frequency, divided by the sum of blade passage frequencies and finally rounded towards negative infinity, which is formulated in equation 10.1:

$$a = \left\lfloor \frac{f_s \cdot 0.5}{BPF_1 + BPF_2} \right\rfloor \quad (10.1)$$

Table 10.1: List of settings for CROR noise prediction tool

For $\text{Eval_Op} = 1$		
Sound harmonic	m	$[0 : a]$
Sample frequency [Hz]	f_s	20000
Frequency resolution [Hz]	df	8
For $\text{Eval_Op} = 2$		
Load harmonic	k	$[-20 : 50]$
Sound harmonic	m	$[-10 : a]$
Blade section indicator	$z_0_divisor$	15
Reynolds number	Re_x	$1E6$

Blade layout and aerodynamic properties are required to evaluate Hanson computations. If the value of blade section indicator increases, so does the amount of blade sections that are evaluated. The aerodynamic properties of a blade are evaluated using pre-generated data from JBlade (axial induction factor), which is explained in chapter 9. The data of axial induction factor is imported contemporary with the values from input file by using script *readinput.m*.

Once the input values are saved, the blade tip rotational Mach number is compared to warn the user with a statement about the reliability of the output data. If Hanson is the chosen routine and flight Mach number (M_x) is higher than 0.8 or blade tip Mach number

(M_T) is higher than 0.97 a warning is displayed and the routine is changed to $\text{Eval_Op} = 1$. Another warning is displayed in case that $M_x \geq 0.5$. However, no change to Eval_Op is prompt. Lastly, if flight speed (v_0) is below $30 \frac{\text{m}}{\text{s}}$, a warning for to low flight speed is shown. Again, Eval_Op remains unchanged. The full list of warning options is presented in table 10.2.

Table 10.2: List of warnings for CROR noise prediction tool if $\text{Eval_Op} = 2$

Parameter	Statement in Display	Change in Eval_Op
$M_x > 0.8$	<i>Only Choose Mach number M_x below 0.8</i>	Yes
$M_T > 0.97$	<i>Only Choose Mach number M_T below 0.97</i>	Yes
$M_x \geq 0.5$	<i>Choose Mach number M_x below 0.5 for more accurate aerodynamics</i>	No
$v_0 < 30$	<i>Choose $M_x \geq 30/c$ for more accurate aerodynamics</i>	No

After all values are saved, *Initiator.m* calls the designated tools folder and runs its main file (*main.m*). The flow chart of *Initiator.m* is depicted in figure 10.2 obeying left-right and top-down chronology. Therefore, *readinput.m* is called before *main.m* and *atmosphere.m* after *Input.txt* while *readinput.m* is evaluated.

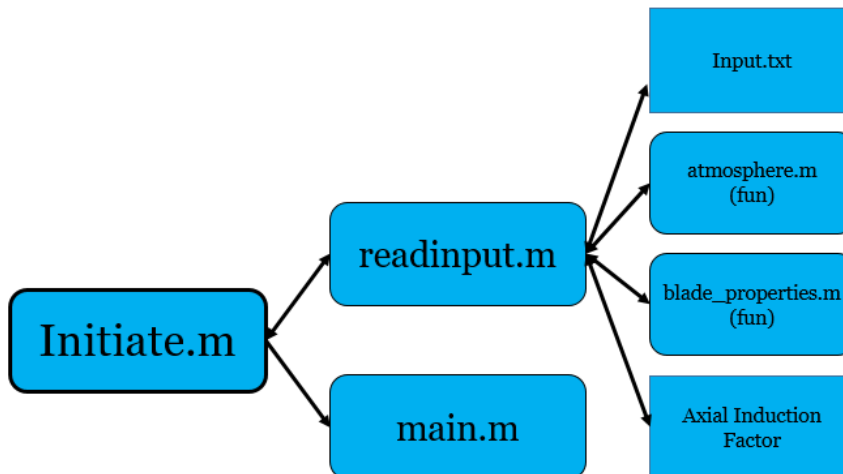


Figure 10.2: Computational structure of initiation instant

Moreover, result display can be adjusted for every figure individually. For both Eval_Op settings a total of eight plot handles are available. Their names are self explanatory, nonetheless one example each for all resulting figures are listed in appendix A, which is specifically established to support the understanding.

11

Input Definition

Before initiating the program's routine, the input file has to be understood and if demanded rewritten. For the assessment of CROR noise emission, various parameters of influence have been determined. This chapter explains the format and syntax of the input file.

Typically, aircraft optimisation routines are fed with .dat or .txt files. These formats feature simple layout and fast processing capabilities regardless of operation. Both, manual and automate operation is straightforward and unlikely to be misused. The file is divided into three subsections, that is atmospheric conditions, CROR geometry, and analysis conditions. Moreover, the program results for each routine depend on different values. If the semi-empirical tool is called, the values listed in table 11.1 under 'Semi-Empirical Tool' are demanded, otherwise the values under 'Analytical Tool' are used. A table row is marked with 'n/a' if the value does not affect the result of a program's routine.

The atmospheric conditions are important for both Tools. Speed of sound at any given altitude is directly or indirectly dependent on all atmospheric conditions listed except humidity of air, which is only needed to account for atmospheric attenuation. However, only the frequency spectrum generated by the analytical tool is atmospherically attenuated. The CROR data is divided into three sections: General, first rotor only, and second rotor only. It is assumed that the CROR data input is clear. Since most engines are rated by thrust output, the value for mechanical shaft power has to be approximated in case thrust is the available parameter only. For non-zero flight speeds, with thrust in N an approximation of the shaft power in kW is obtained by equation 11.1:

$$W_{mec} = T \cdot \frac{c \cdot M_x}{1000} = T \cdot \frac{\nu_0}{1000} \quad (11.1)$$

Table 11.1: Required input data of prediction tool

Input	Semi-Empirical Tool [Unit]	Analytical Tool [Unit]
Atmospheric Conditions		
Sea Level Temperature	[K]	[K]
Sea Level Pressure	[Pa]	[Pa]
Specific Heat Ratio	[-]	[-]
Specific Heat Difference	[J kg ⁻¹ K ⁻¹]	[J kg ⁻¹ K ⁻¹]
Gravitational Constant	[m s ⁻²]	[m s ⁻²]
Temperature Laps Rate	[K m ⁻¹]	[K m ⁻¹]
Humidity of Air	n/a	[%]
CROR Data		
Mechanical Shaft Power	[kW]	n/a
Rotor Spacing Fraction	[-]	n/a
True Rotational Speed	[%]	n/a
Blade Type	n/a	[Name]
Airfoil	n/a	[Camber]
Rotor One		
Blade number	[-]	[-]
Rotational Speed	[Hz]	[Hz]
Diameter at Tip	[m]	[m]
Diameter at Hub	n/a	[m]
Root Chord / Diameter	n/a	[-]
Rotor Two		
Blade number	[-]	[-]
Rotational Speed	[Hz]	[Hz]
Diameter at Tip	[m]	[m]
Diameter at Hub	n/a	[m]
Root Chord / Diameter	n/a	[-]
Analysis Conditions		
Sideline Distance	[m]	[m]
Flight altitude	[m]	[m]
Flight Mach Number	[-]	[-]
Observer Angle	[°]	[°]

with thrust, T , and flight speed, v_0 . Further, rotor spacing is normalised by the second rotor tip diameter and the true rotational speed is given as a fraction of the maximum achievable speed of the second rotor. Since the analytical method developed by Hanson is based on aerodynamic properties of the rotor blades, a data base of currently three different geometries is set up. The name listed in input file calls the blade properties, which

are later discretised in sections depending on $z_0_divisor$. This is irrelevant for the semi-empirical tool. Every original blade is shown in figures 11.1, 11.3, and 11.5. The reproduced blades from data called during computations in Matlab are depicted in figures 11.2, 11.4, and 11.6. Blade mid-chord and pitch axis are also plotted.

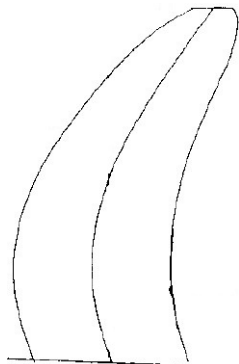


Figure 11.1: F7 blade from literature [22]

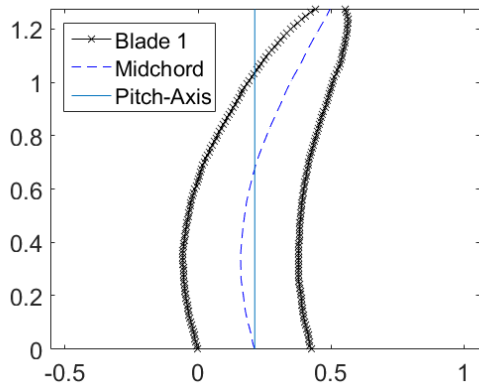


Figure 11.2: F7 blade reproduced in Matlab

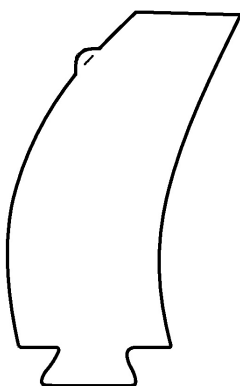
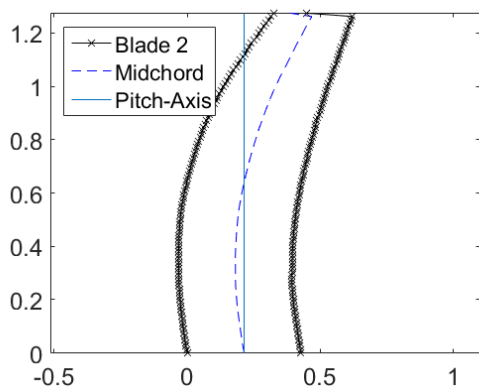


Figure 11.3: Patented blade from literature [50] Figure 11.4: Patented blade reproduced in Matlab



Lastly, the analysis conditions need to be defined. Sideline distance and observer angle purely refer to the location, that is distance of travelled sound and direction of emission. Flight altitude and Mach number refer to the engine operation, independent of the observer location.

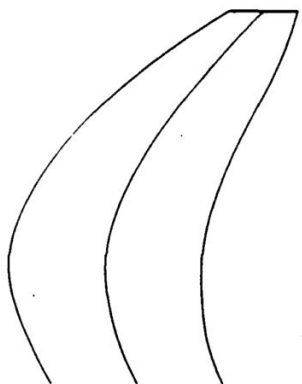


Figure 11.5: SR3 from literature [51]

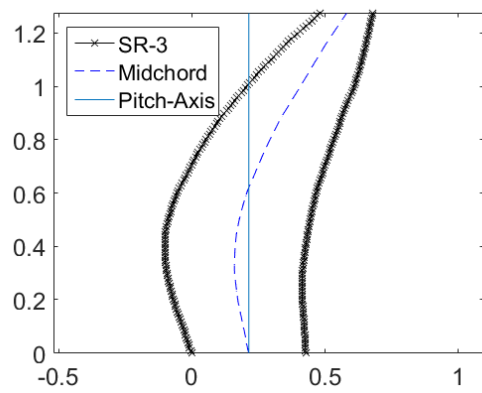


Figure 11.6: SR3 blade reproduced in Matlab

12

Semi-Empirical Tool

This chapter presents the structure and main functions executed during evaluation of the semi-empirical tool. Its flow chart is presented in figure 12.1. The chart is read from left to right and top-down, thus *LewyDirectivity.m* in *Lewy.m* is evaluated first, followed by *LewyThirdOctave.m*. Afterwards, *Partner.m* is evaluated, starting with *PARTNERNarrowband.m*.

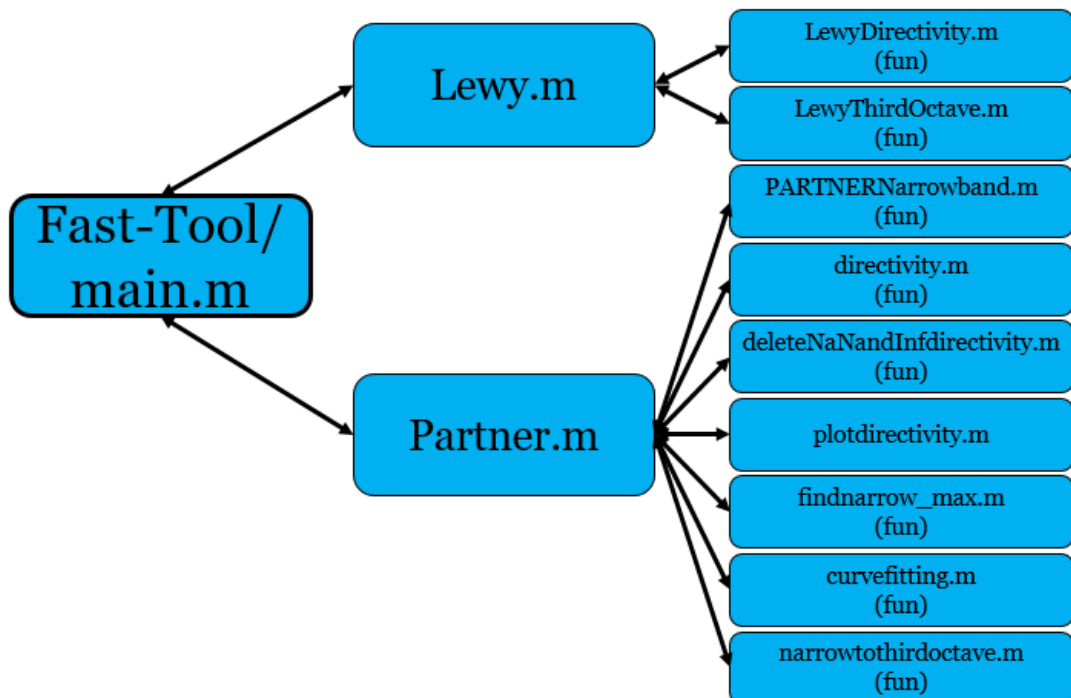


Figure 12.1: System structure of semi-empirical tool

The most crucial functions called, while evaluating the semi-empirical tool, are ex-

plained in this chapter. The chapter is structured in sections, which appear in chronological order of the files execution.

12.1 Generation of OASPL-Directivity

This section explains function *LewyDirectivity.m*. The equations implemented are fully listed and explained in chapter 5. All inputs and outputs of this functions are listed in table 12.1. It is the first function called during evaluation of the semi-empirical method. Its output *OASPL* is relevant for all succeeding functions included in the semi-empirical tool. All subsequent *SPL*-directivity is scaled based on the values returned from this function. Note, the value of *OASPL* is for constant sideline, thus distance towards the engine is smallest at an observer angle of 90° and increases when moving aft or forward along the sideline. Constant distance for any observer angle is true for *polarOASPL*. Independently of the user's input, *OASPL* is evaluated for observer angles $0^\circ - 180^\circ$ in step of 1° . However, computations are executed in radians.

Table 12.1: Input and output data of Lewy-OASPL-directivity function

<i>LewyDirectivity.m</i>			
Input		Output	
Type	Unit	Type	Unit
θ^*	rad	<i>OASPL</i>	dB
B_1	-	<i>polarOASPL</i>	dB
B_2	-		
D_2	m		
r_1	m		
W_{mech}	W		
S	-		

*Fixed to vector $0 : \pi/180 : \pi$

12.2 Lewy 1/3-Octave Band Frequency Spectrum

In order to predict the third octave band frequency spectrum based on Lewy [28], the function *LewyThirdOctave.m* is used. The function's settings and their influence on the output are visualised in this section. Table 12.2 contains all in- and output parameters of this function.

In section 5.2 the setting parameters have been explained in detail. Moreover, their standard values are listed in table 5.2. All parameters are examined for CROR of equal blade

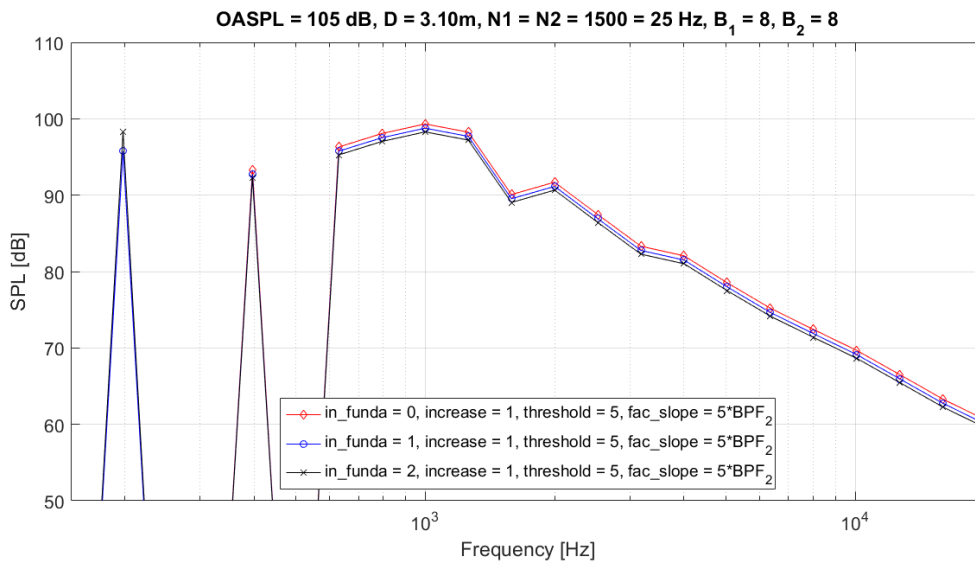
Table 12.2: Input and output data of Lewy 1/3-octave frequency spectrum function

LewyThirdOctave.m			
Input		Output	
Type	Unit	Type	Unit
Harmonics*	-	<i>SPL</i>	dB
B_1	-	f	Hz
B_2	-		
D_2	m		
Ω_1	Hz		
Ω_2	Hz		
<i>OASPL</i>	dB		
c	m s^{-1}		

*Fixed to value 120

count, $B_1 = B_2 = 8$, and different blade count, $B_1 = 11$ and $B_2 = 9$. Additionally, the values of $OASPL = 105$ dB, $D_2 = 3.10$ m, $\Omega_1 = \Omega_2 = 25$ Hz, and $c = 340$ m s $^{-1}$ complete the input.

Firstly, the influence of setting value *in_funda* is evaluated for both CROR geometries. Figure 12.2 presents the spectral change for CROR with $B_1 = B_2$. As expected, for *in_funda* = 0 the fundamental frequency is not appearing. For increasing values of *in_funda* the fundamental frequency raises in *SPL*. In turn, all other values will reduce to maintain the *OASPL* value.

Figure 12.2: Effect of *in_funda* on 1/3-octave band frequency spectrum for $B_1 = B_2$ after [28]

The phenomena traced in figure 12.2 are also visible in 12.3. For both blade counts the

same explanation holds.

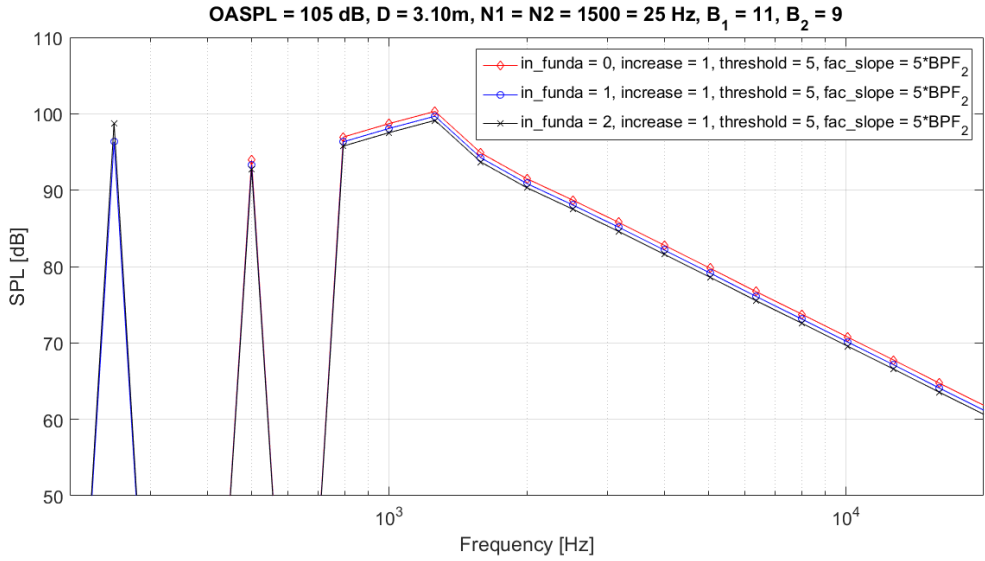


Figure 12.3: Effect of *in_funda* on 1/3-octave band frequency spectrum for $B_1 = B_2 + 2$ after [28]

Next, parameter *increase* is analysed. Its affect on the tonal noise is limited by *threshold*. For this analysis *threshold* = 5, hence for $B_1 = B_2 = 8$ all frequencies (excluding fundamental) up until $B_2 \cdot \Omega_2 \cdot \text{threshold} = 8 \cdot 25\text{Hz} \cdot 5 = 1000 Hz are influenced by *increase*. Figure 12.4 confirms this theory: For *increase* = 0 frequencies (excluding fundamental) higher 1000 Hz are audible. If *increase* = 1, tones at 200 Hz, 400 Hz, 600 Hz, and 800 Hz, are incorporated into the third octave band frequency spectrum as expected. For rising value of *increase*, those frequencies will grow in *SPL*. Consequently, the *SPL* will reduce for all higher frequencies and the fundamental to result in the required *OASPL*.$

Analogous, figure 12.5 depicts the behaviour of a CROR with blade count $B_1 = B_2 + 2$. However, here the limiting frequency for *increase* = 0 is $B_1 \cdot \Omega_1 \cdot \text{threshold} = 11 \cdot 25\text{Hz} \cdot 5 = 1375$ Hz.

The task of *threshold* was broached already during evaluation of *increase*. However, the influence of changing its value was not investigated yet. Again, first blade count $B_1 = B_2$ is considered, before $B_1 = B_2 + 2$ is investigated. Figure 12.6 shows the graphs for values of 2, 5, and 10. For *threshold* = 2 only a frequency value of $B_2 \cdot \Omega_2 \cdot \text{threshold} = 8 \cdot 25\text{Hz} \cdot 2 = 400$ Hz is treated with *increase*. Accordingly, the highest peak can be found at a frequency value of 600 Hz. The graph for *threshold* = 5 is equal to the previous figures. Its maximum value is therefore at 1000 Hz. The frequency of 2000 Hz is the limiting value for *threshold* = 10, thus the containing band reaches maximum value.

Again, same logic for different frequencies is reflected in figure 12.7, showing the frequency spectra for blade counts $B_1 = B_2 + 2$.

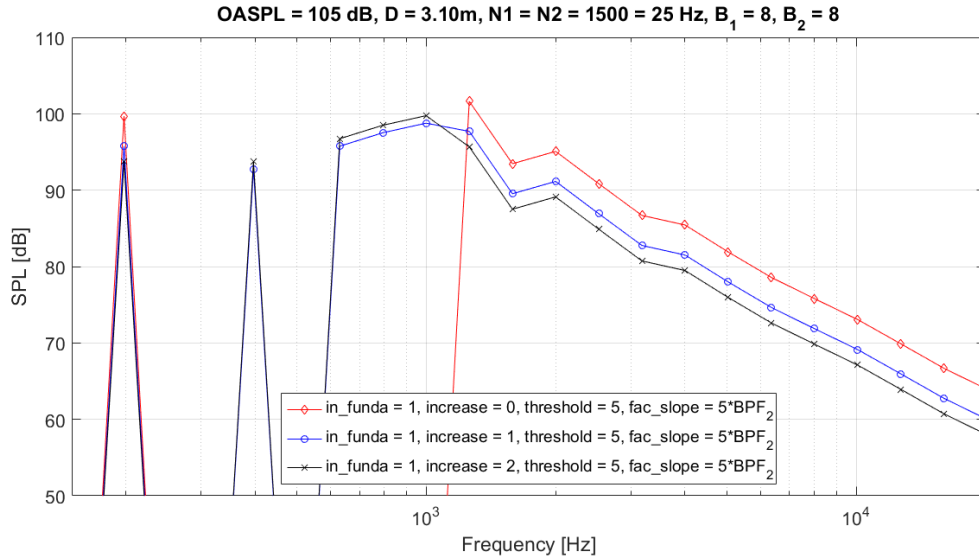


Figure 12.4: Effect of increase on 1/3-octave band frequency spectrum for $B_1 = B_2$ after [28]

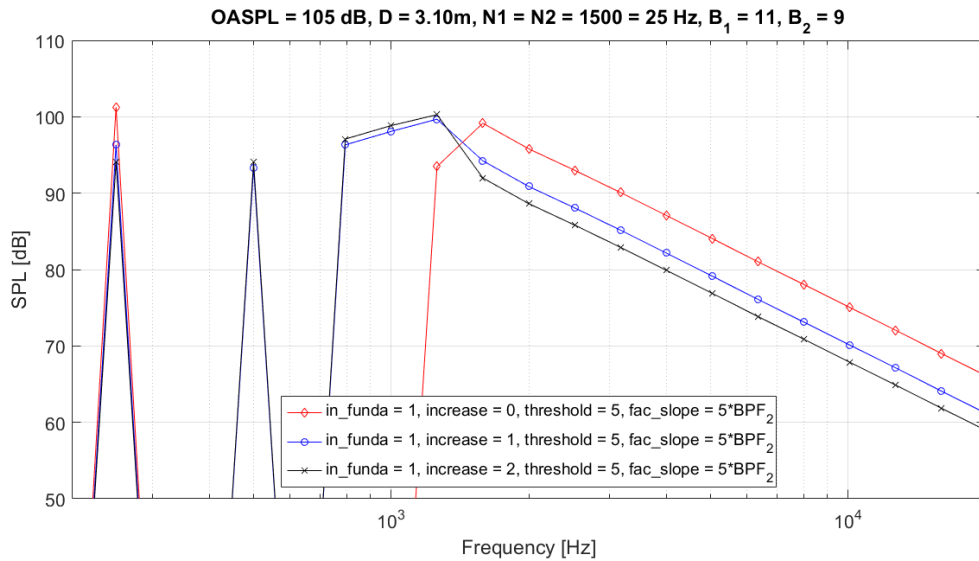


Figure 12.5: Effect of increase on 1/3-octave band frequency spectrum for $B_1 = B_2 + 2$ after [28]

The fourth parameter is *fac_slope*, which (in this analysis) is composed of a positive integer and BPF_2 . In order to obtain an instantaneous negative slope after the frequency depending on *threshold* (say ‘*threshold* frequency’), the integer in *fac_slope* needs to be equal or smaller compared to *threshold* (see first two graphs in figure 12.8). Otherwise, the *SPL* will grow past the ‘*threshold* frequency’ (see last graph of figure 12.8). The reason is readily explained: The addition value used in this function is computed by $(\frac{fac_slope}{f})^5$, with $fac_slope = 10 \cdot 200 = 2000$ Hz. Moreover, $threshold = 5$, which leads to $f = 1000$ Hz. Therefore, for all frequencies between 1000 Hz and 2000 Hz the solution is ≥ 1 . Concluding, only after $f = 2000$ Hz a negative slope is obtained.

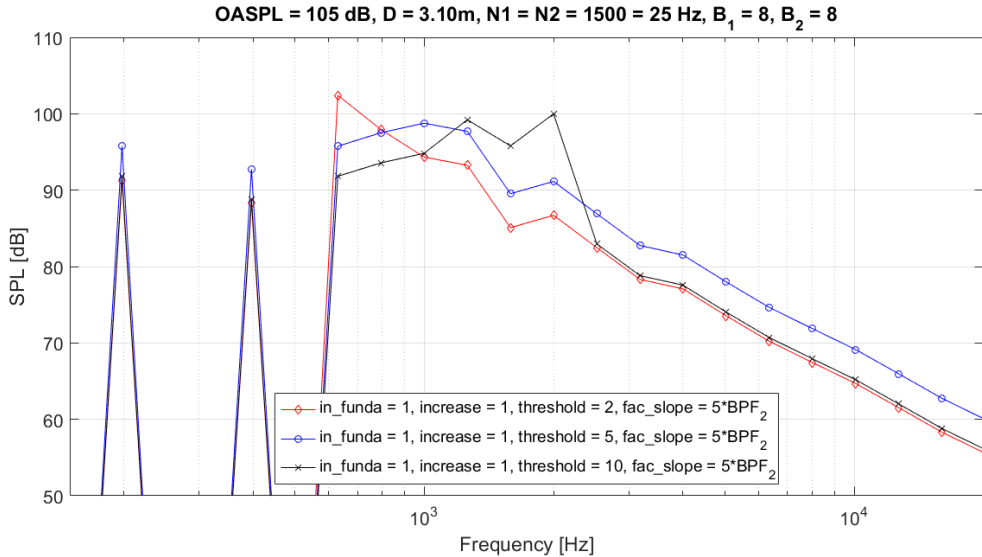


Figure 12.6: Effect of threshold on 1/3-octave band frequency spectrum for $B_1 = B_2$ after [28]

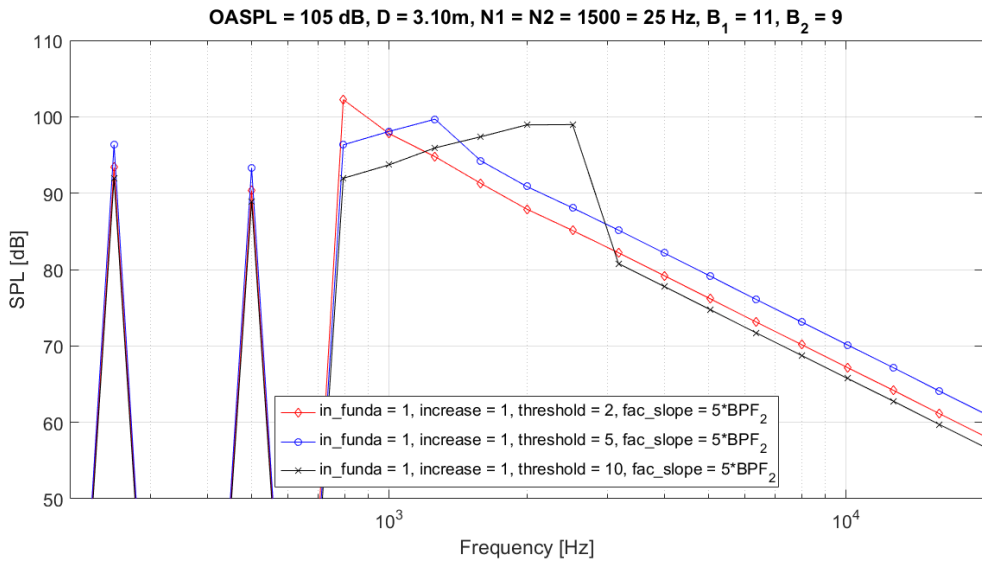


Figure 12.7: Effect of threshold on 1/3-octave band frequency spectrum for $B_1 = B_2 + 2$ after [28]

For an increased amount of blades, the ‘threshold frequency’ increases. Here it is, as previously mentioned, a frequency of 1375 Hz. Note: For this blade count $BPF_2 = 9.25\text{Hz} = 225\text{ Hz}$. Therefore, the adding value reduces from $(2000/1000)^5 = 32$ to $(2250/1375)^5 = 11.7$. Hence, the slope after ‘threshold frequency’ proceeds more gradually for figure 12.9 as compared to the emerged peak in figure 12.8.

Thus, if the *SPL* of higher frequencies is wished to be increased, *threshold* and *fac_slope* have to be increased (see figure 12.10). The fundamental, first harmonics and interaction tones are more pronounced, if *in_funda* and *increase* are raised, which is shown in figure 12.11.

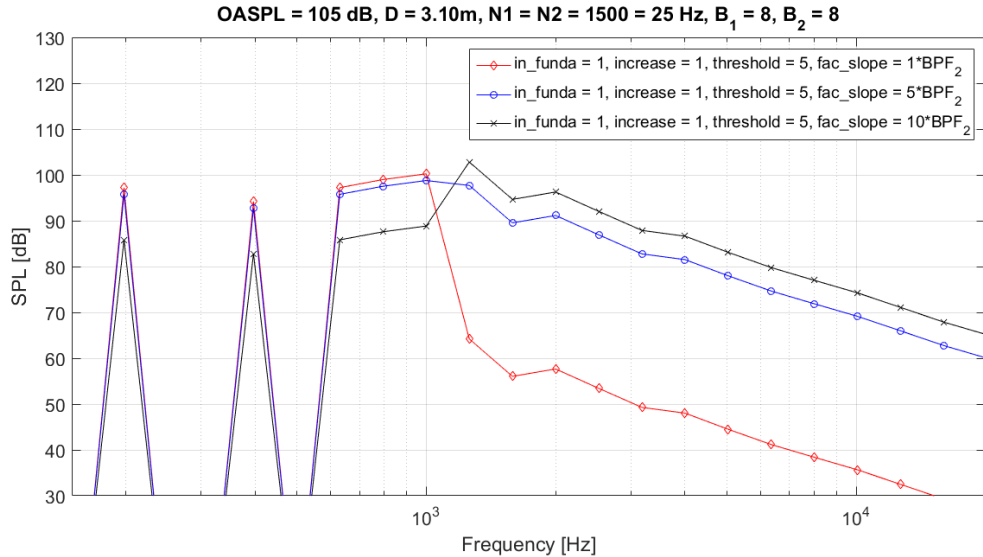


Figure 12.8: Effect of threshold on 1/3-octave band frequency spectrum for $B_1 = B_2$ after [28]

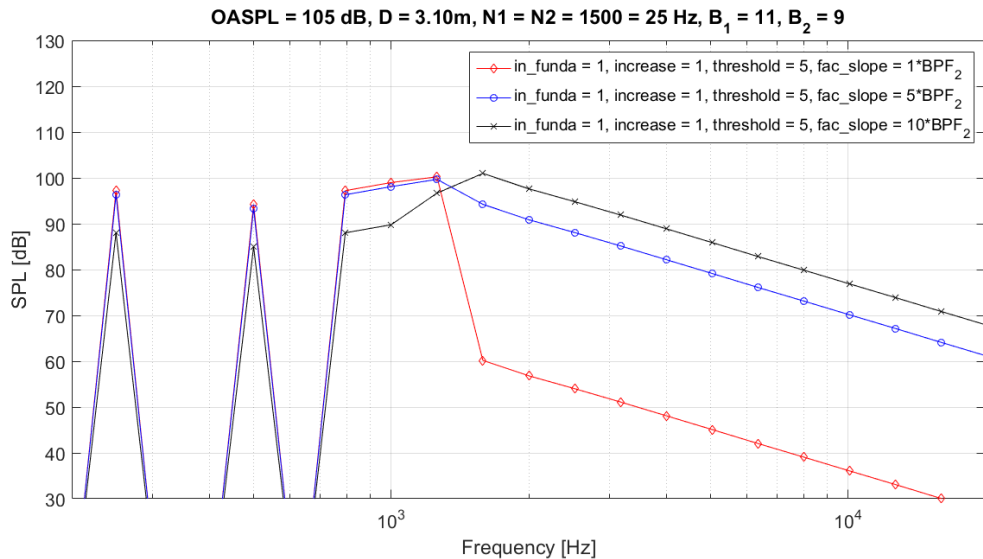


Figure 12.9: Effect of threshold on 1/3-octave band frequency spectrum for $B_1 = B_2 + 2$ after [28]

12.3 Tonal Noise

This section addresses the algorithm of function *PARTNERNarrowband.m*. It clarifies the in-/ output and illustrates the behaviour of results for different parameter settings.

All in- and outputs to *PARTNERNarrowband.m* are listed in table 12.3. Contrary to the analytical tool, *PARTNERNarrowband.m* only evaluates positive sound harmonics, therefore *m* contains only integers ≥ 0 , (see table 10.1 in section 10).

The theory to predict tonal noise was explained in section 6.1. Also, a table listing Mc-

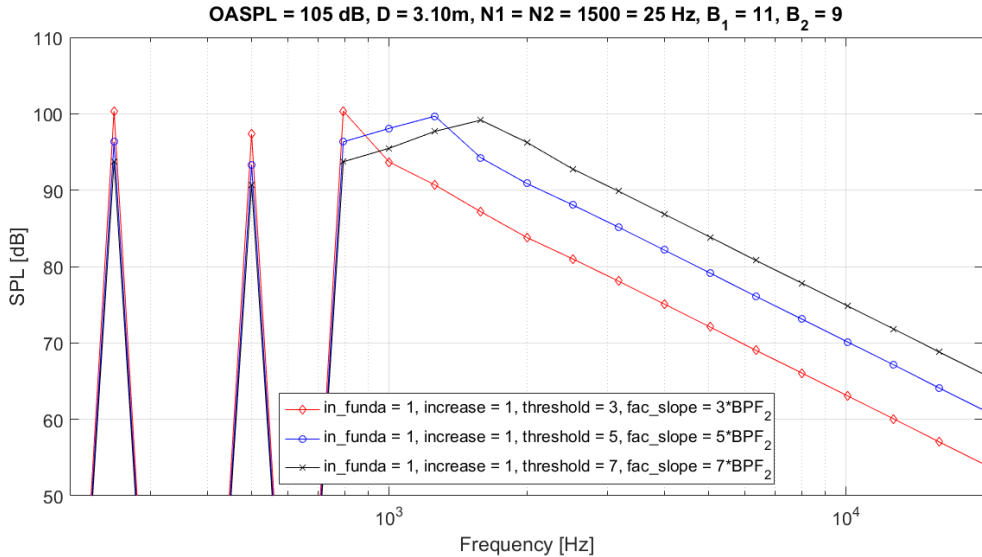


Figure 12.10: Increase SPL of higher tones for 1/3-octave band frequency spectrum for $B_1 = B_2 + 2$ after [28]

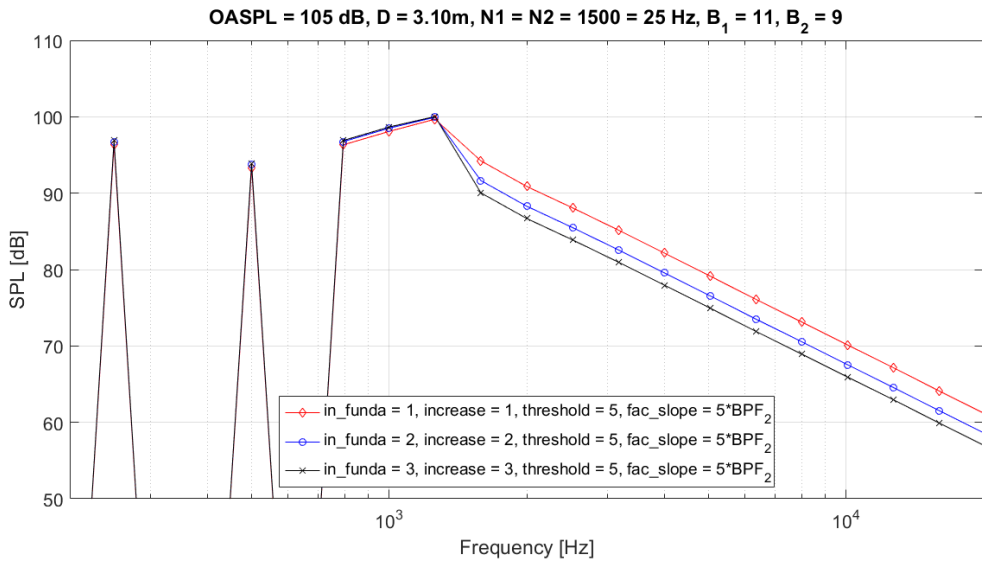


Figure 12.11: Increase SPL of fundamental tones for 1/3-octave band frequency spectrum for $B_1 = B_2 + 2$ after [28]

Curdy attenuation factors is presented. Table 6.1 and equation 6.1 lead to the fact that for higher tone numbers, the McCurdy's factor decreases (its negativity increases), so does its associated *SPL*. Consequently, equation 6.1 reveals a drop in *SPL* for an increase in *TS*. This behaviour is visualised by figures B.2 - B.13 in appendix B.

In general, parameter *init* is the initial value for broadband noise. Since the *SPL* of each tone is increased according to the *OASPL*-value from the input, *init* is always set to zero. If for any circumstance the computational algorithm is changed, *init* has to be investigated and, if necessary, adjusted.

Table 12.3: Input and output data of PARTNER tones function

PARTNERNarrowband.m			
Input		Output	
Type	Unit	Type	Unit
B_1	-	SPL	dB
B_2	-	f	Hz
Ω_1	Hz		
Ω_2	Hz		
$OASPL$	dB		
m	-		

12.4 Tonal-Directivity

This section explains the handling of function *directivity.m*. Again, in- and output variables are listed in table 12.4. In *directivity.m* the Bessel Function of First Kind is evaluated to approximate the tonal directivity.

Table 12.4: Input and output data of tonal directivity function

directivity.m			
Input		Output	
Type	Unit	Type	Unit
m	-	SPL	dB
θ	rad	n^*	-
B_1	-	f	Hz
BPF_1	Hz		
B_2	-		
BPF_2	Hz		
D_2	m		
c	m s^{-1}		
p_{e0}	Pa		

*Harmonic number for correction

Two normalised directivity plots are depicted in figures 12.12 and 12.13, for $B_1 = B_2 = 8$ and $B_1 = B_2 + 2 = 11$. Moreover, the inputs are given to be $D_2 = 3.05$ m, $c = 340 \text{ ms}^{-1}$ with a step size of two degrees for the observer angle, θ . Due to different blade count BPF differ: $BPF_1 = BPF_2 = 191.2$ Hz for the first and $BPF_1 = 262.9$ Hz plus $BPF_2 = 215.1$ Hz for the second CROR. For equal blade count, the directivity is identical for BPF_1 and BPF_2 . Therefore, the graphs in figure 12.12 coincide for fundamental and second harmonic. The interaction tones cover a wider range of observer angle. Thus at forward and aft angles,

noise is dominated by the interaction tones. In plane of rotation, the fundamental tones are predominant. This behaviour was also depicted in figure 5.3 of section 5.3.

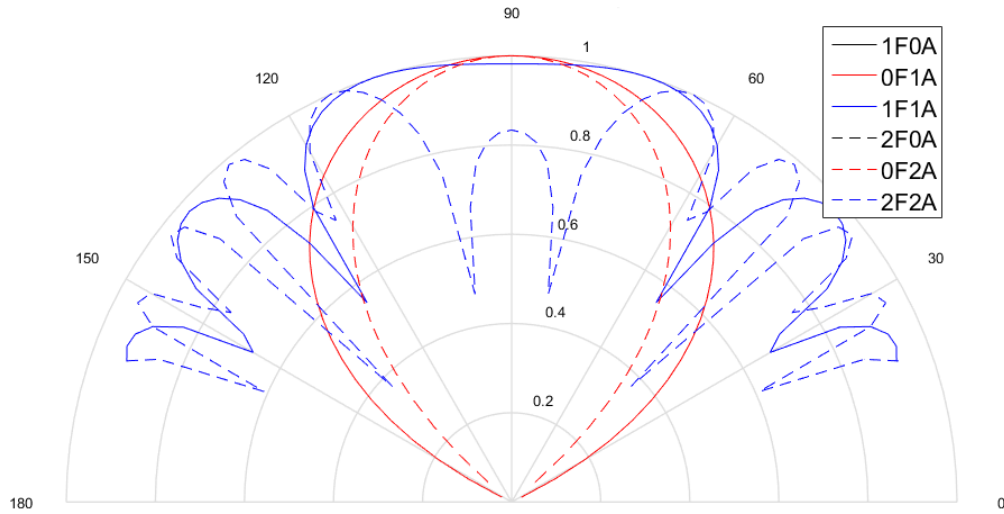


Figure 12.12: Tonal directivity for $B_1 = B_2$ after [28]

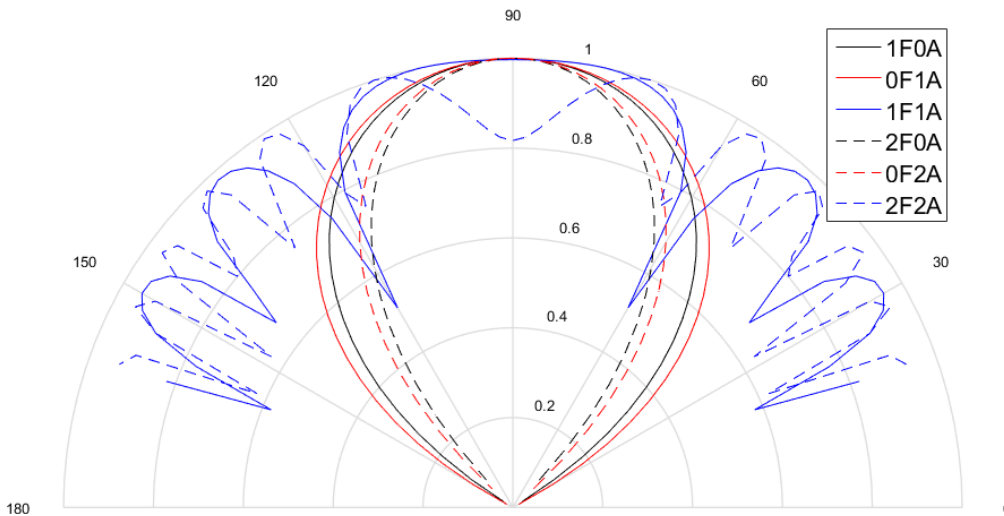


Figure 12.13: Tonal directivity for $B_1 = B_2 + 2$ after [28]

Analogous to that is the prediction for different blade counts. Again, fundamental and harmonic tones are depicted as a lobe mainly radiating in the rotational plane. Different frequencies are obtained due to variation in blade count, which results in similar but not identical lobes for the tone's directivity. Also for this blade setting and in accordance to literature, interaction tones show high sound pressure radiation forward and rearward.

13

Analytical Tool

This chapter presents the structure and main functions executed during evaluation of the analytical tool. Its flow chart is presented in figure 13.1. The chart is read in clockwise direction, thus *runXFOIL.m* is evaluated first, followed by *generateNAME.m* and *wavenumber_phi.m*, which all for their own return values to *main.m*.

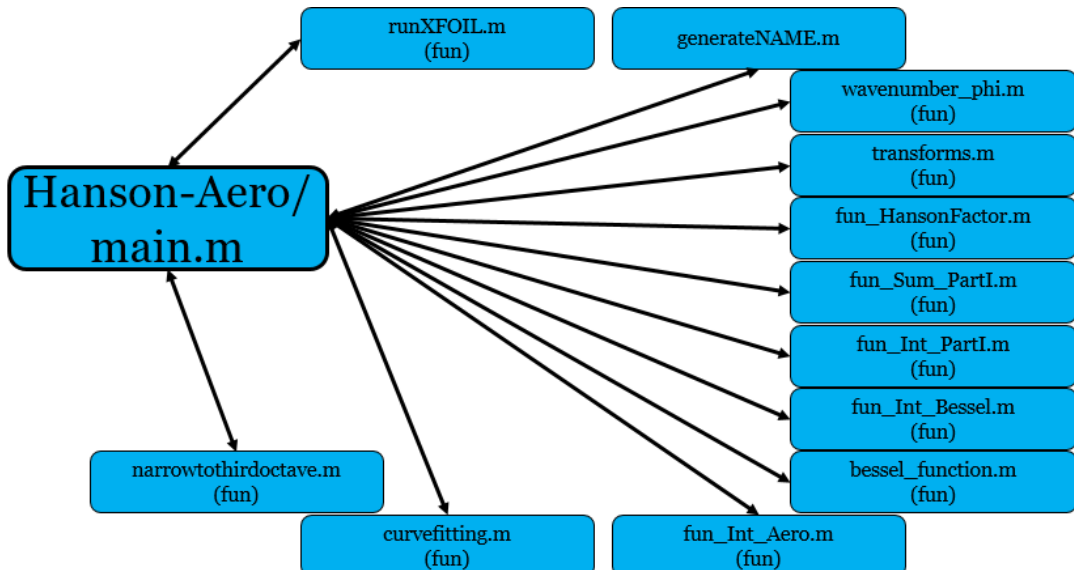


Figure 13.1: System structure of analytical tool

Firstly, this chapter will explain the XFOIL calculation in *runXFOIL.m*. Afterwards, it will introduce a feature to save computational time for recurrent calculation scenarios. Lastly, the implementation of Hanson's formulation is explained.

13.1 XFOIL Execution

Function *runXFOIL.m* calls and executes *xfoil.exe*. XFOIL computes for given angles of attack, both C_L and C_D values. Their results are used to compute lift and drag gradient, respectively. The gradients are thereafter used to compute the harmonic lift and drag coefficients, since the axial induction factor causes the angle of attack to change. The change in lift and drag due to the induced angle of attack is the harmonic lift and drag coefficient. All in- and output parameters to *runXFOIL.m* are listed in table 13.1.

Table 13.1: Input and output data of XFOIL execution function

<i>runXFOIL.m</i>			
Input		Output	
Type	Unit	Type	Unit
profile	-	message	-
Re_x	-	Alpha	$^\circ$
M_x	-	CL	
α_{fa_x}	$^\circ$	CD	-

13.2 Computational Database

The noise prediction program is a self-learning tool, that is, computed sound pressures for determined CROR settings are saved and in case of recurrent evaluation retrieved from a .m file. In order to store the data unambiguously, script *generateNAME.m* creates the file name, which consists of the tool's input values. The name is therefore a sequence of numbers and letters, all separated by minus. The final name's syntax is listed in table 13.2.

Table 13.2: Syntax of *generateNAME.m*

<i>generateNAME.m</i>												
T	-	P	-	R	-	γ	-	g	-	a_0	-	h
M_x	-	B_1	-	B_2	-	Ω_1	-	Ω_2	-	D_1	-	D_2
$D_{in,1}$	-	$D_{in,2}$	-	$cdr1$	-	$cdr2$	-	Blade Type	-	r_1	-	dt
$t(end)$	-	θ	-	$k(1)$	-	$k(end)$	-	$m(1)$	-	$m(end)$	-	$\text{length}(z_0)$

Table 13.2 is read from left to right and from top to bottom, with front rotor inner diameter, $D_{in,1}$, aft rotor inner diameter, $D_{in,2}$, chord to diameter ratio front rotor, $cdr1$, and chord to diameter ratio aft rotor, $cdr2$.

13.3 Hanson's Formulation

Hanson's formulation is divided into several minor functions. This guarantees a clear computational structure and a straight forward verification process. The function breakdown is listed in table 13.3. The results of each function is returned in a matrix of up to four dimensions. The dependence is also listed in table 13.3. The calculation is concluded with a joined evaluation of all matrices for their dependences, starting with z_0 . To integrate from root to tip a Riemann Sum is used which leads to a multiplication with dz_0 . Therefore, all z_0 dimensions are evaluated and it is continued with the summation over k and subsequently over m . Finally, only a two dimensional matrix remains with dependence θ and t .

Table 13.3: Input and output data of Hanson's formulation functions

Function	Evaluated Part of Hanson's Formula	Dependence
<i>fun_HansonFactor</i>	$\frac{-i \cdot \rho \cdot c^2 \cdot B_2 \cdot \sin(\theta)}{8 \cdot \pi \cdot \frac{r_1}{D_2} \cdot (1 - M_x \cdot \cos(\theta))}$	θ
<i>fun_Sum_PartI</i>	$e^{i((mB_2 - kB_1)(\phi - \phi^{(2)} - \frac{\pi}{2}) + (mB_2 \Omega_2 + kB_1 \Omega_1)(\frac{t}{c} - t))}$	θ, t, m, k
<i>fun_Int_PartI</i>	$M_r^2 e^{i(\phi_o + \phi_s)}$	θ, m, k, z_0
<i>fun_Int_Bessel</i>	$\frac{(mB_2 + kB_1 \Omega_{12}) z_0 M_T \sin \theta}{1 - M_x \cos \theta}$	θ, m, k, z_0
<i>fun_Int_Aero</i>	$\left(k_x \frac{C_{Dk}}{2} \psi_{Dk}(k_x) + k_y \frac{C_{Lk}}{2} \psi_{Lk}(k_x) \right)$	θ, m, k, z_0

For any observer angle, the pressure history can be plotted. Fourier analysis leads to the frequency spectrum. By applying the atmospheric attenuation a first frequency spectrum is determined. Lastly, the **curve fitting following the theory of PARTNER leads to the final frequency spectrum.**

14

Verification & Validation

This chapter reports the verification and validation process. It obeys the structure of part II. Firstly, the prediction based on Lewy's work is assessed. Secondly, the program's parts which are based on the content presented in PARTNER's report is examined. Lastly, the result obtained from Hanson's formulation is investigated.

Table 14.1: General input for verification and validation process

Sea Level Temperature	288.15 K
Sea Level Pressure	101325 Pa
Specific Heat Ratio	1.4
Specific Heat Difference	$287 \text{ Jkg}^{-1} \text{ K}^{-1}$
Gravitation	9.81 ms^{-2}
Temperature Laps Rate	-6.5 Kkm^{-1}
Humidity of Air	80 %
Flight Altitude	0 m
Fraction Blade 1 Root Chord over Diameter	0.11
Fraction Blade 2 Root Chord over Diameter	0.11
Blade Type	F7/A7
Airfoil	Symmetric

The validation data solely originates from open literature. The tool's validity for a wide range of operating settings and engine geometries is only revealed if a variety of datasets is covered. Therefore, data from various authors are compared to the prediction. Each dataset is investigated in correspondence to its specific input parameters. All common parameters are added to the list of general inputs, which is presented in table 14.1. These values are always valid if not mentioned otherwise.

The inner diameter can be computed from figure 158 in [22]. Since the outer diameter is given to be 3.05 m, this leads to a 1.49 m inner diameter, which is used if $D_2 = 3.05$ m.

14.1 Lewy

Based on [28], *OASPL*-directivity and third octave band frequency spectra are generated. In subsection 14.1.1, the data published in [22] are used for validation. To verify the correct implementation of Lewy's theory, a third octave band frequency spectrum is compared to Lewy's figure from [28].

14.1.1 OASPL-Directivity

Lewy describes the overall directivity as a parabola, with its maximum value for $\theta = 90^\circ$. As explained in chapter 5, the theory to predict *OASPL*-directivity was adapted to also match the magnitude. Figures 14.1, 14.2, and 14.3 compare the predicted *OASPL* with the measured data from [22]. All figures confirm the validity with an accuracy of approximately 5 dB.

Firstly, two performance settings of an engine geometry with eight propeller blades on each rotor are compared to their acoustic data (figures 14.1 and 14.2). Both predictions (in blue) show good agreement with data from F-7/A-7 blade geometries.

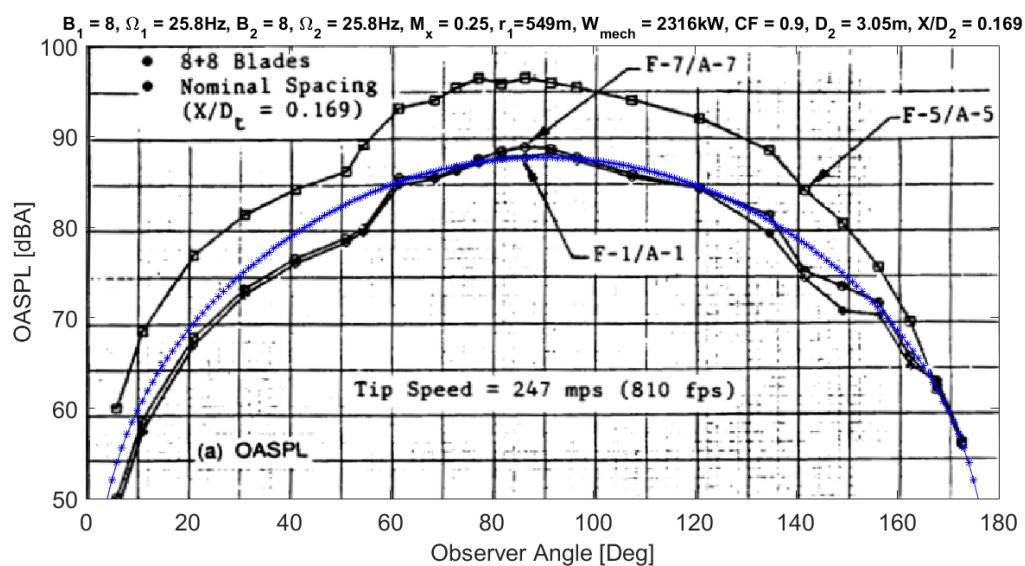


Figure 14.1: Results compared to figure 197 of [22]

Comparison conducted in both figures shows that the reduction in thrust and rotational speed leads to a decrease in SPL. In figure 14.1 the maximum value is found to be 88 dB, which is reduced to 82 dB in figure 14.2.

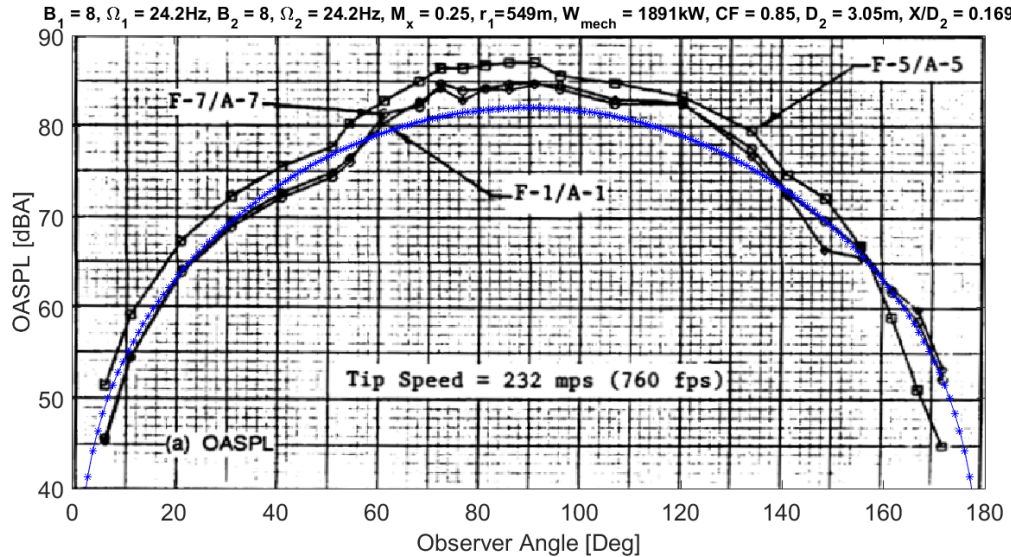


Figure 14.2: Results compared to figure 199 of [22]

Secondly, figure 14.3 depicts the OASPL-directivity for a CROR with blade settings $B_1 = 11$ and $B_2 = 9$. A maximum deviation of 5 dB is acceptable for a semi-empirical tool with low computation time.

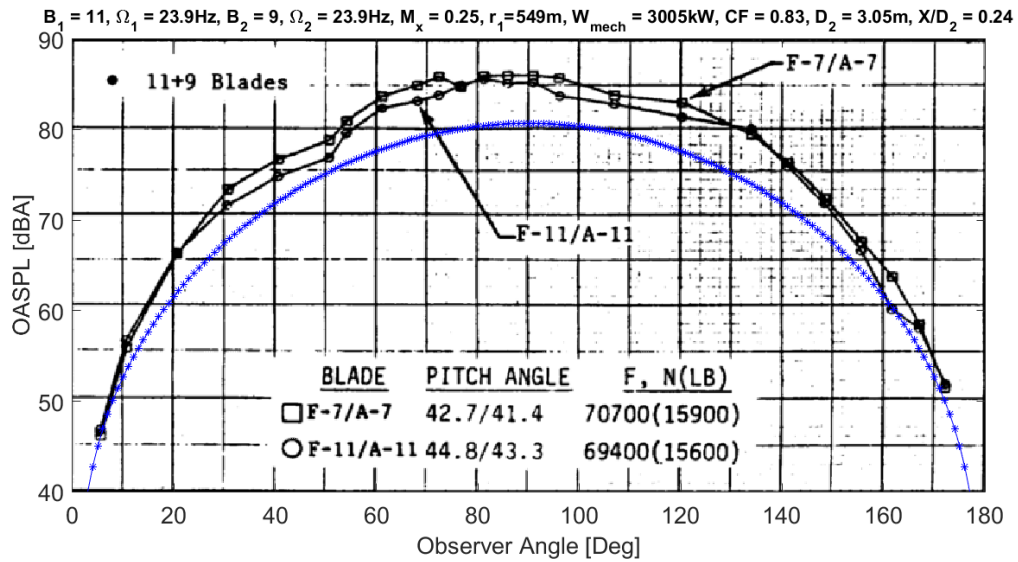


Figure 14.3: Results compared to figure 208 of [22]

14.1.2 Third Octave Frequency Spectrum

In the following subsection, model to model verification is executed. Lewy predicts the third octave band based on the theory explained in chapter 5. Figure 14.4 depicts the third octave band frequency spectra published in [28], while figure 14.5 presents the program's

output for equal inputs. It is evident that both figures show identical results.

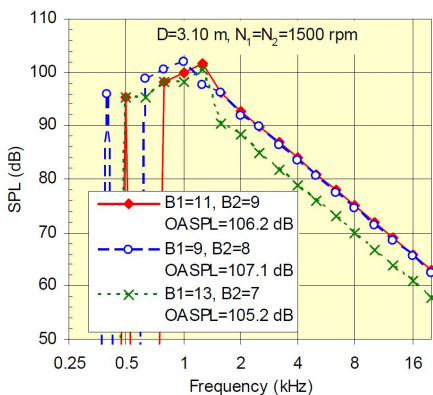


Figure 14.4: 1/3-Octave band results from [28]

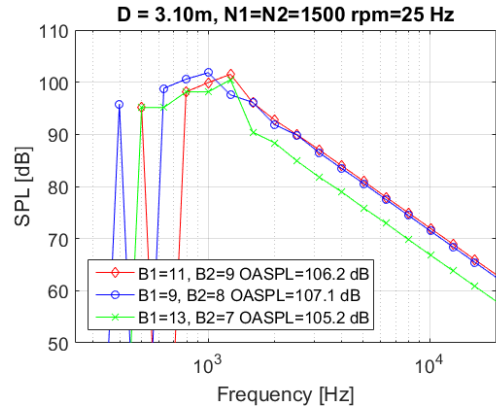


Figure 14.5: Exact reproduction with settings from table 5.2

In order to produce figure 14.5 for verification, the selected settings are `in_funda = 0`, `increase = 1`, `threshold = 5`, and `fac_slope = 5 · BPF2`.

14.1.3 Conclusion

The modified method to predict the *OASPL*-directivity returns good approximation of results, which are in agreement to data from [22]. The user has to account for a miss-prediction of approximately 5 dB, especially for reduced rotational speed. Thus, trustworthy values are predicted for take-off settings.

Lewy's method to estimate third octave frequency spectra was implemented successfully. Graphs from [28] were exactly reproduced. In order to increase the reliability of prediction results, an analysis of program setting values in dependence of CROR geometry and operating conditions is necessary. Differences in shape and magnitude of *SPL* are caused when using incorrect tool settings. The individual influence of the setting values is explained in chapter 12.

14.2 PARTNER

This chapter deals with the verification and validation of the implemented theory from PARTNER, which extends Lewy's model in order to gain more information about the acoustic emission of CROR. Firstly, the frequency spectrum generated in narrow- and third octave band are analysed. For the final result, the tonal components generated are also compared to measured data from [22]. The relevant figures are presented in subsection 14.2.1. Secondly, the tonal directivity of *BPF₁* and *BPF₂* is compared to measurements from [54],

presented in subsection 14.2.2. This section is concluded in subsection 14.2.3. The main statements about the tools reliability are formulated and the quality of results evaluated.

The setting values used in *PARTNERNarrowband.m* during verification and validation are $TS_f = 1.5$, $TS_a = 2$, $TS_s = 3$, and $init = 0$. However, if $B_1 = B_2$ only the lower value of TS_f and TS_a is of importance.

14.2.1 Frequency Spectrum

PARTNER bases its tonal prediction on the measured data published in [22]. Therefore, the computations should reproduce therein published plots. Since different outputs originate from PARTNER computations, each result needs to be compared with adequate data from [22]. The results published in [22] are depicted in the background of figure 14.6 and 14.7. Firstly, only the tonal plot resulting from combined calculations of Lewy and PARTNER are depicted in figure 14.6. The main tones are duplicated in their frequency value and closely match the *SPL*. The first tone is in good agreement with the data, while the second tone is over-predicted. Tones 3-6 show same overall tendency in *SPL*, however again a miss-prediction of approximately 5 dB is attained. The tendency of an increase in sound throughout tones 7-9 is evident, nevertheless the *SPL* value is miss predicted about 15 dB. The last compared tone accurately predicts the *SPL*.

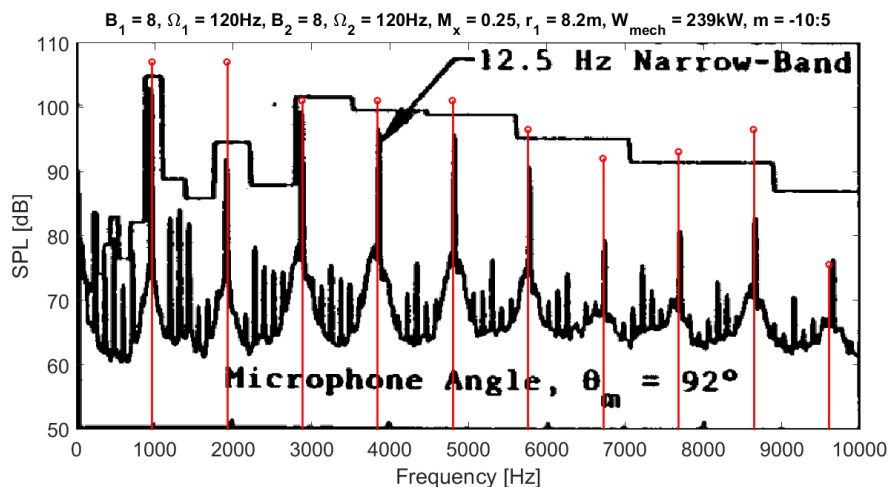


Figure 14.6: Tonal *SPL* compared to [22] with $D_2 = 0.622$ m, $\frac{X}{D_2} = 0.169$, and $CF = 0.83$ based on Lewy+PARTNER

Secondly, figure 14.7 shows the narrowband frequency spectrum generated based on Lewy and PARTNER. The tonal peaks from figure 14.6 resulting from the fundamentals, their harmonics, and interaction tones are preserved (red). Additional tones are generated using the approximating function, which is explained in chapter 6. For frequencies below

5000 Hz the spectrum is over predicted by up to 20 dB. For values higher than that, the sound is resembled fairly well.

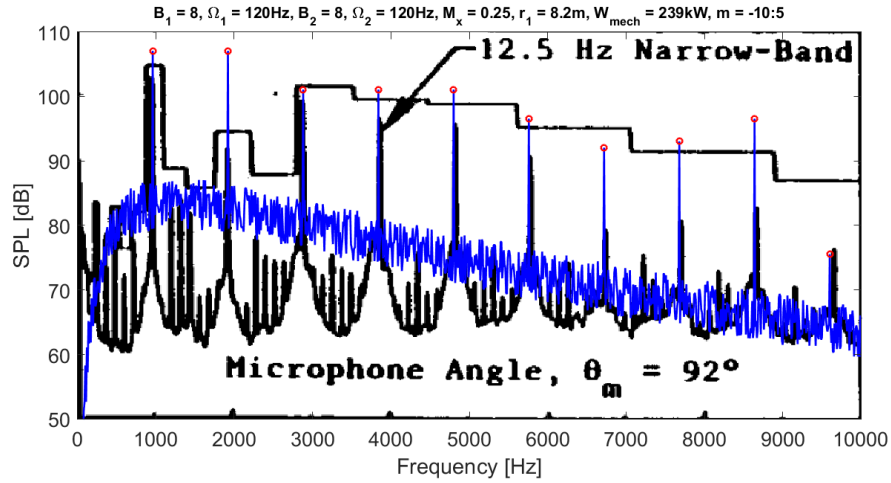


Figure 14.7: Narrowband compared to [22] with $D_2 = 0.622 \text{ m}$, $\frac{X}{D_2} = 0.169$, and $CF = 0.83$ based on Lewy+PARTNER

The decrease in SPL for frequencies below 1000 Hz is caused by the approximating function from PARTNER to obtain the correct third octave band spectrum. Therefore, this graph of [22] is contradicting to the third octave band based on data from for example figure B.1), which is listed in appendix B.

Figure 14.8 compares third octave band frequency spectra of the final prediction to data from Hoff [22]. The values for frequencies higher than 100 Hz are predicted in shape and level. The peaks of the bands containing the fundamental BPF are clearly present. Moreover, for all following harmonics and interaction tones the level and shape is resembled.

Nevertheless, if other observer angles and engine settings are considered, miss-match may occur. The following figures present the miss-predictions possible. Comparisons of observer angles 68° (figure 14.9) and 91° (14.10) shows that the first fundamental BPF is constant for the measured data of Hoff [22]. To the contrary, noise prediction shows a reduction in forward angle, analogous to the measurements of Woodward [54].

Nonetheless, the parabolic analogy applied to aft observer angles holds and predicts SPL with an accuracy of about 5 dB. It must be said, that for this CROR setting deviations to the measured data were found for all observer angles for frequencies higher than 2000 Hz.

Lastly, the frequency spectrum for CROR blade setting $B_1 = 11$ and $B_2 = 9$ is investigated. The fundamental tones are predicted in shape and level. Moreover, a ‘valley’ between the harmonics/interaction and fundamental tones is reproduced. Small deviations in SPL for frequencies below 2000 Hz are noticeable. SPL for higher frequencies are predicted unsatisfactorily.

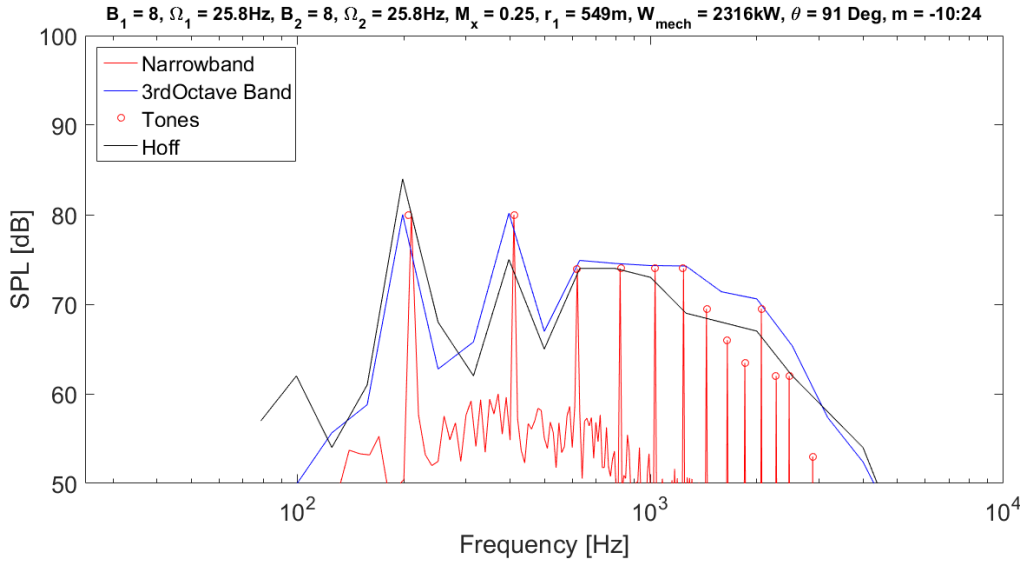


Figure 14.8: $B_1 = B_2$ prediction for 1/3-octave band at $\theta = 91^\circ$ compared to [22]

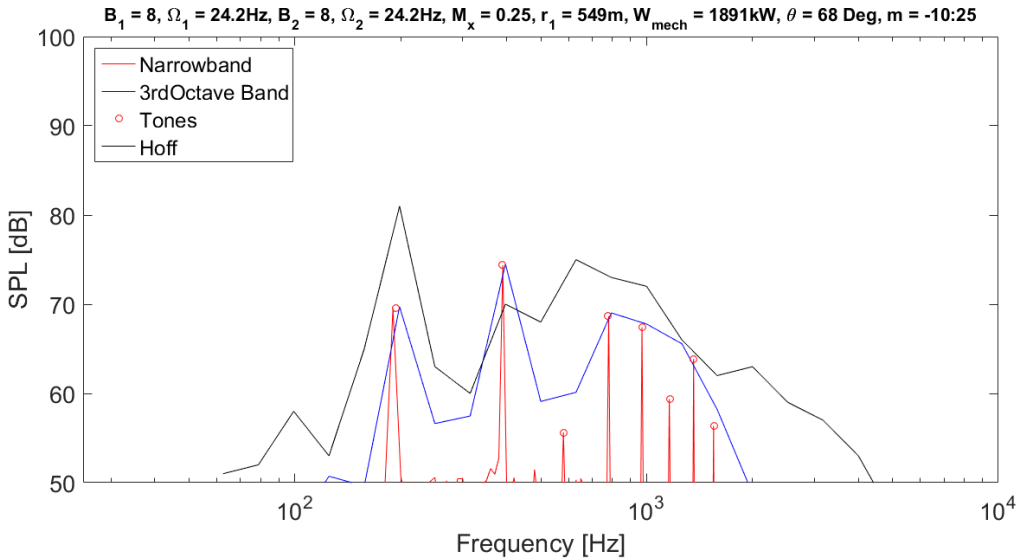


Figure 14.9: $B_1 = B_2$ prediction for 1/3-octave band at $\theta = 68^\circ$ compared to [22] reduced thrust

14.2.2 Tonal-Directivity

In this subsection, the prediction of SPL for BPF_1 and BPF_2 are evaluated using the directivity of tones published in [54]. In order to predict the tonal directivity, the Bessel Function of First Kind is applied. Figure 14.14 shows good agreement with Woodward's data. For BPF_1 miss-match of some 5 dB for observer angles of $50 - 100^\circ$ are evident. Perfectly resembled is the tonal directivity for BPF_2 . The data is well predicted for observer angles of $60 - 120^\circ$.

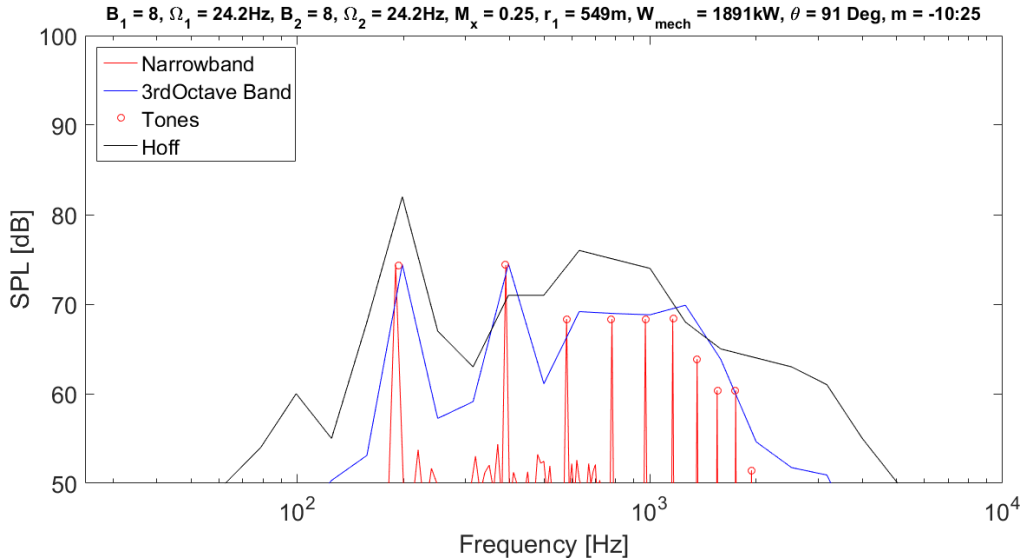


Figure 14.10: $B_1 = B_2$ prediction for 1/3-octave band at $\theta = 91^\circ$ compared to [22] reduced thrust

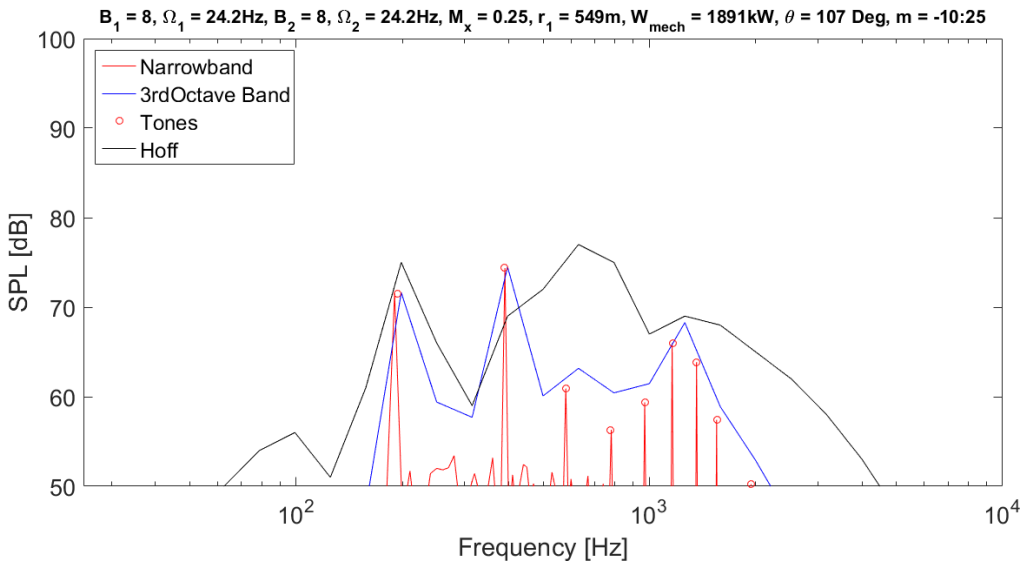


Figure 14.11: $B_1 = B_2$ prediction for 1/3-octave band at $\theta = 107^\circ$ compared to [22] reduced thrust

14.2.3 Conclusion

Figures 14.8, 14.10, 14.13, and 14.14 show that the method composed of Lewy and PARTNER provides good approximations for low computational time. Especially the noise prediction for BPF_1 is trustworthy, since a maximum miss-prediction of approximately 5 dB was shown. In general, the same is true for BPF_2 , it was shown that the directivity is predicted in shape and magnitude.

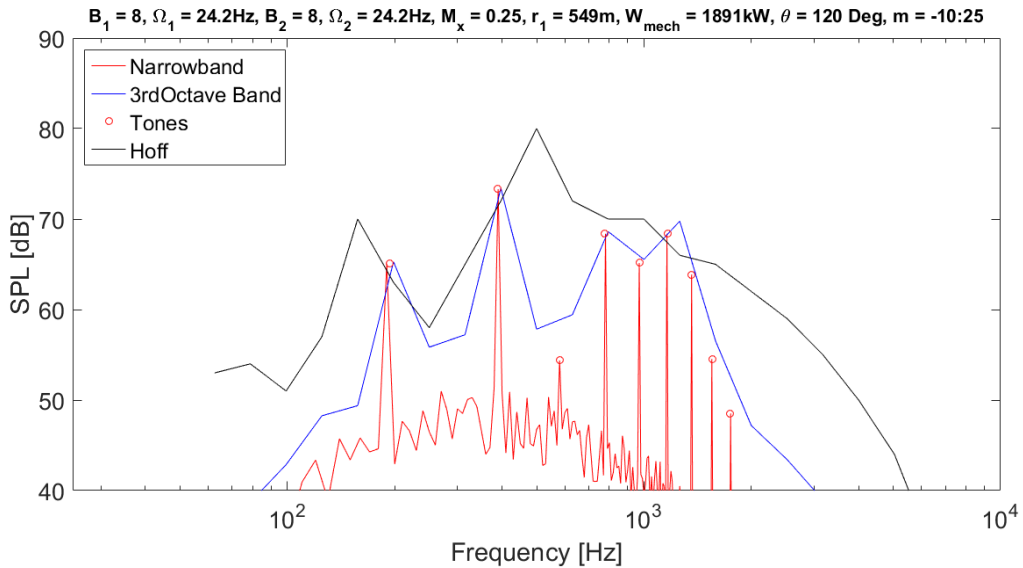


Figure 14.12: $B_1 = B_2$ prediction for 1/3-octave band at $\theta = 120^\circ$ compared to [22] reduced thrust

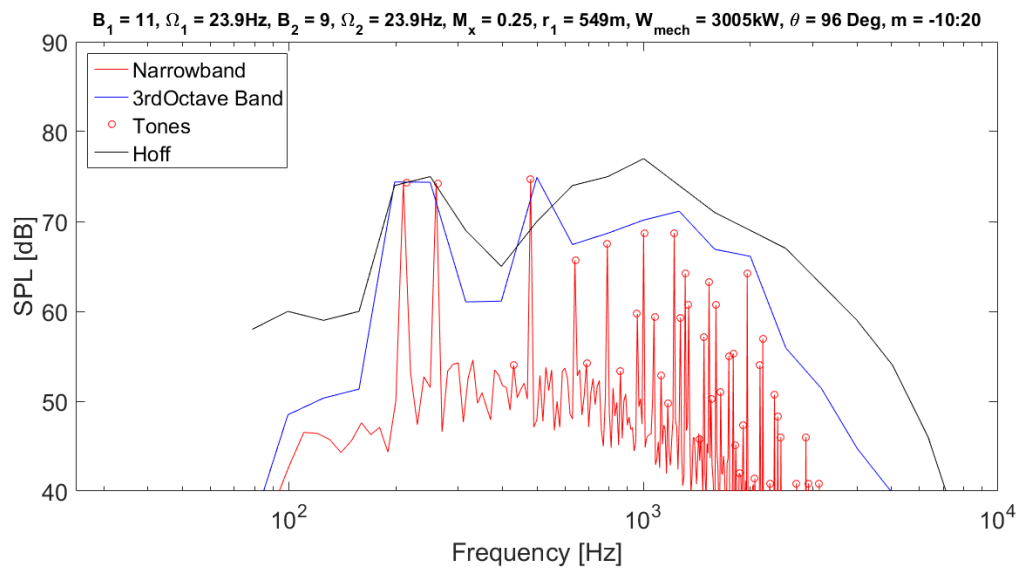


Figure 14.13: $B_1 = B_2 + 2$ prediction for 1/3-octave band at $\theta = 96^\circ$ compared to [22]

The method to predict narrowband spectra shows good predictions for observer angles close to the plane of rotation. Moreover, it returns good results for frequencies between 100 Hz and 2000 Hz. For frequencies higher than 2000 Hz and observer angles off plane of rotation, the prediction provides a good indication but are to be analysed with good understanding of the matter and in careful evaluation of result reliability.

This section showed, that the agreement of prediction and measurements also depends on the source of data. Woodward (figure 14.14) shows a decrease in SPL of approximately 5

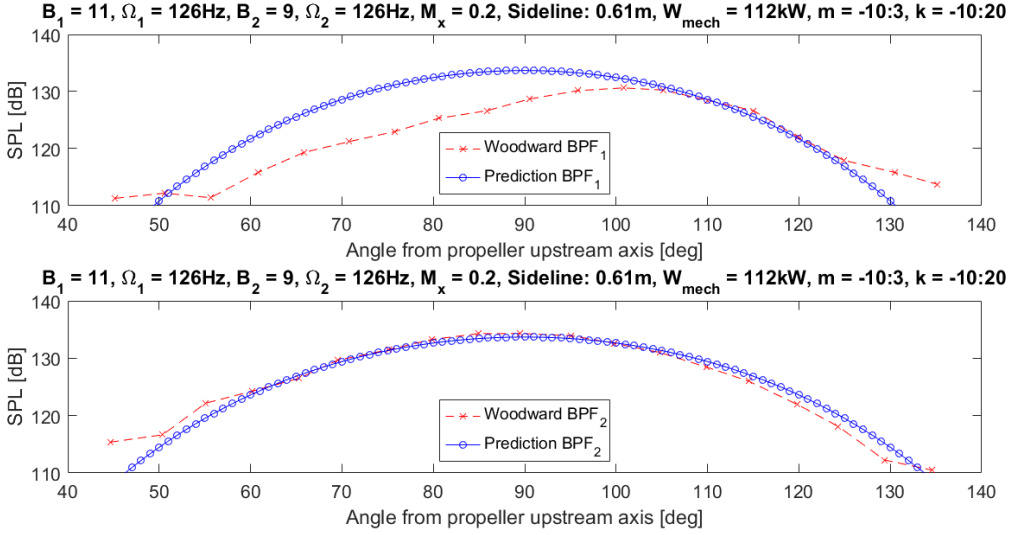


Figure 14.14: Predictions based on PARTNER method compared to [54] with $D_1 = 0.622\text{ m}$, $D_2 = 0.607\text{ m}$, $\frac{X}{D_2} = 0.14$, and $CF = 0.9$

dB between 70° and 90° for BPF_1 and BPF_2 . Contrary to that are the measurements plotted in third octave frequency spectra of Hoff. The SPL of the third octave band, that contains the fundamental tones (figures 14.9 and 14.10) is nearly constant.

Lastly, the input parameter can influence the predictions results. If settings that are not covered by input data influence the measurement data, the change will not be captured by the tool. Also, deviations can originate from the estimated thrust level adequately. Moreover, the approximated conversion from force to work introduces uncertainty.

14.3 Analytical Tool

This section classifies the noise predictions obtained from the analytical tool. Firstly, the $OASPL$ -directivity plots are compared to values from literature. Measured data from [22] and simulation results from [49] are referred to. Secondly, generated third octave frequency spectra are compared to data retrieved from [22]. The plots also show the computed narrowband graphs.

14.3.1 OASPL-Directivity

This subsection presents the quality of analytical prediction output. The results are compared with data from the 90's and model data from present. The formulation of Hanson's equation was published during the 80's, thus in proximity to the publication of reference data from [22]. The tool's functionality is verified with a comparison to Soulat's model from

[49], which is also based on Hanson's analytical theory.

At first, a CROR with blade count $B_1 = B_2 = 8$ and blade plan form F7 with high rotational speed is under investigation. In figure 14.15, the predicted values are reduced by 5 dB throughout the whole range of depicted observer angles. As a result, the OASPL matches the F-7/A-7 propeller blade for angles of $100^\circ - 135^\circ$. In general, the level is in proximity to the measured values. Nevertheless, the shape greatly miss-matches for observer angles of $45^\circ - 70^\circ$. The measurements show a parabolic shape, whilst the prediction presents a 'valley' around 65° . However, Soulats prediction in figure 14.16 confirms the reduction for angles around 70° .

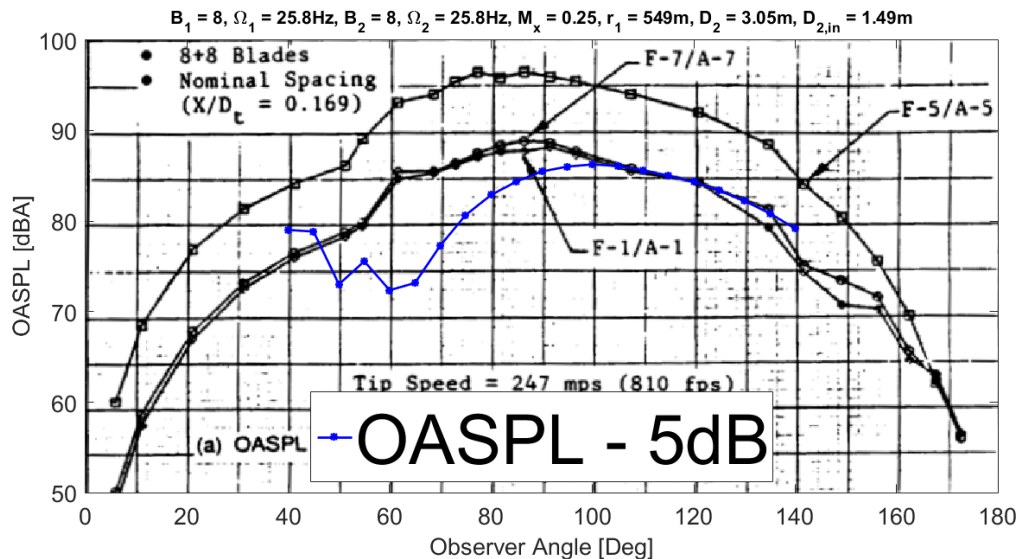


Figure 14.15: OASPL-directivity based on Hanson compared to figure 197 of [22] for 8+8 CROR

Again, the OASPL predicted with the analytical tool is corrected by 5 dB in figure 14.17. The shape presented is comparable to the one depicted in figure 14.15, with its minimum value at an observer angle of 60° . For angles $80^\circ - 140^\circ$ the shape is well predicted. Comparing the prediction to Soulat emphasises that the 'valley' is according to theory.

Lastly, a CROR with blade setting $B_1 = 11$ and $B_2 = 9$ is investigated. Same procedure as before is applied, leading to same results. For both figure 14.19 and 14.20, the same characteristics can be identified, which shows consistency in the prediction method.

14.3.2 Frequency Spectrum

This section compares the final frequency spectrum based on Hanson with data from [22]. The Hanson-based frequency spectrum is given in narrowband (8 Hz band width), while Hoff data is presented in third octave band. As such, the shapes can be compared and

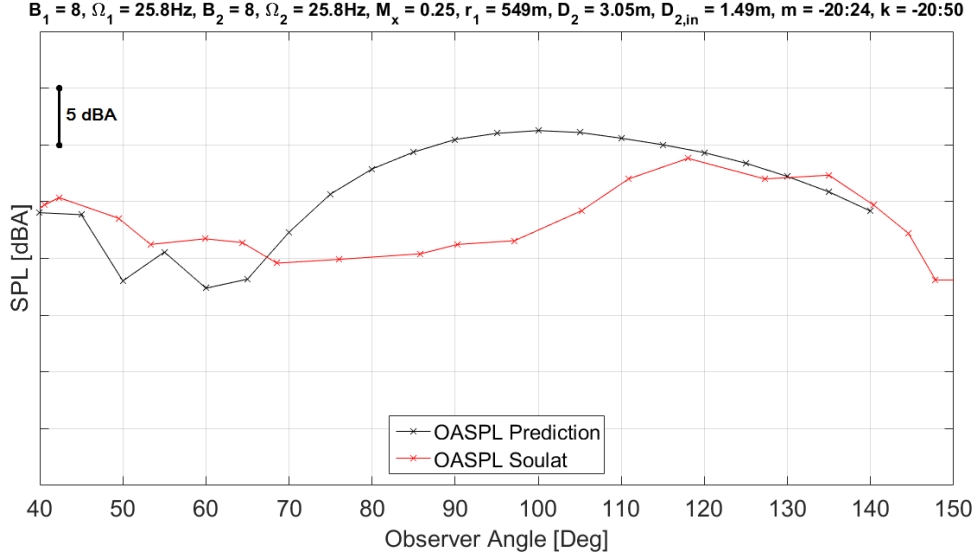


Figure 14.16: OASPL-directivity based on Hanson compared to Soulat [49] for 8+8 CROR

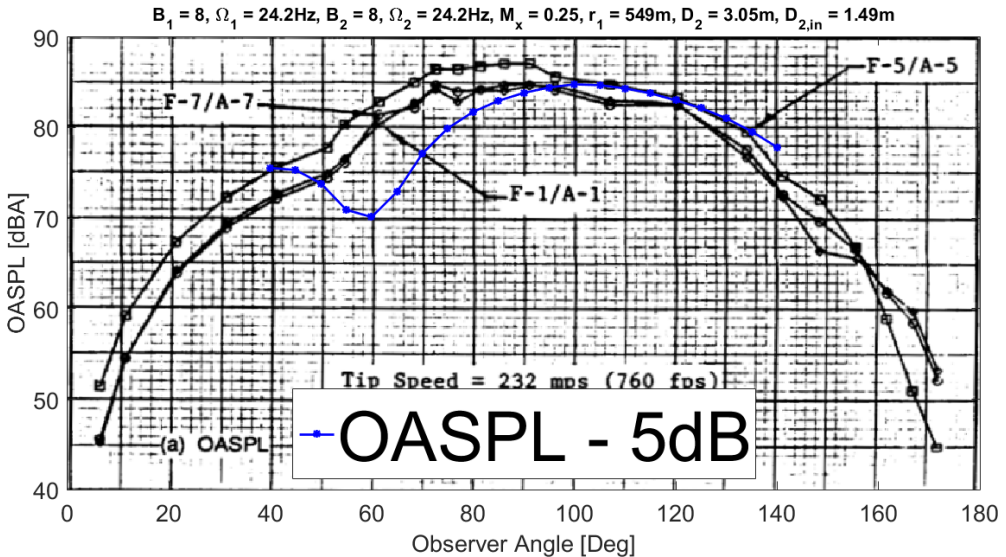


Figure 14.17: OASPL-directivity based on Hanson compared to figure 199 of [22] for 8+8 CROR

an idea of the correct *SPL* value can be obtained. The selected data is compared to the prediction in the same chronological order as it is in subsection 14.3.1.

Firstly, CROR with equal blade count and F7 blade is investigated. Figures 14.21 and 14.22 depict the predicted narrowband frequency spectra for 91° and 105°, respectively. The calculations are compared to spectra of 91° and 107°. At an observer angle of 91°, the general trend is reproduced by the prediction. After a peak for the first *BPF*, a reduction in *SPL* is obtained. Subsequently, for frequencies equalling first interaction tone and second harmonic, a growth in *SPL* is evident. After a newly decrease, the last *SPL* raise is measured. The prediction deviates from the data also because the last increase is over-predicted. In

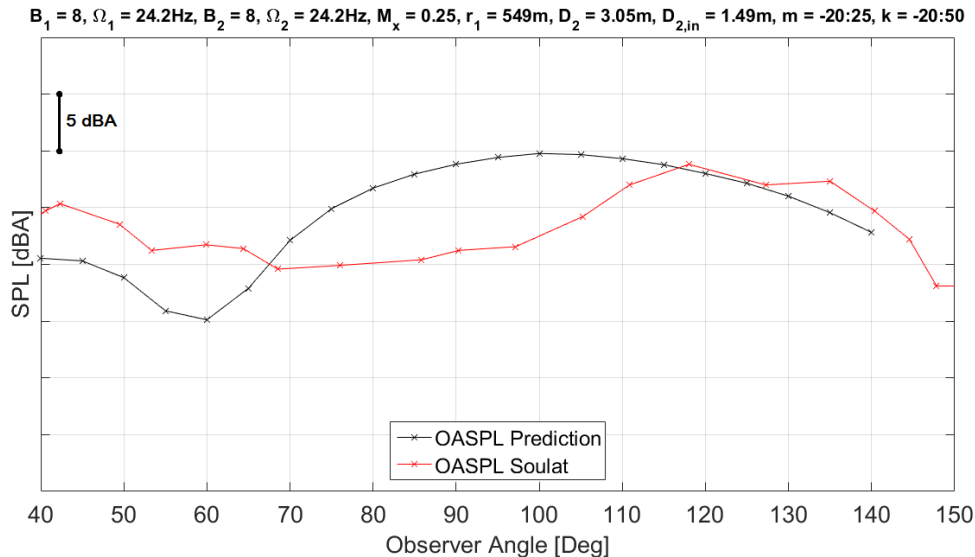


Figure 14.18: OASPL-directivity based on Hanson compared to Soulat [49] for 8+8 CROR

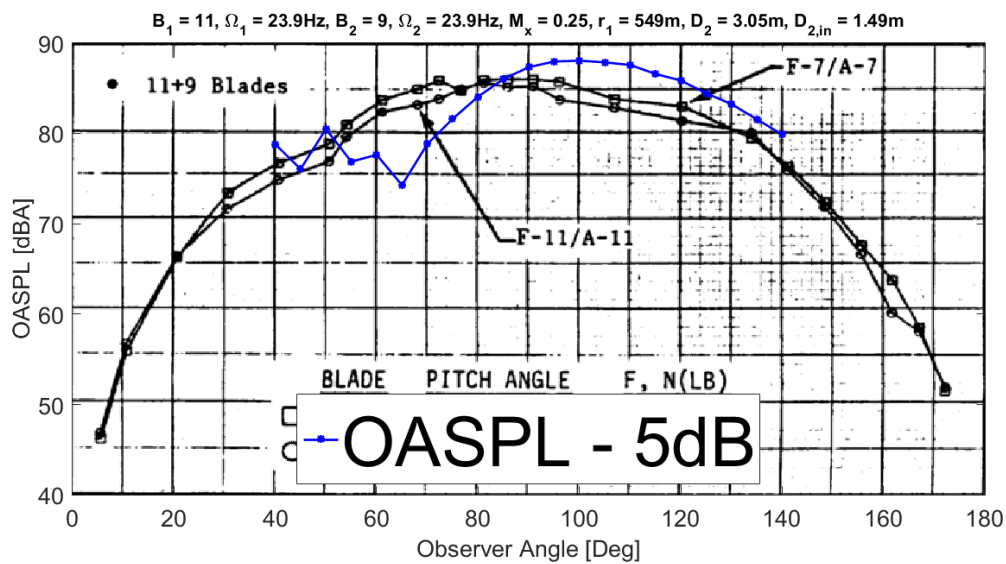


Figure 14.19: OASPL-directivity based on Hanson compared to figure 208 of [22]

general, the prediction reproduces the measurement trend to a frequency of about 1000 Hz.

If the same rotor is investigated for an observer angle of 105°, the same phenomenon is observed. Up until a frequency of about 1000 Hz the general tendency is well predicted, albeit over-predicted to a certain extend. Nevertheless, the sudden increase for frequencies higher 1000 Hz is captured again.

Furthermore, the eight bladed CROR is investigated with a reduced rotational speed. The predicted narrowband spectra for 90° and 105° are depicted in figures 14.23 and 14.24, respectively. Similarly, the comparison to third octave spectra of 91° and 107° is eval-

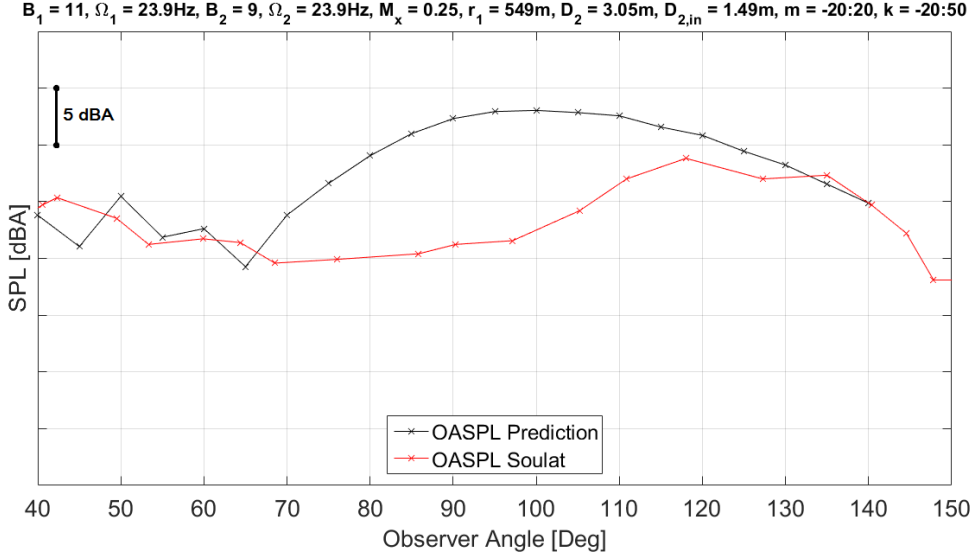


Figure 14.20: OASPL-directivity based on Hanson compared to Soulat [49]

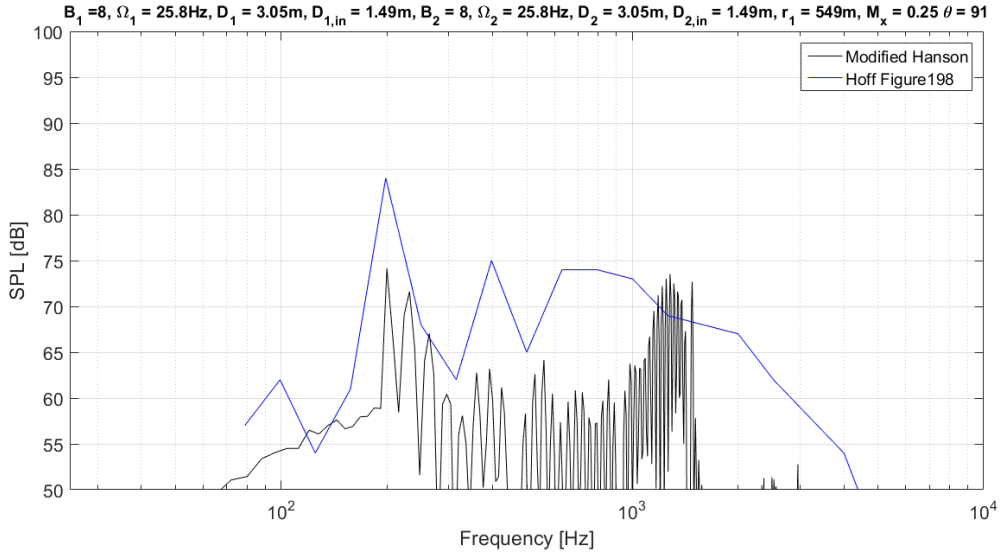


Figure 14.21: Frequency spectrum at $\theta = 91^\circ$ based on Hanson compared to figure 198 of [22] for 8+8 CROR

ated. For low frequencies, the predicted SPL shape is in good agreement to data. In accordance to the former prediction, but contradicting to the measurements, an increased SPL is shown at approximately 1500 Hz.

The increased SPL is also computed for the observer angle of 105°, for which the values are over-predicted throughout the complete spectrum.

Lastly, the spectra for a CROR with blade count $B_1 = 11, B_2 = 9$ are validated. In figure 14.25, the observer angles of 95° and 96° are compared. Again, the general shape is resembled, apart from the overall over-prediction. For frequencies in the vicinity of 1500 Hz, the SPL is strongly over-predicted, which is discovered in former investigation.

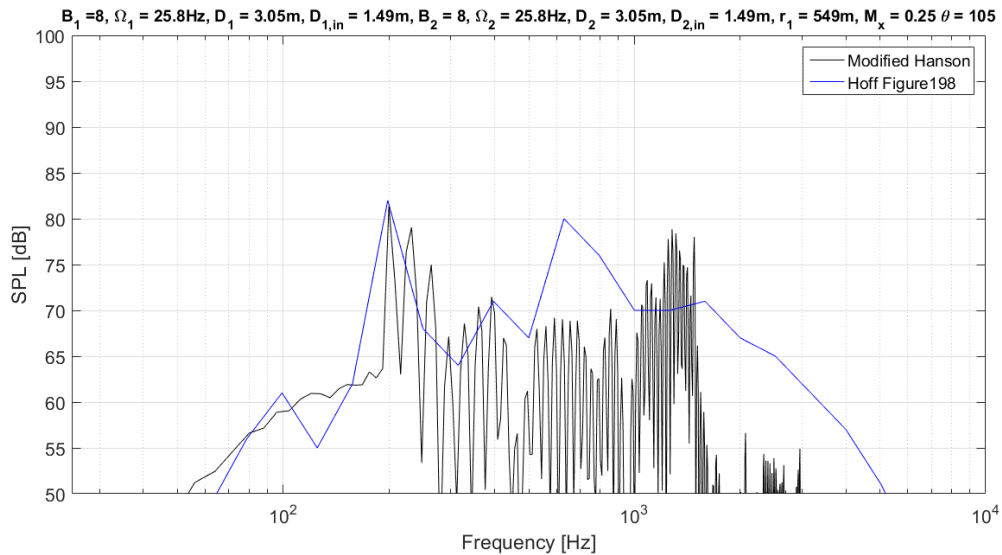


Figure 14.22: Frequency spectrum at $\theta = 105^\circ$ based on Hanson compared to figure 198 of [22] for 8+8 CROR

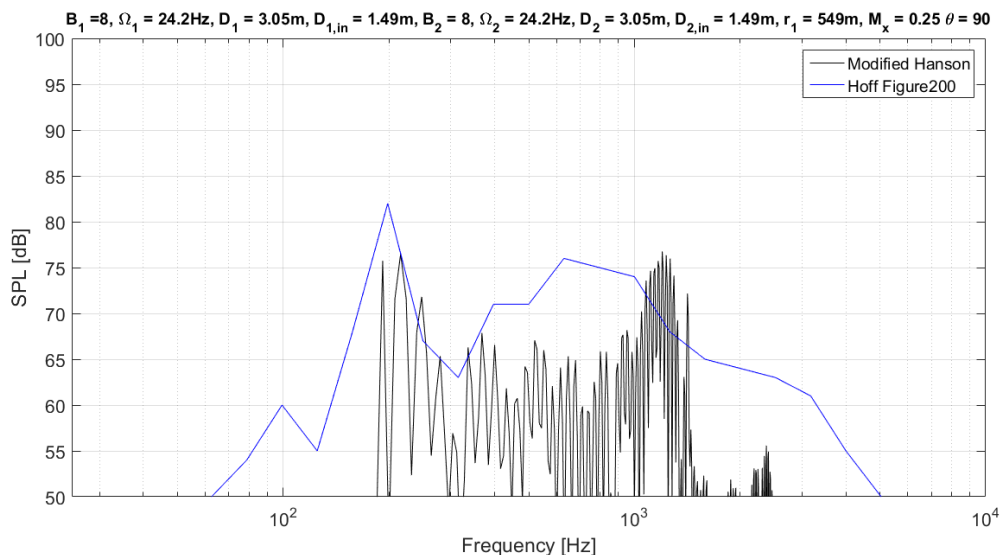


Figure 14.23: Frequency spectrum at $\theta = 90^\circ$ based on Hanson compared to figure 200 of [22] for 8+8 CROR

In the comparison of observer angles 105° and 107° , a constant over-prediction is evident. However, the general shape of the third octave band frequency spectrum is met.

14.3.3 Conclusion

The OASPL-directivity shows a repeating pattern for different rotor geometries and operating conditions. Therefore, it can be concluded that the theory was implemented correctly, hence unpredicted tool behaviour is excluded. The difference in shape between the pre-

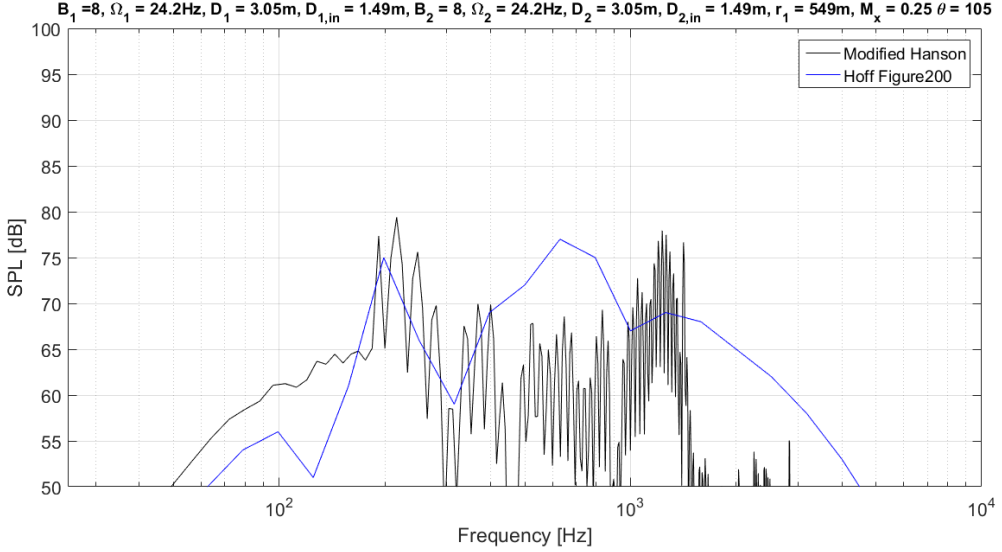


Figure 14.24: Frequency spectrum at $\theta = 105^\circ$ based on Hanson compared to figure 200 of [22] for 8+8 CROR

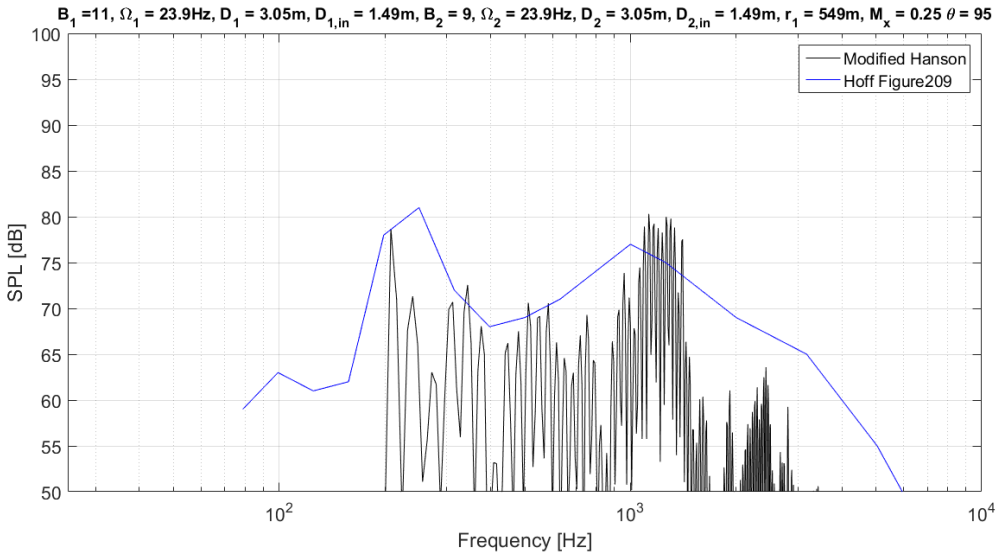


Figure 14.25: Frequency spectrum at $\theta = 95^\circ$ based on Hanson compared to figure 209 of [22] for 11+9 CROR

diction and the results of Soulat is caused by two factors. Firstly, it was not possible to exactly determine the necessary input Soulat used in his analysis. Secondly, the model presented in [49] was ‘originally developed by Hanson and extended to non compact chord length’ [49]. The advantage of implementing non compactness in chord wise direction is understood as follows: ‘A more detailed acoustic representation is to distribute the acoustic sources in the chord wise direction’ [45]. Moreover, ‘this requires that the unsteady aerodynamic solutions be fully three-dimensional and non compact when non compact solutions to the acoustic problem are employed’ [45]. Additionally, the input data to Soulat’s model

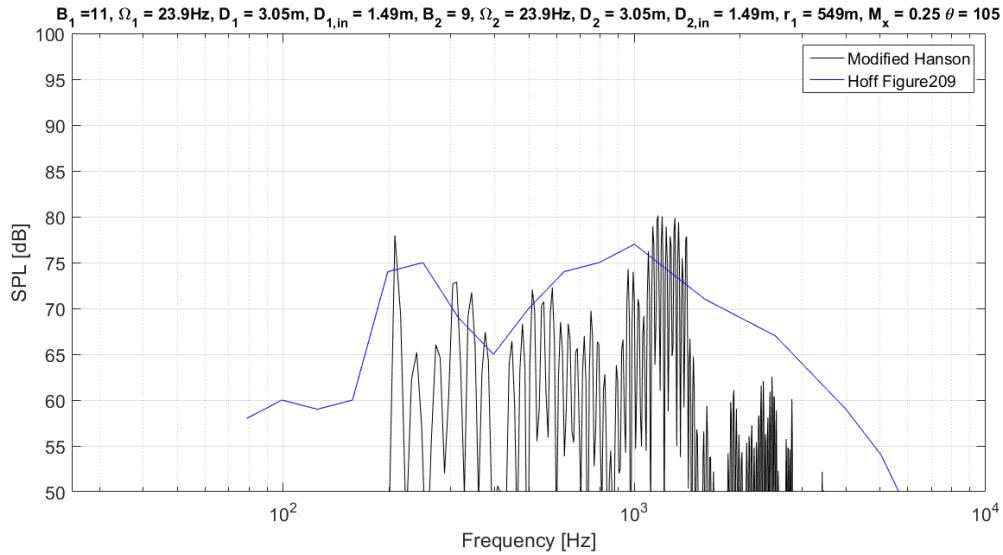


Figure 14.26: Frequency spectrum at $\theta = 105^\circ$ based on Hanson compared to figure 209 of [22] for 11+9 CROR

was not available in sufficient detail, thus a miss-match is acceptable.

The recurrent and consistent miss-prediction in the vicinity of 1500 Hz for all frequency spectra supports the statement mentioned above. Improved aerodynamic models will correct the computational results and predicted values.

IV

Concluding Remarks

15

Conclusion & Recommendation

This chapter concludes the work and evaluates the quality of result. Moreover, it illustrates possible improvements and additional analyses to be performed. In chapter 14, intermediate conclusions for each theory implemented were formulated. This chapter summarises the stated and further examines the tool's capabilities in light of future application.

Firstly, it was demonstrated that the semi-empirical tool returns good predictions of the noise level for *OASPL*-directivity for high rotational speeds, which favours the evaluation of take-off noise. The third octave band frequency spectrum model based on Lewy was implemented successfully. Further implementation of content from PARTNER project shows that good approximations are possible even for low computational time. The *SPL* and directivity of fundamental tones is trustworthy. For observer angles close to the plane of rotation the generated frequency spectra are well predicted, especially for frequencies between 100 Hz and 2000 Hz. For future work, an analysis of setting values is necessary to restrict the valid design space.

The analytical tool returns results in satisfying quality. However, potential for improvement is found in the blade aerodynamics approximation. In particular, the blade plan form replicated in JBlade should be improved or the non compact chord length, which means a fully three-dimensional blade pressure approximation, should be implemented. As such, recurrent and consistent miss-prediction in the vicinity of 1500 Hz for all frequency spectra could be removed.

It was discovered that the agreement of prediction and measurements also depends on source of data, i.e. experimental set-up and year of recording. Table 15.1 presents the pre-

dictability of results listed by tool methodology. The semi-empirical tool replicates 90's data well. However, the *OASPL*-directivity is assumed to be a parabola, while present models predict the highest *SPL* at observer angle in the range $110 - 140^\circ$. The analytical tool predicts the frequency spectra close to the plane of rotation in good accordance to 90's data. However, a maximum in *OASPL*-directivity plots is determined at observer angles between $100 - 120^\circ$, with a local decrease around 60° . On the other side, this is in agreement to presently developed prediction models.

Table 15.1: Overview of accordance with data in temporal perspective

Temporal Origin	Semi-Empirical	Analytical
Past	(✓)	(✓) in vicinity of plane of rotation
Present	(✓) for $80^\circ \leq \theta \geq 140^\circ$	(✓)

In order to improve the predictive quality of the semi-empirical tool, sensitivity analysis of the setting values of function *LewyThirdOctave.m* and *PARTNERNarrowband.m* can be executed. For different design spaces the parameters can then be adapted accordingly. Moreover, a better conversion algorithm from engine thrust to work can be incorporated. To improve the analytical tool a sensitivity analysis of parameters k , m , and $z_0_divisor$ in *Initiate.m* could be executed. There is also room for improvement in discretisation as well as the variability of blade geometries, as this would enhance the tool and allow the noise prediction for future use. This also includes the incorporation of higher fidelity aerodynamic models, which is only possible due to the tool's capabilities of evaluating any blade geometry desired. Such enhanced aerodynamic models lead to more realistic load distribution functions (because implementing non compactness leads to 3D aerodynamics) and hence a better approximation of CL_k and CD_k values. With the current tool, any new blade layout can be evaluated immediately, after its plan form and aerodynamic performance is incorporated into the tool database.

After integrating any upgrades to the tool, it is advised to perform a new verification and validation process.

Lastly, it is worth commenting on the usability of the tool. First of all, the tool will serve as upgrade to an overall engine noise prediction tool, whose flow chart is depicted in figure 4.1 of chapter 4. The integration is solely dependent on the generation of correct input files. A commented section in *Initiator.m* contains the syntax on how to overwrite values in .txt files automatically. At this development stage, the only users advised to employ the program are those who have a competent knowledge and know how to interpret and question the tool's results. Although it is possible to integrate this noise package into an in-design tool, the results should be examined with a critical attitude. Lastly, it is important to realise

that this tool evaluates the isolated conditions for zero angle of attack.

V

Bibliography

Bibliography

- [1] Asmar. Bessel's Equations and Bessel's functions. In *Partial Differential Equations with Fourier Series and Boundary Value Problems*, chapter 4, pages 237–248. Pearson, 2nd edition, 2004.
- [2] P. J. W. Block. Noise radiation patterns of counter-rotation and unsteadily loaded single-rotation propellers. *Journal of Aircraft*, 22(9):776–783, 1985. ISSN 0021-8669. doi: 10.2514/3.45201. URL <http://arc.aiaa.org/doi/abs/10.2514/3.45201>.
- [3] P. J. W. Block. Experimental Study of the Effects of the effects of installation on Single and Counter Rotation Propeller noise. Technical report, Langley Research Center, Hampton, 1986.
- [4] P. J. W. Block and G. L. Jr. Gentry. Directivity and Trends of Noise Generated by a Propeller in a Wake. Technical report, Langley Research Center, Hampton, 1986. URL <http://adsabs.harvard.edu/abs/1986dtng.rept.....B>.
- [5] P. J. W. Block, R. J. Klatte, and P. M. Druez. Counter-rotating propeller noise directivity and trends. *10th AIAA/CEAS Aeroacoustics Conference*, 1986. doi: 10.2514/6.1986-1929.
- [6] A. Deperrois. XFLR5, 2016. URL <http://www.xflr5.com/xflr5.htm>.
- [7] J. H. Dittmar. Cruise Noise of Counterrotation Propeller at Angle of Attack in Wind Tunnel. Technical report, Lewis Research Center, Cleveland, 1986.
- [8] J. H. Dittmar and R. J. Jeracki. Additional Noise Data on the SR-3 Propeller. Technical report, NASA Lewis Research Centre, Ohio, 1981.
- [9] J. H. Dittmar and D. B. Stang. Noise reduction for model counterrotation propeller at cruise by reducing aft-propeller diameter. Technical report, NASA Lewis Research Center, Cleveland, 1987. URL <http://hdl.handle.net/2060/19870009624>.
- [10] F. Farassat and C. P. Succi. Review of Propeller Discrete Frequency Noise Prediction Technology With Emphasis on Two Current Methods for Time Domain Calculations. *Journal of Sound and Vibration*, 71(3):399–419, 1980. ISSN 0022460X. doi: 10.1016/0022-460X(80)90422-8.

- [11] F. Farassat, S. L. Padula, and M. H. Dunn. Advanced turboprop noise prediction based on recent theoretical results. *Journal of Sound and Vibration*, 119:53–79, 1987. URL <http://www.sciencedirect.com/science/article/pii/0022460X87901891>.
- [12] A. Filippone and Z. Mohamed-Kassim. Multi-disciplinary simulation of propeller-turboprop aircraft flight. *Aeronautical Journal*, 116(1184):985–1014, 2012. ISSN 00019240.
- [13] FLUG REVUE. Snecma testet Open Rotor, 2013. URL <http://www.flugrevue.de/flugzeugbau/snecma-testet-open-rotor/518776>.
- [14] D. B. Hanson. Influence of Propeller Design Parameters on Far-Field Harmonic Noise in Forward Flight. *AIAA Journal*, 18(11):1313–1319, 1980. ISSN 0001-1452. doi: 10.2514/3.50887. URL <http://arc.aiaa.org/doi/abs/10.2514/3.50887>.
- [15] D. B. Hanson. Helicoidal Surface Theory for Harmonic Noise of Propellers in the Far Field. *AIAA Journal*, 18(10):1213–1220, 1980. ISSN 00011452.
- [16] D. B. Hanson. **Noise of Counter-rotation Propellers**. *Journal of Aircraft*, 22(7):609–617, 1985.
- [17] D. B. Hanson. Near-field frequency-domain theory for propeller noise. *AIAA Journal*, 23(4):499–504, 1985. ISSN 0001-1452. doi: 10.2514/3.8943. URL <http://arc.aiaa.org/doi/abs/10.2514/3.8943>.
- [18] D. B. Hanson. Acoustic Interference of Counter-Rotating Propellers. *Journal of Sound and Vibration*, 124(2):357–366, 1988.
- [19] D. B. Hanson. Unified Aeroacoustic Analysis for High Speed Turboprop Aerodynamics and Noise. Technical report, Nasa Lewis Research centre, 1991.
- [20] D. B. Hanson. Theory for Noise of Propellers in Angular Inflow With Parametric Studies and Experimental Verification. Technical report, NASA, 1993.
- [21] D. B. Hanson, C. J. McColgan, R. M. Ladden, and R. J. Klatte. Unified Aeroacoustics Analysis for High Speed Turboprop Aerodynamics and Noise Volume III - Application of Theory for Blade Loading, Wakes, Noise, and Wing Shielding. Technical report, Hamilton Standard Division, 1991.
- [22] G. E. Hoff. Experimental Performance and Acoustic Investigation of Modern, Counterrotating Blade Concepts. Technical report, NASA Lewis Research Center, 1990.
- [23] H. H. Hubbard. Sound From Dual-Rotating And Multiple Single-Rotating Propellers. Technical report, Langley Aeronautical Laboratory, 1948.

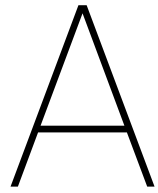
- [24] International Civil Aviation Organization. Annex 16 to the Convention on International Civil Aviation: Environmental Protection Volume I, 2008.
- [25] B. A. Janardan and P. R. Grieve. Acoustic characteristics of counterrotating fans from model scale tests. *Journal of Aircraft/12th Aeroacoustic Conference*, 27(3):268–275, 1989. ISSN 00218669. doi: 10.2514/6.1989-1142. URL <http://dx.doi.org/10.2514/6.1989-1142>.
- [26] M. J. Kingan. Open rotor broadband interaction noise. *Journal of Sound and Vibration*, 332(17):3956–3970, 2013. ISSN 10958568. doi: 10.1016/j.jsv.2013.03.014. URL <http://dx.doi.org/10.1016/j.jsv.2013.03.014>.
- [27] M. J. Kingan and R. H. Self. Advanced Open Rotor Noise Modelling Tool and Comparison Study Technical Dissemination Workshop. In *Omega - Aviation in a sustainable world*, number December, 2008.
- [28] S. Lewy. Semi-empirical prediction of tone noise due to counter-rotating open rotors. *Proceedings of the 20th International Congress on Acoustics, ICA 2010*, (August), 2010. URL [http://www.acoustics.asn.au/conference{_\]proceedings/ICA2010/cdrom-ICA2010/papers/p113.pdf](http://www.acoustics.asn.au/conference{_]proceedings/ICA2010/cdrom-ICA2010/papers/p113.pdf).
- [29] B. Magliozzi. Noise characteristics of model counter-rotating Prop-Fans. *11th Aeroacoustics Conference*, 1987. doi: 10.2514/6.1987-2656.
- [30] B. Magliozzi, P. Brown, and D. Parzych. Acoustic test and analysis of a counterrotating prop-fan model. Technical report, NASA Lewis Research Center, Cleveland, 1987.
- [31] R. M. Martin and F. Farassat. Users' Manual for a Computer Program To Calculate Discrete Frequency Noise of Conventional and Advanced Propellers. Technical report, Langley Research Center, Hampton, 1981.
- [32] D. Mavris, J. Tai, R. Young, and B. Havrilesko. Open Rotor Noise Impact on Airport Communities Open Rotor Noise Impact on Airport Communities. Technical Report July, FAA/NASA/Transport Canada, 2011.
- [33] D. A. McCurdy. Annoyance Caused by Advanced Turboprop Aircraft Flyover Noise - CR Propeller Configuration, Counter-Rotating Propeller Configuration. Technical report, Langley Resreach Center, Hampton, 1990.
- [34] G.A. Mitchell and D. C. Mikkelsen. Summary and Recent Results From the NASA Advanced High-Speed Propeller Research Program. In *AIAA/SAE/ASME 18th Joint Propulsion Conference*, 1982. doi: doi:10.2514/6.1982-1119.

- [35] J. Morgado. JBLADE: a Propeller Design and Analysis Software, 2014. URL <https://sites.google.com/site/joaomorgado23/Home>.
- [36] D. Nark, C. Burley, A. Tinetti, and J. Rawls. Initial Integration of Noise Prediction Tools for Acoustic Scattering Effects. *14th AIAA/CEAS Aeroacoustics Conference (29th AIAA Aeroacoustics Conference)*, (May):1–17, 2008. doi: 10.2514/6.2008-2996. URL <http://arc.aiaa.org/doi/abs/10.2514/6.2008-2996>.
- [37] T. Node-Langlois, F. Wlassow, V. Languille, Y. Colin, B. Caruelle, J. Gill, X. Chen, X. Zhang, and A. B. Parry. Prediction of Contra-Rotating Open Rotor broadband noise in isolated and installed configurations. *20th AIAA/CEAS Aeroacoustics Conference*, (June):1–15, 2014. doi: 10.2514/6.2014-2610.
- [38] A. B. Parry. *Theoretical prediction of counter-rotating propeller noise*. PhD thesis, University of Leeds, 1988. URL <http://etheses.whiterose.ac.uk/id/eprint/319>.
- [39] A. B. Parry, M. J. Kingan, and B. J. Tester. Relative importance of open rotor tone and broadband noise sources. *17th AIAA/CEAS Aeroacoustics Conference (32nd AIAA Aeroacoustics Conference)*, (June):5–8, 2011. doi: 10.2514/6.2011-2763. URL <http://eprints.soton.ac.uk/192027/> <http://dx.doi.org/10.2514/6.2011-2763>.
- [40] A. G. Rao. Lecture Notes AE-2203 Propulsion and Power, 2013.
- [41] J. P. Roberts and L. L. Beranek. Experiments in external noise reduction of a small pusher-type amphibian airplane. Technical report, NACA, Washington, 1952.
- [42] Rolls-Royce. Open rotor technology, 2016. URL <http://www.rolls-royce.com/about/our-technology/research/research-programmes/sustainable-and-green-engine-sage-itd/open-rotor-technology.aspx>.
- [43] G.J.J. Ruijgrok. *Elements of Aviation Acoustics*. Delft University Press, 1993. ISBN 90-6275-899-1.
- [44] M. K. Rwigema. Propeller Blade Element Momentum Theory with Vortex Wake Deflection. *Proceedings of the 27th Congress of the Aeronautical Sciences*, pages 1–9, 2010. URL <http://www.ewp.rpi.edu/hartford/{~}ernesto/S2013/MMEES/Papers/ENERGY/6AlternativeEnergy/McCosker/Rwigema2010.pdf>.
- [45] S. N. Koushik. *A new experimental approach to study helicopter BVI noise*. PhD thesis, University of Maryland, 2007.

- [46] A. Sahai. *Consideration of Aircraft Noise Annoyance during Conceptual Aircraft Design*. PhD thesis, RWTH Aachen, 2016.
- [47] M. A. R. Silvestre, J. Morgado, and J. C. Pascoa. JBLADE: a Propeller Design and Analysis Code. *2013 International Powered Lift Conference*, (August):1–12, 2013. doi: 10.2514/6.2013-4220. URL <http://arc.aiaa.org/doi/abs/10.2514/6.2013-4220>.
- [48] A. M. O. Smith. High-Lift Aerodynamics. *Journal of Aircraft*, 12(6):501–530, 1975.
- [49] L. Soulat, I. Kernemp, M. Sanjose, S. Moreau, and R. Fernando. Assessment and comparison of tonal noise models for Counter-Rotating Open Rotors. *19th AIAA/CEAS Aeroacoustics Conference*, pages 1–15, 2013. doi: 10.2514/6.2013-2201. URL <http://arc.aiaa.org/doi/abs/10.2514/6.2013-2201>.
- [50] L. Vion, G. Delattre, L. Jacquin, B. Rodriguez, R. Boisard, B. Ortun, and F. Falissard. Blade Patent.pdf, 2013. URL <http://google.com/patents/WO2013045859A1?cl=zh-CN>.
- [51] C. E. Whitfield, P. R. Gliebe, R. Mani, and P. Mungur. High Speed Turboprop Aeroacoustic Study (Single Rotation) Volume I: Model Development. Technical report, NASA Lewis Research Center, Cincinnati, 1989.
- [52] C. E. Whitfield, R. Mani, and P. R. Gliebe. High Speed Turboprop Aeroacoustic Study (Counterrotation) Volume I - Model Development. Technical report, NASA Lewis Research Center, 1990.
- [53] C. E. Whitfield, R. Mani, and P. R. Gliebe. High Speed Turboprop Aeroacoustic Study (Counterrotation) Volume II - Computer Programs. Technical report, NASA Lewis Research Center, 1990.
- [54] R. P. Woodward. Noise of a model high speed counterrotation propeller at simulated takeoff/approach conditions (F7/A7). *11th Aeroacoustics Conference*, 1987. ISSN 04999320. doi: 10.2514/6.1987-2657.

VI

Appendix



Final Result Display

This appendix lists examples of final figures, if its according handle is equal one. First, the figure output of semi-empirical tool is presented, followed by the display of analytical tool.

A.1 Semi-Empirical Tool

The displays are generated for an input of observer angle $\theta = 20 : 2 : 160$.

First, *OASPL*-directivity is plotted for observer angle from 0 to π . The example is given in figure A.1.

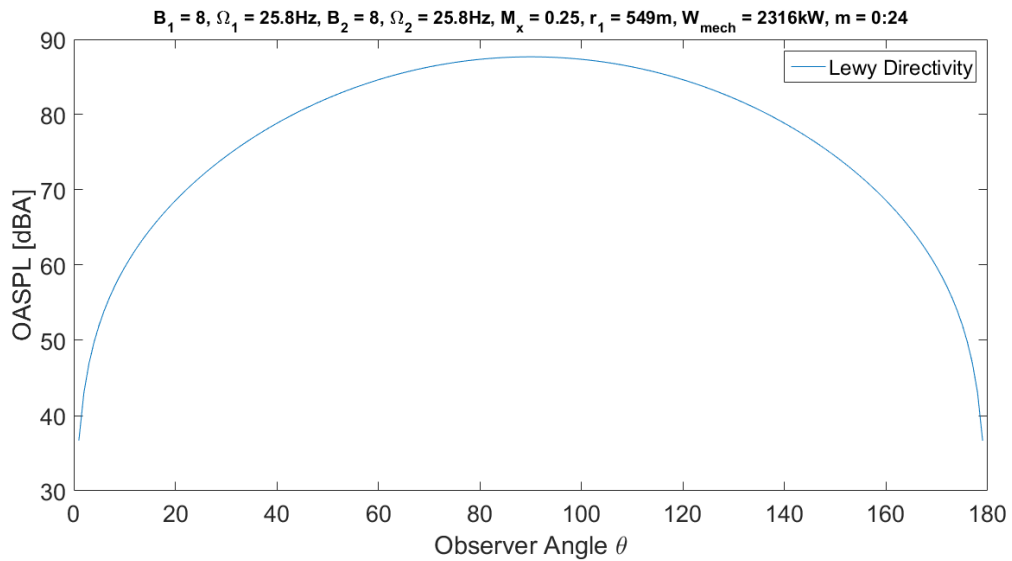


Figure A.1: Display if `plot_LowyDirectivity = 1` in `Initiate.m`

Next, the third octave band frequency spectrum based on Lewy is generated. However, this is only generated for observer angle of 90°. Figure A.2 is an example.

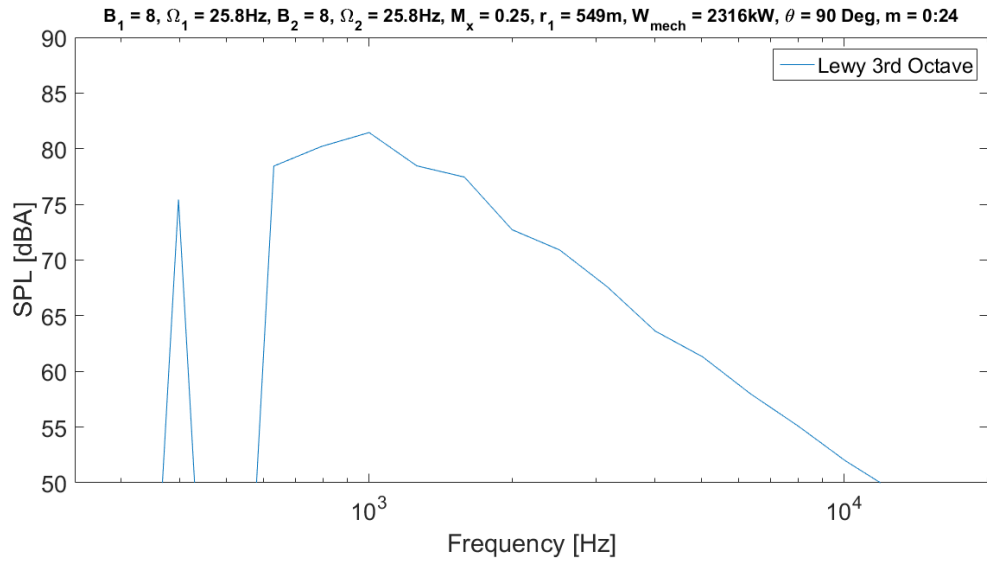


Figure A.2: Display if plot_LowyThirdOctave = 1 in Initiate.m

The 3-D third octave band frequency spectrum based on Lewy is shown in figure A.3. Included are all observer angles given in input.txt.

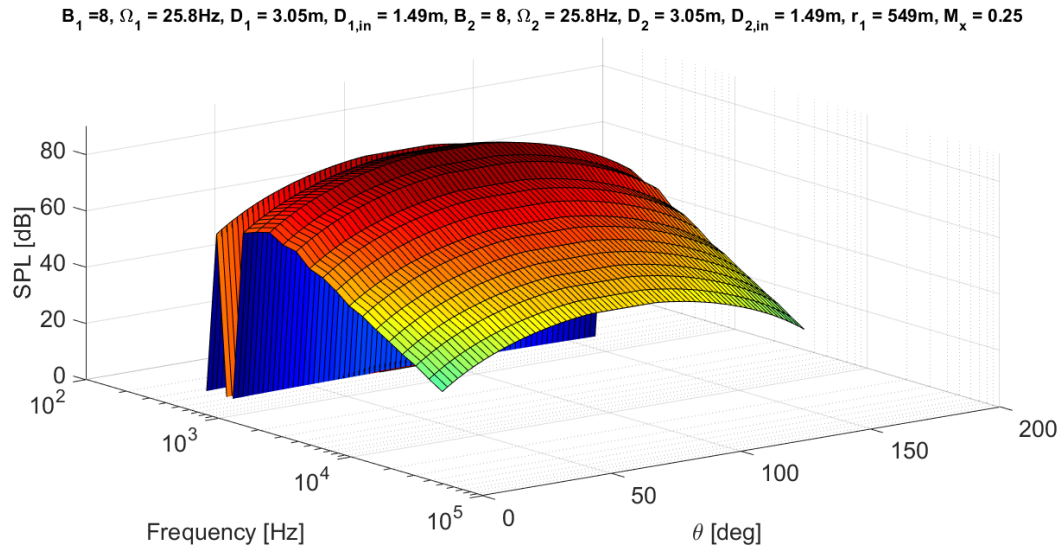


Figure A.3: Display if plot_Lowy3DThirdOctave = 1 in Initiate.m

The tonal directivity is shown in a normalised state and an example is displayed in figure A.4.

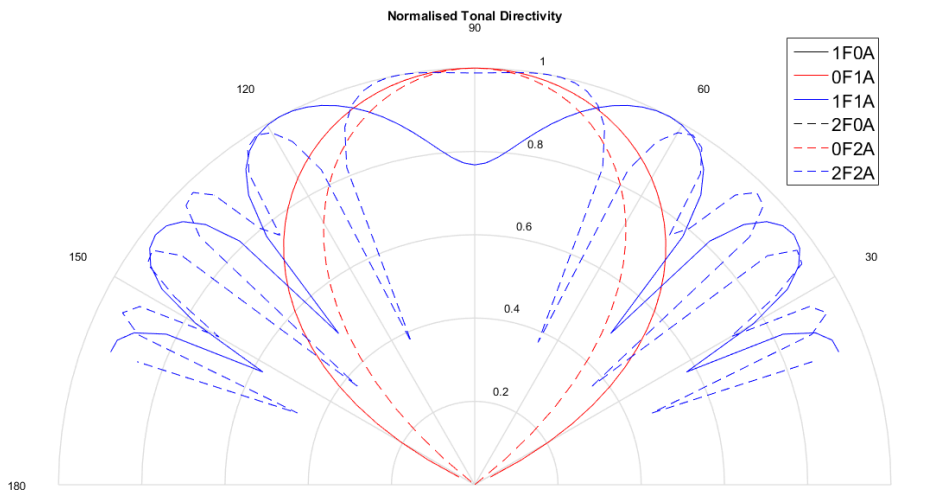


Figure A.4: Display if `plot_tonal_Directivity = 1` in `Initiate.m`

For all combinations of BPF the Bessel Function of First Kind is evaluated. An example is given in figure A.5.

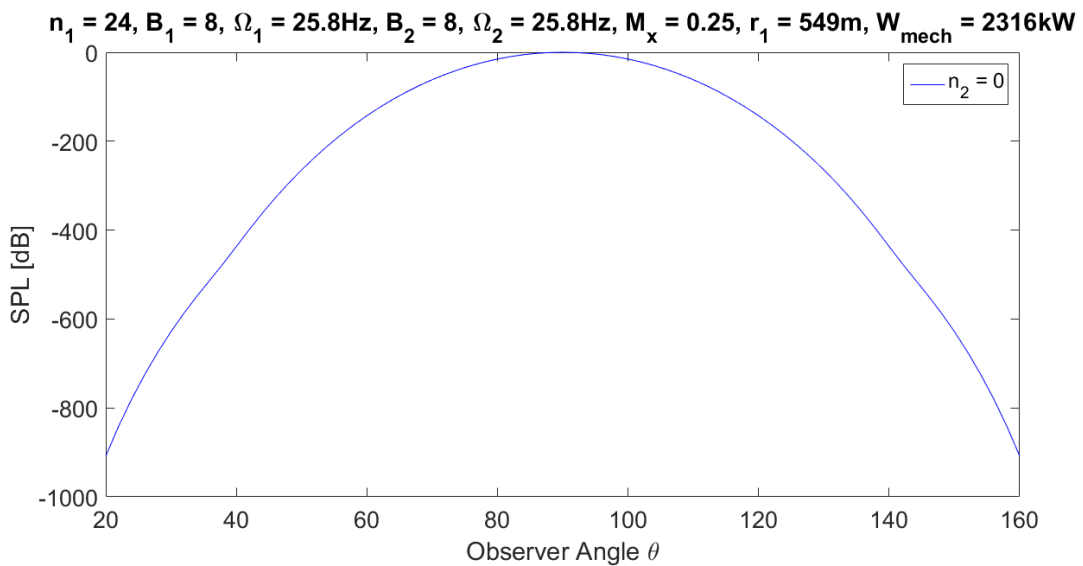


Figure A.5: Example display if `plot_Bessel_Directivity = 1` in `Initiate.m`

Frequency spectra are evaluated for every observer angle demanded. An example for 90° is shown in figure A.6.

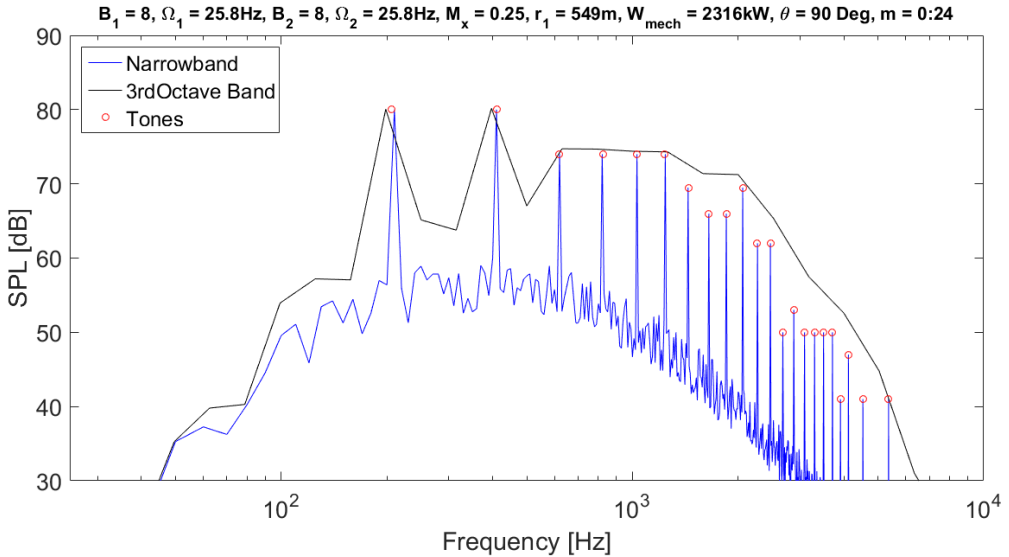


Figure A.6: Display if `plot_Frequency_Spectrum = 1` in `Initiate.m` example of 90°

All evaluated observer angles are contained in the narrowband 3-D plot given in figure A.7.

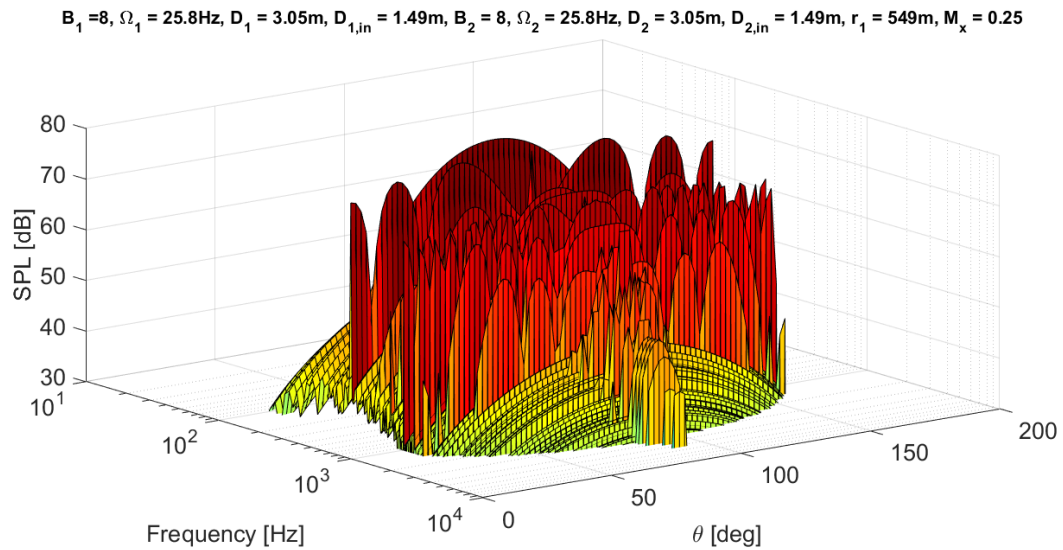


Figure A.7: Display if `plot_PARTNER3D = 1` in `Initiate.m`

Lastly, for an observer angle of 90° only, Lewy third octave frequency spectrum is compared to the tonal noise (figure A.8).

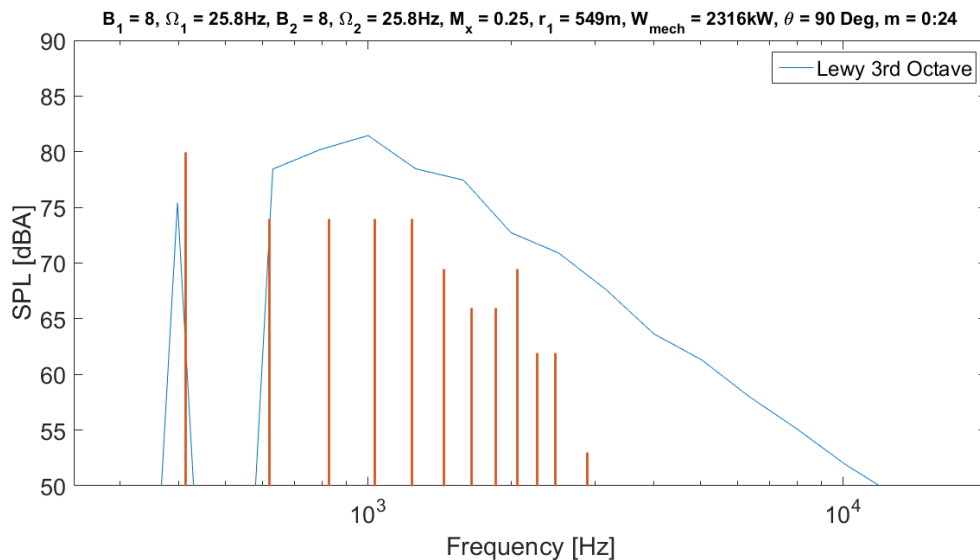


Figure A.8: Display if `plot_PARTNER_Lowy = 1` in `Initiate.m`

A.2 Analytical Tool

The displays are generated for an input of observer angle $\theta = 40 : 5 : 140^\circ$ and $D_{in} = 1.49m$.

The pressure signal is determined for all observer angles demanded. Figures A.9 and A.10 are selected to be presented as examples.

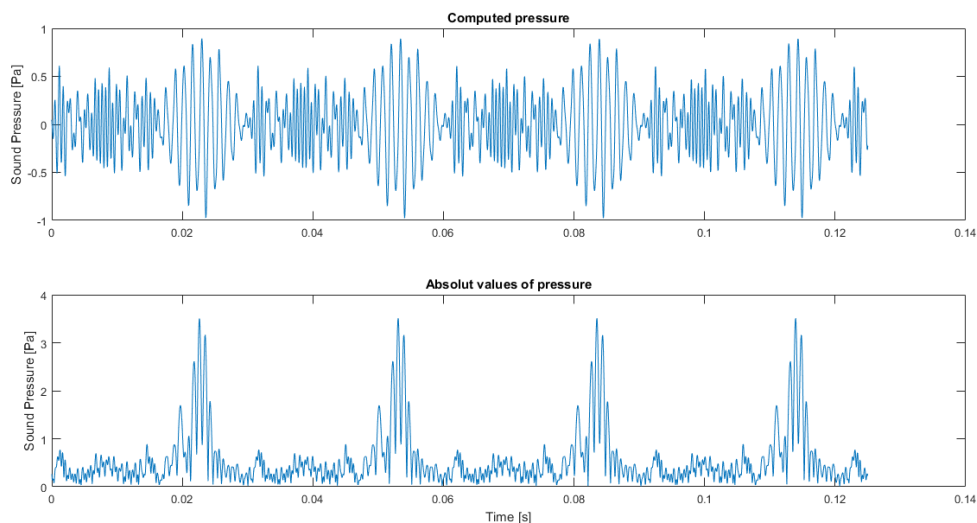


Figure A.9: Display if `plot_PressureSignal = 1` in `Initiate.m` example of 65°

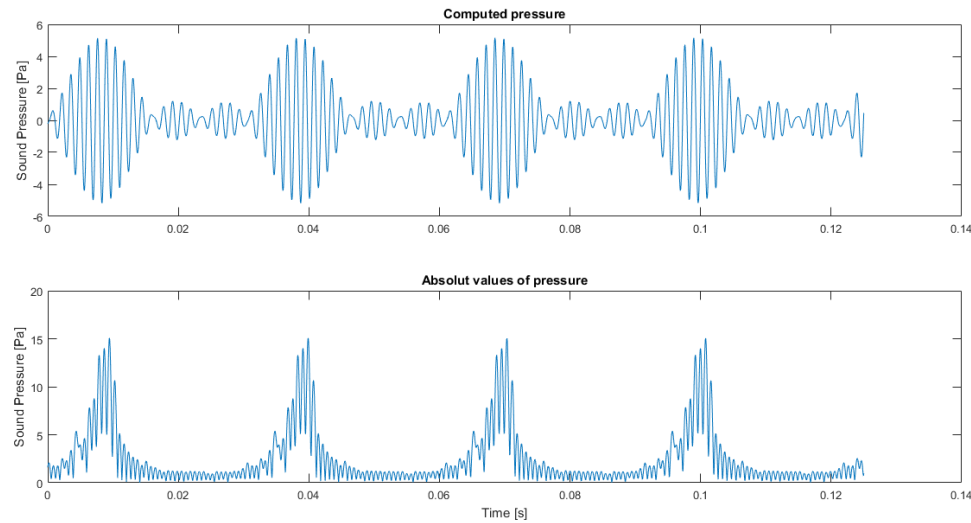


Figure A.10: Display if `plot_PressureSignal = 1` in `Initiate.m` example of 90°

The pressure signal is Fourier transformed. Figures A.11 and A.12 present the FFT from depicted pressure signals.

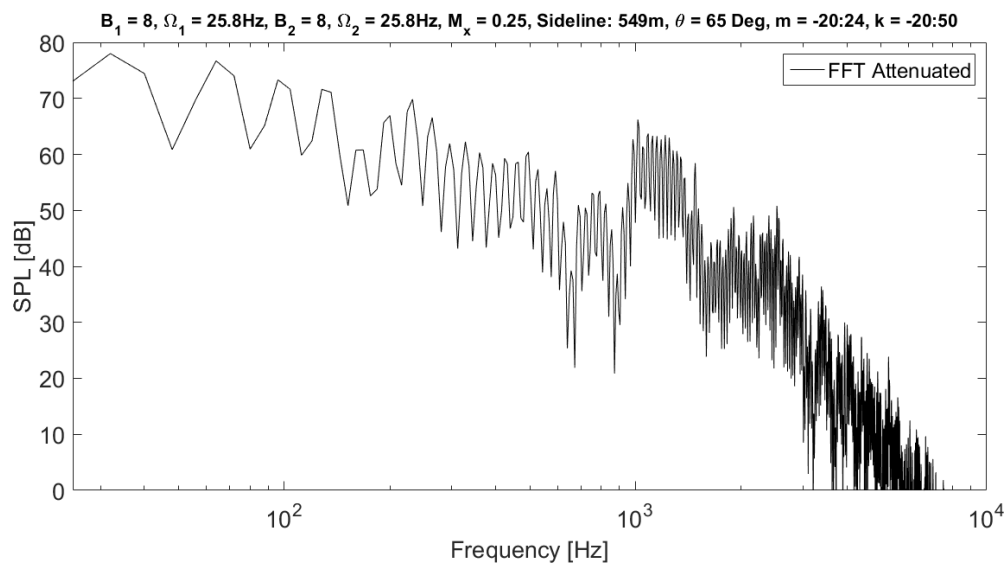


Figure A.11: Display if `plot_FFTattenuated = 1` in `Initiate.m` example of 65°

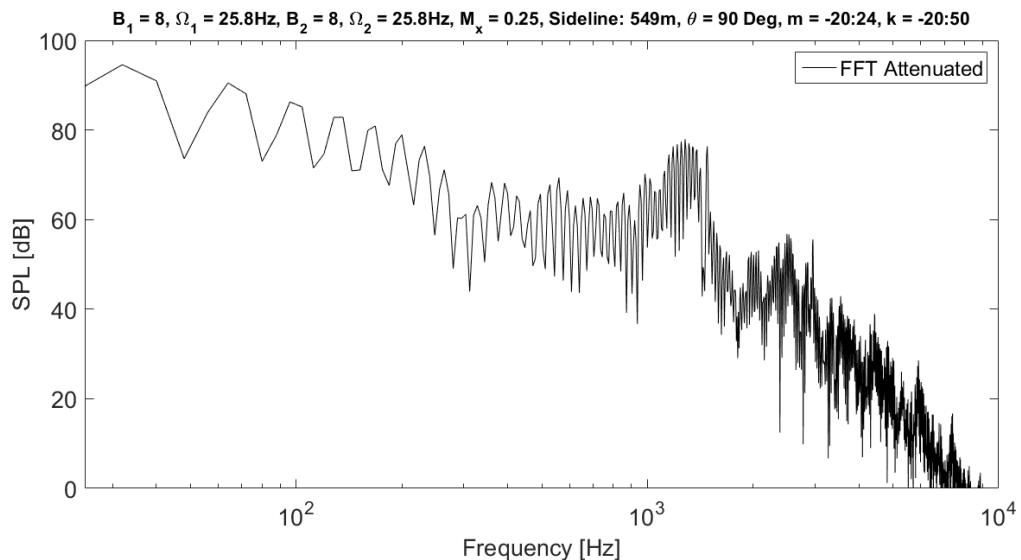


Figure A.12: Display if `plot_FFTattenuated = 1` in `Initiate.m` example of 90°

From FFT the final frequency spectra are obtained. Both spectra are listed displayed in figures A.13 and A.14.

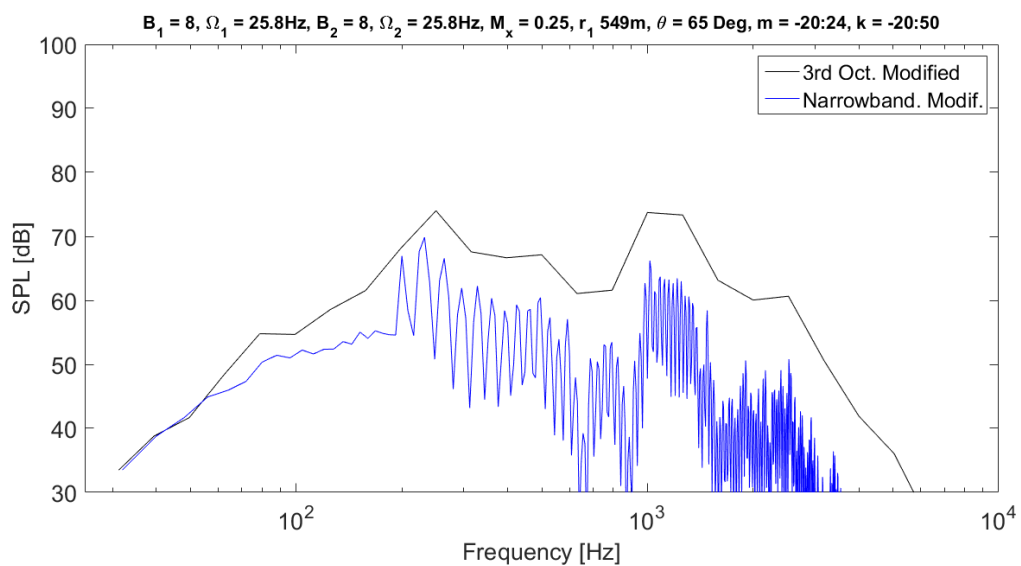


Figure A.13: Display if `plot_FrequencySpectra = 1` in `Initiate.m` example of 65°

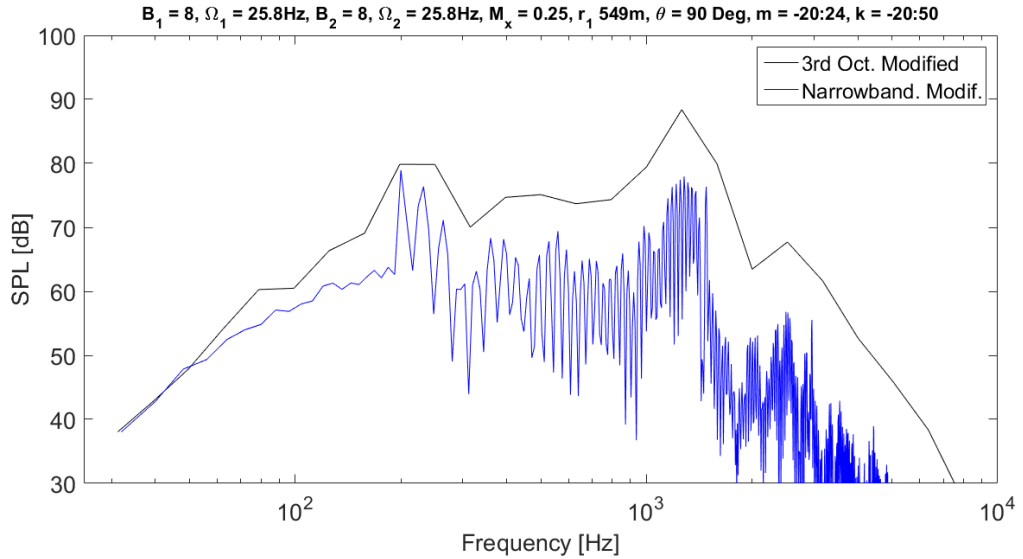


Figure A.14: Display if `plot_FrequencySpectra = 1` in `Initiate.m` example of 90°

For all observer angles of interest, the OSPL is computed. An generic result is shown in A.15.

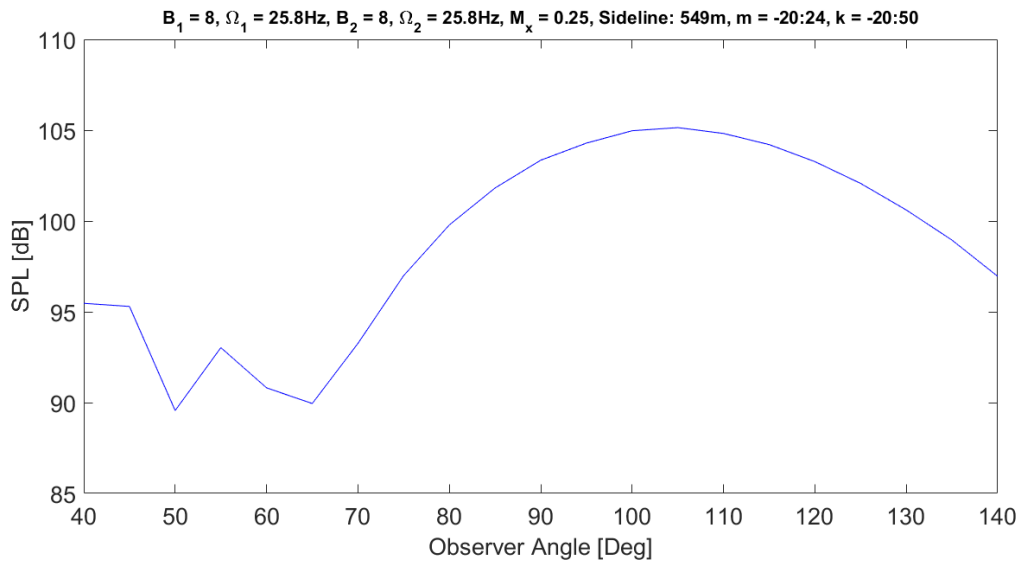


Figure A.15: Display if `plot_Directivity = 1` in `Initiate.m`

Lastly, the frequency Spectra are depicted in a 3-D manner. Narrowband spectra are shown in A.16.

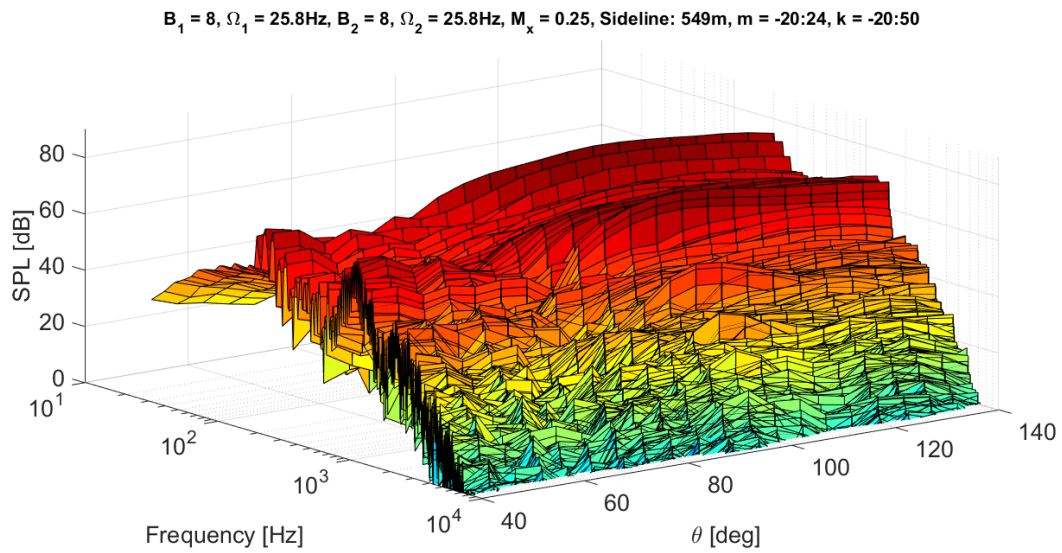


Figure A.16: Display if `plot_3DFrequencySpectrum = 1` in `Initiate.m` example of 90°

Third octave band spectra are contained in figure A.17.

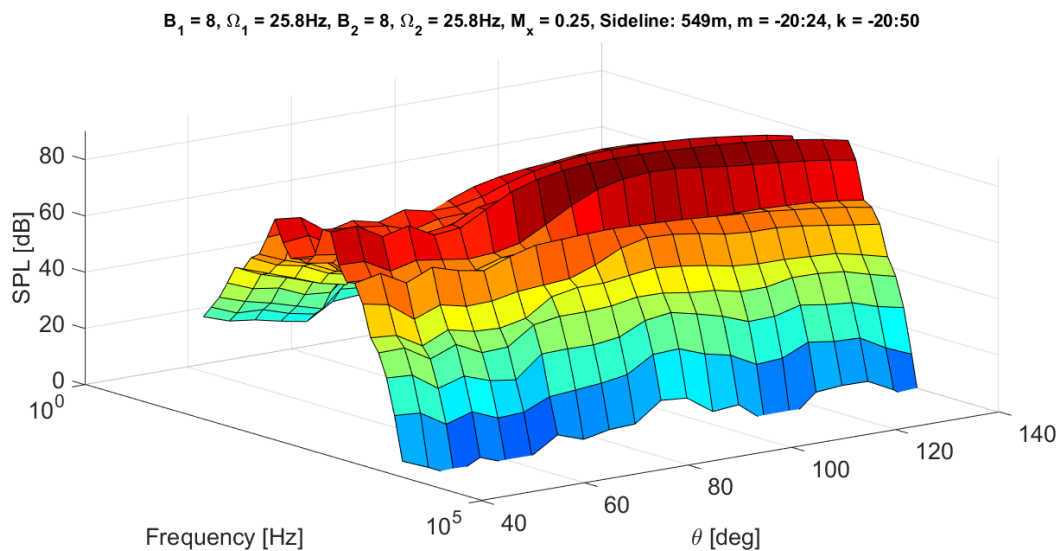


Figure A.17: Display if `plot_3DThirdOctave = 1` in `Initiate.m` example of 65°

B

Supporting Figures

This appendix lists all supporting figures, that are mentioned throughout the report.

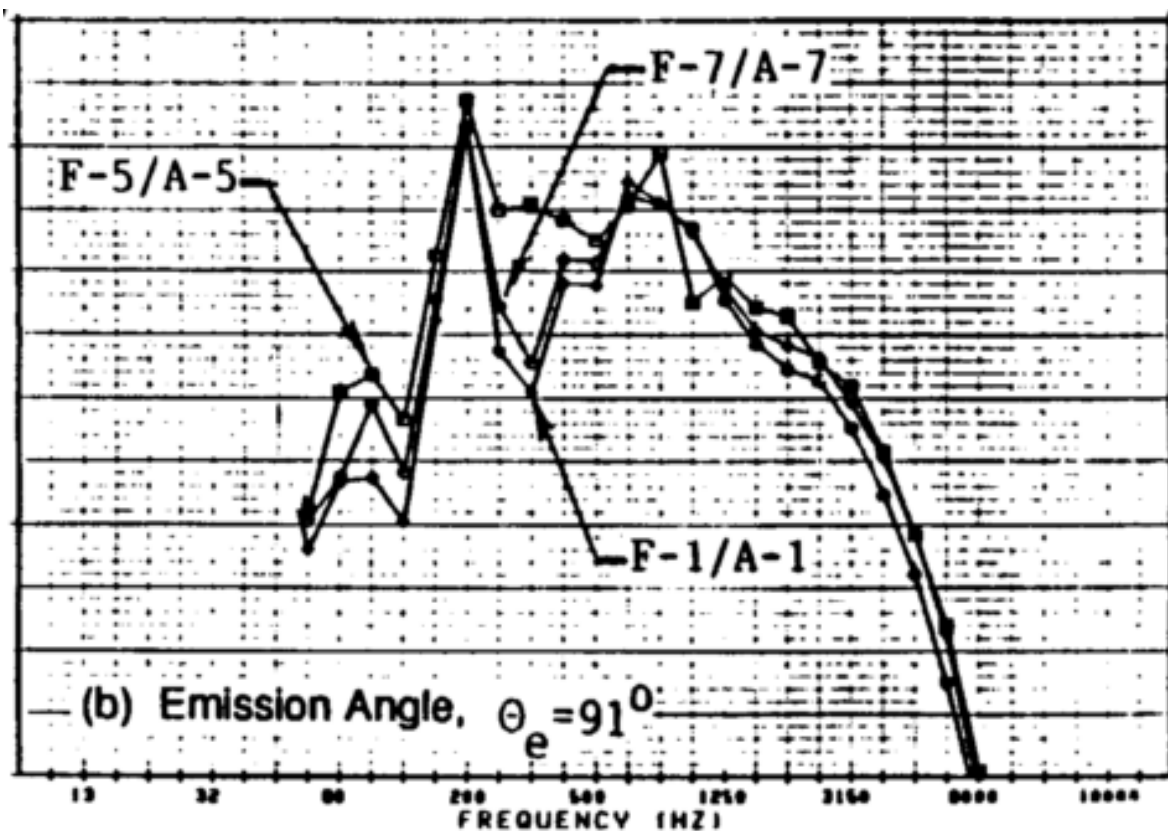


Figure B.1: 1/3-octave band from [22] figure 200 b

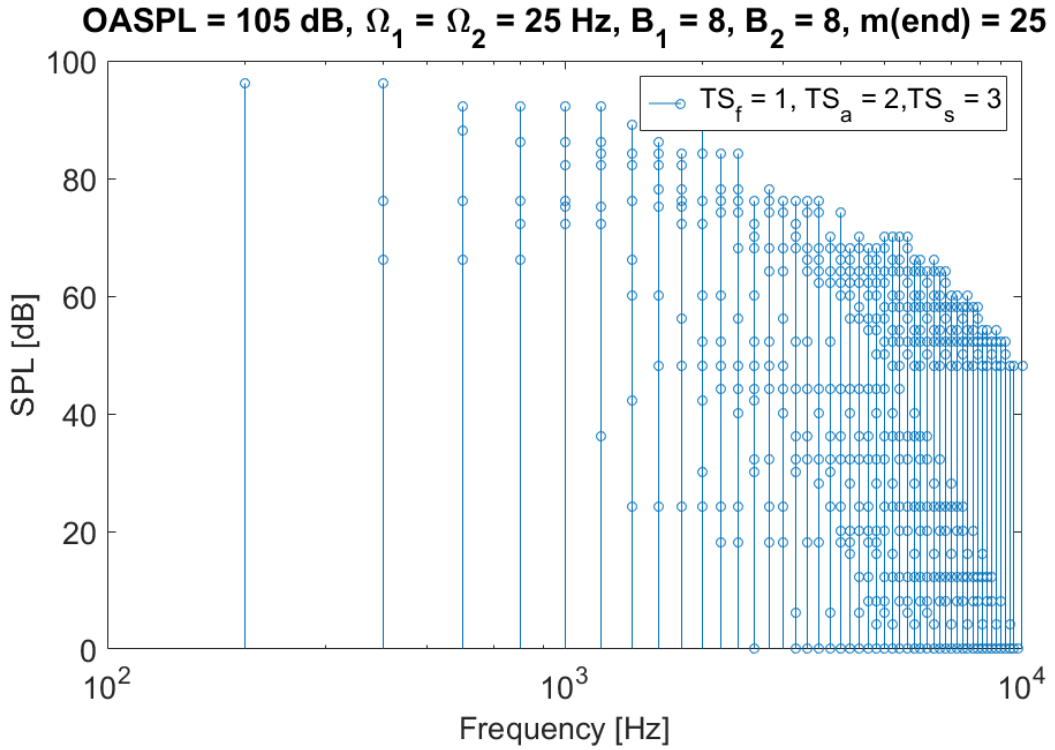


Figure B.2: Tonal noise prediction based on PARTNER for $B_1 = B_2$, $TS_f = 1$, $TS_a = 2$, and $TS_s = 3$

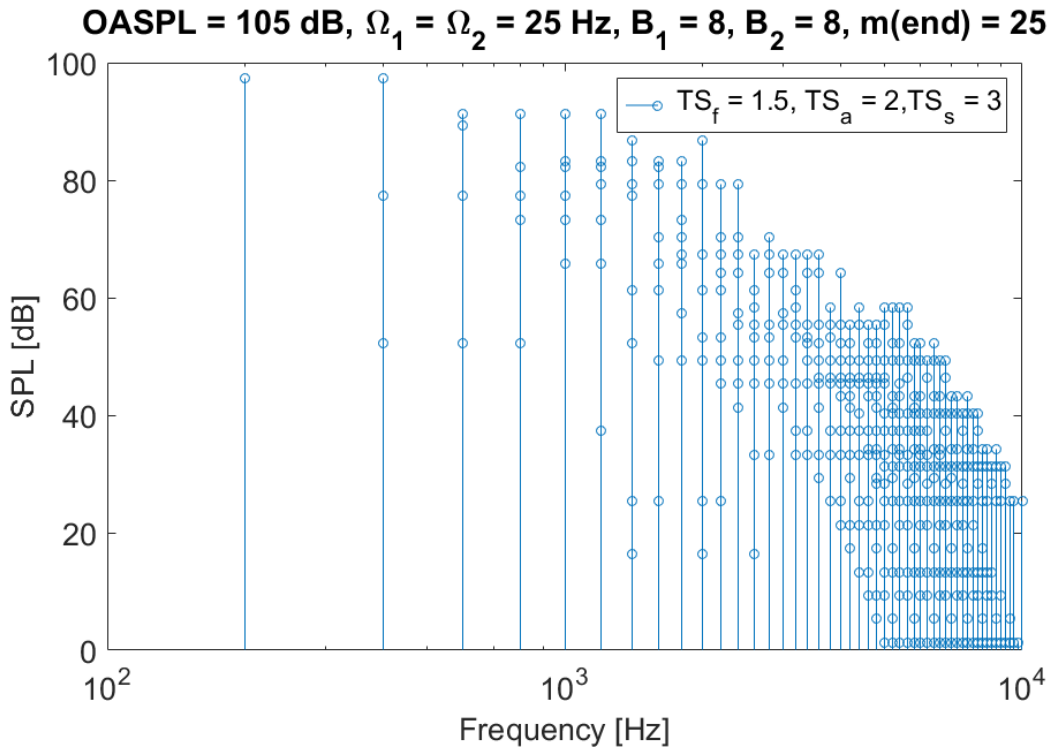


Figure B.3: Tonal noise prediction based on PARTNER for $B_1 = B_2$, $TS_f = 1.5$, $TS_a = 2$, and $TS_s = 3$

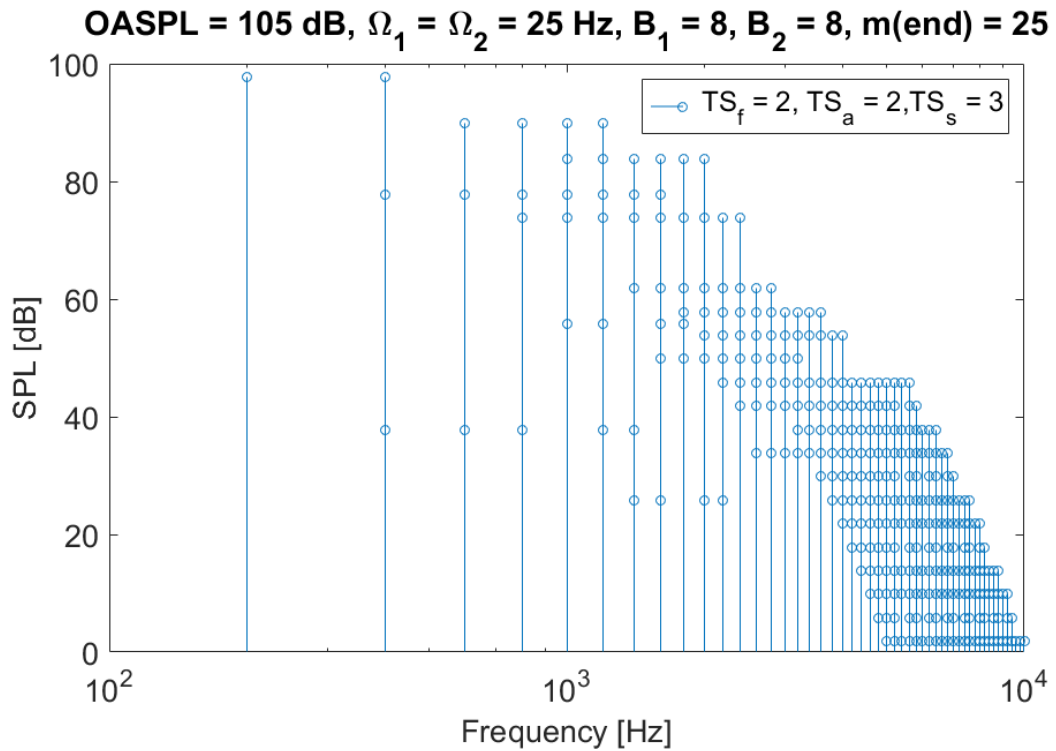


Figure B.4: Tonal noise prediction based on PARTNER for $B_1 = B_2$, $TS_f = 2$, $TS_a = 2$, and $TS_s = 3$

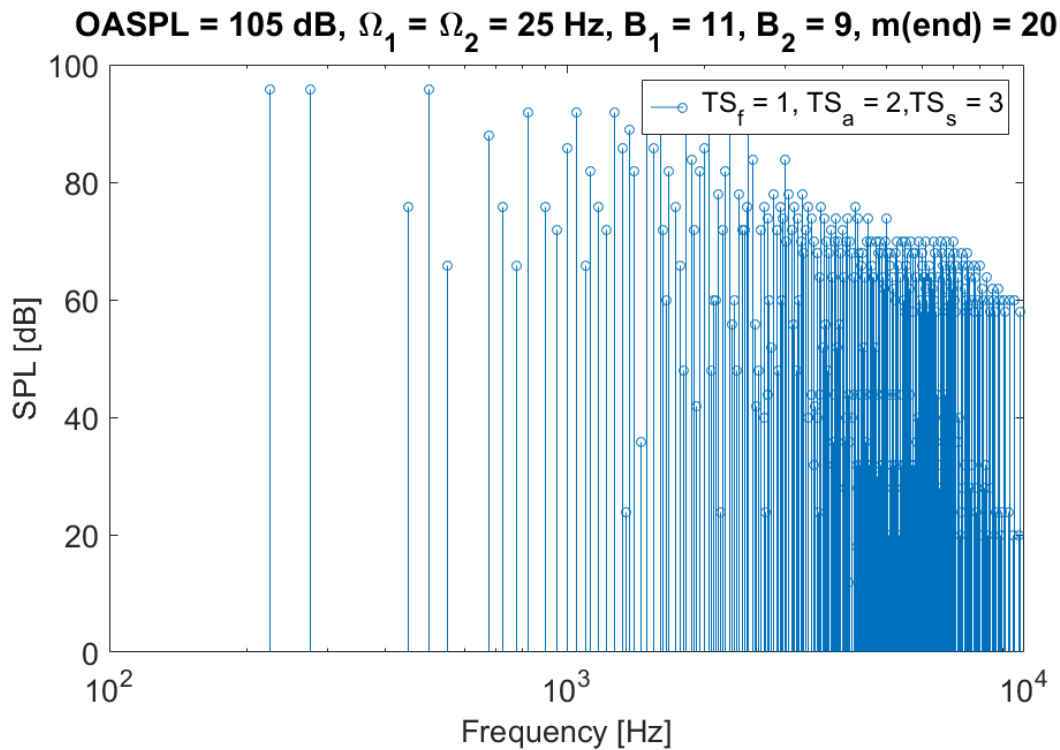


Figure B.5: Tonal noise prediction based on PARTNER for $B_1 = B_2 + 2$, $TS_f = 1$, $TS_a = 2$, and $TS_s = 3$

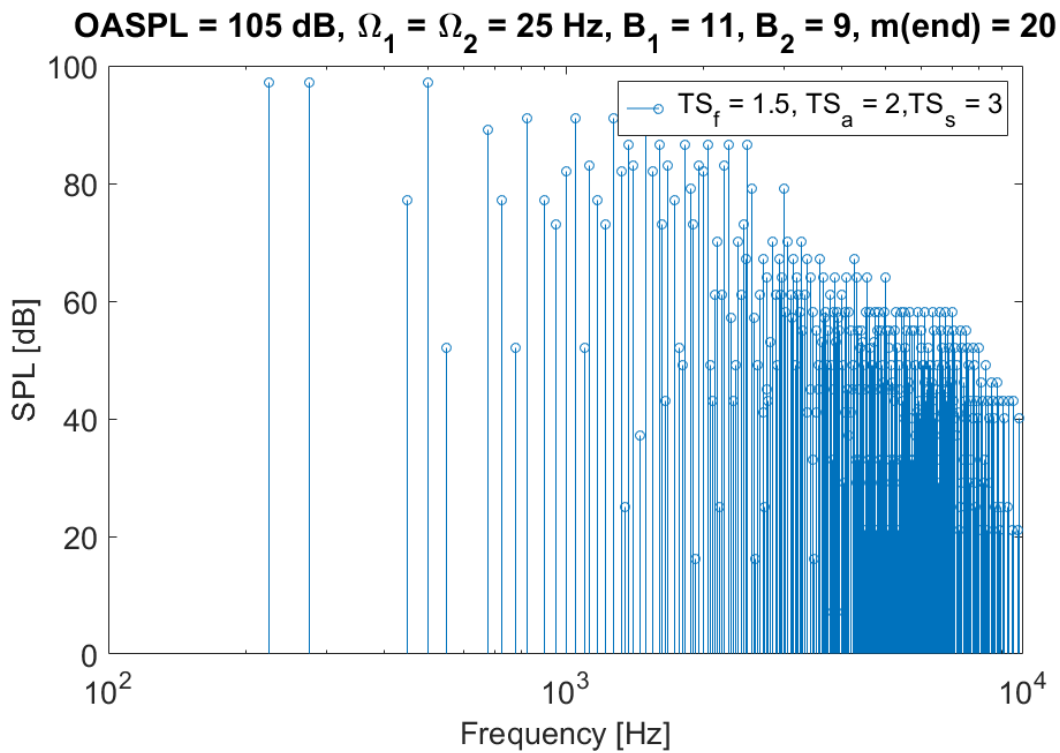


Figure B.6: Tonal noise prediction based on PARTNER for $B_1 = B_2 + 2$, $TS_f = 1.5$, $TS_a = 2$, and $TS_s = 3$

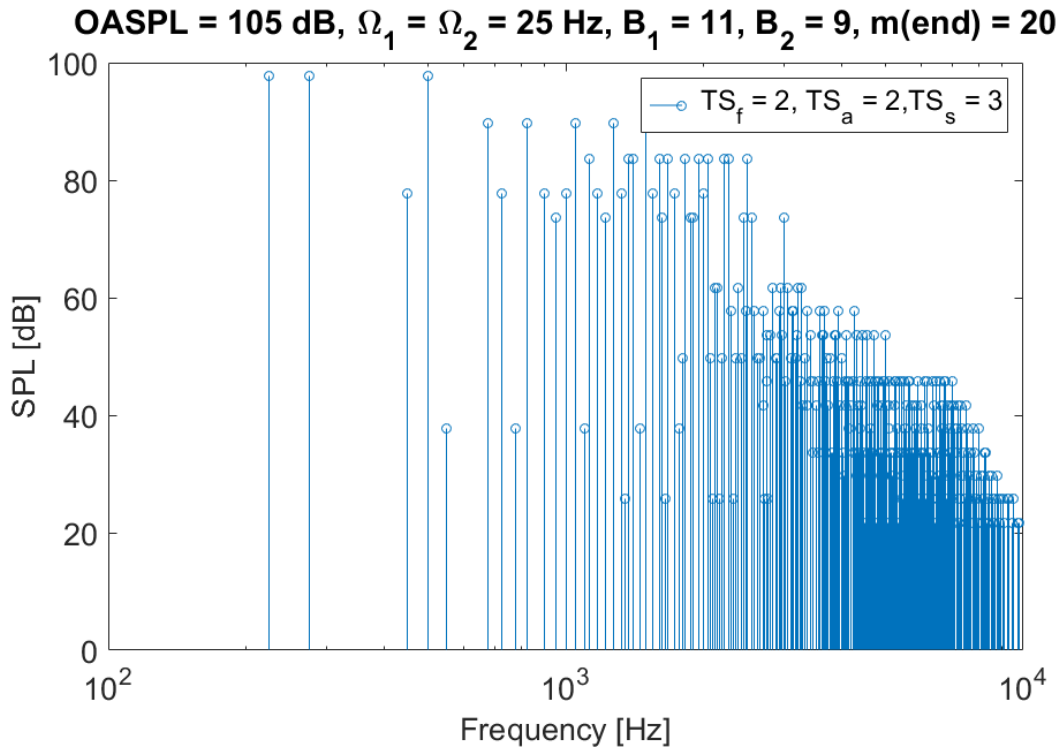


Figure B.7: Tonal noise prediction based on PARTNER for $B_1 = B_2 + 2$, $TS_f = 2$, $TS_a = 2$, and $TS_s = 3$

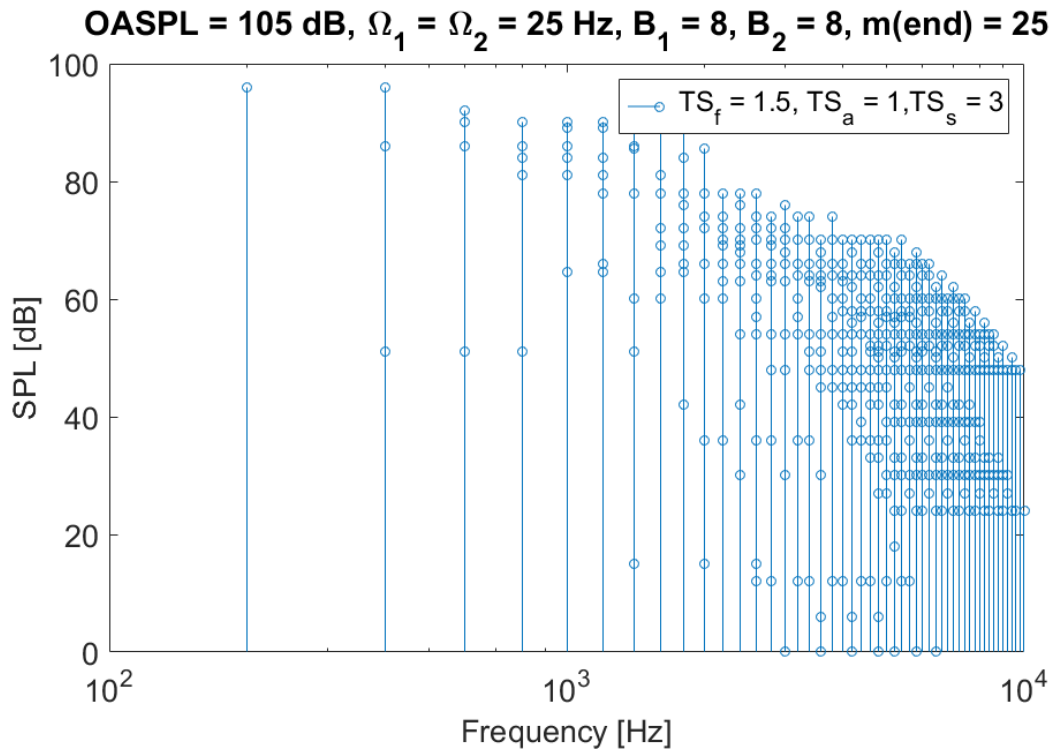


Figure B.8: Tonal noise prediction based on PARTNER for $B_1 = B_2$, $TS_f = 1.5$, $TS_a = 1$, and $TS_s = 3$

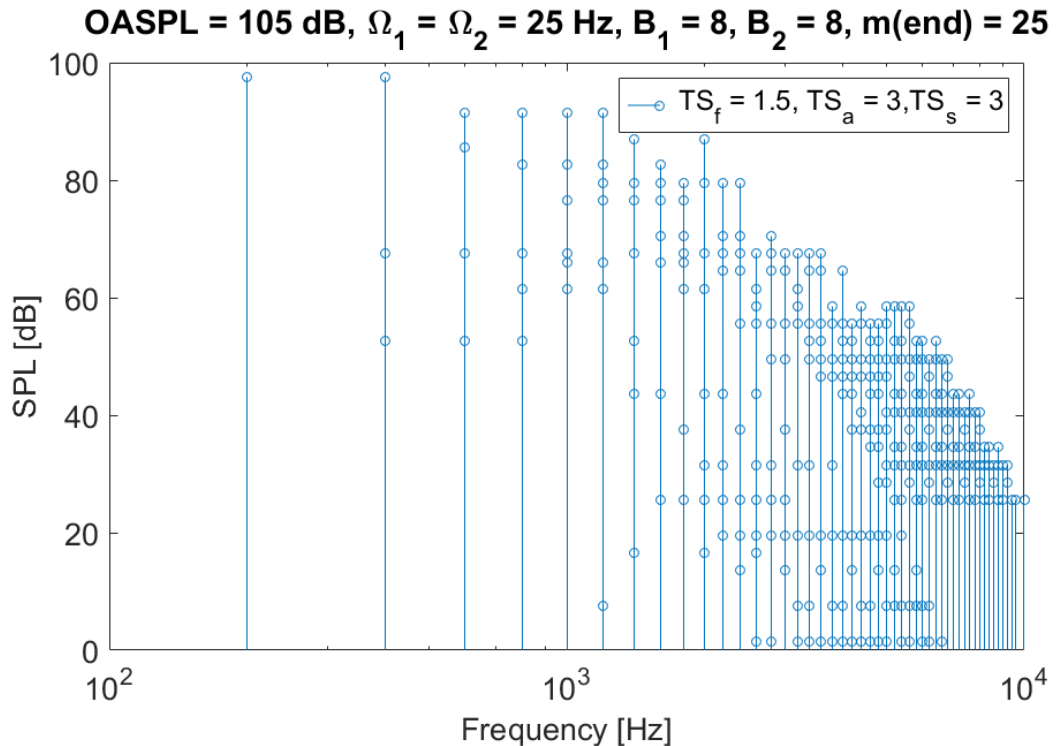


Figure B.9: Tonal noise prediction based on PARTNER for $B_1 = B_2$, $TS_f = 1.5$, $TS_a = 3$, and $TS_s = 3$

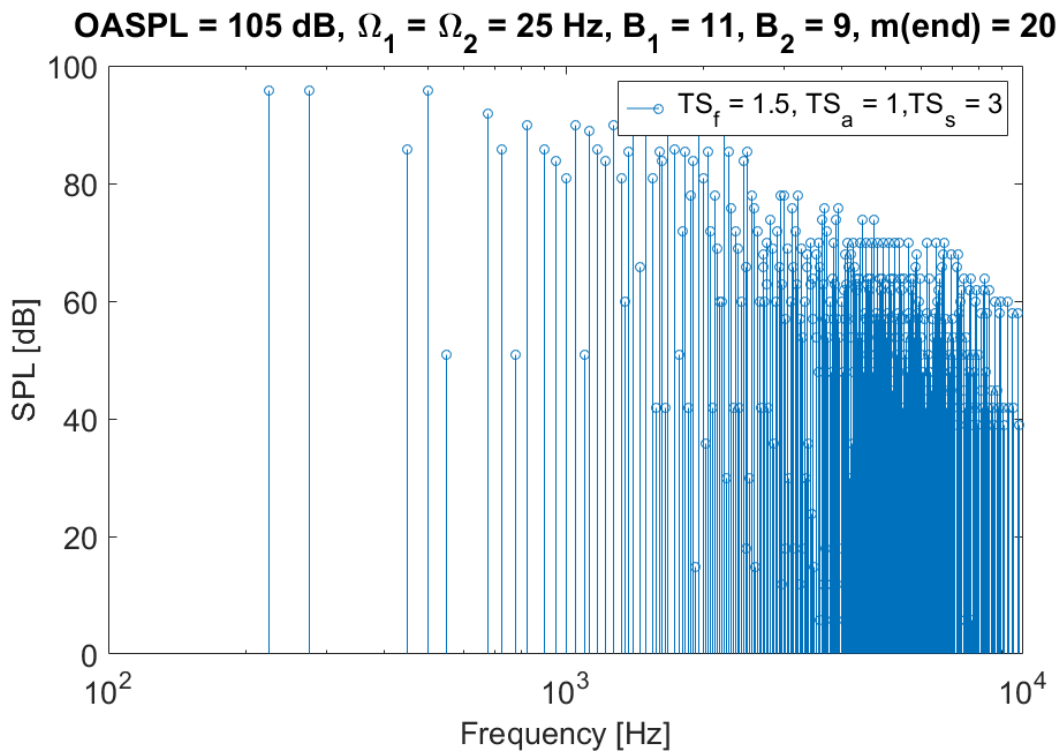


Figure B.10: Tonal noise prediction based on PARTNER for $B_1 = B_2 + 2$, $TS_f = 1.5$, $TS_a = 1$, and $TS_s = 3$

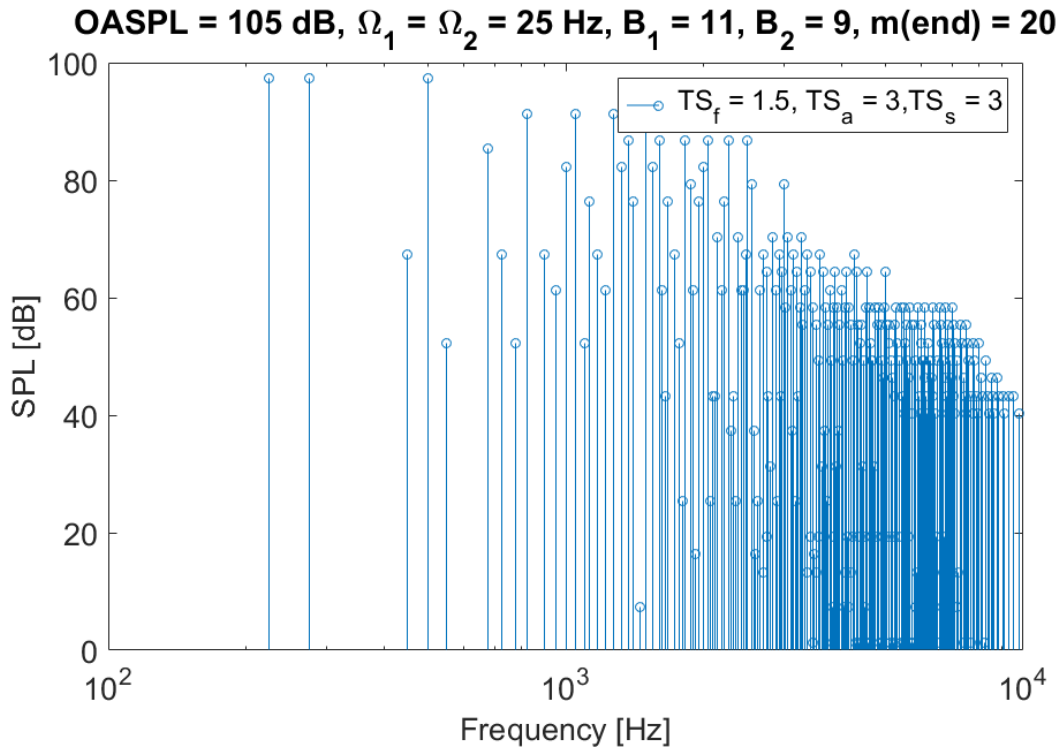


Figure B.11: Tonal noise prediction based on PARTNER for $B_1 = B_2 + 2$, $TS_f = 1.5$, $TS_a = 3$, and $TS_s = 3$

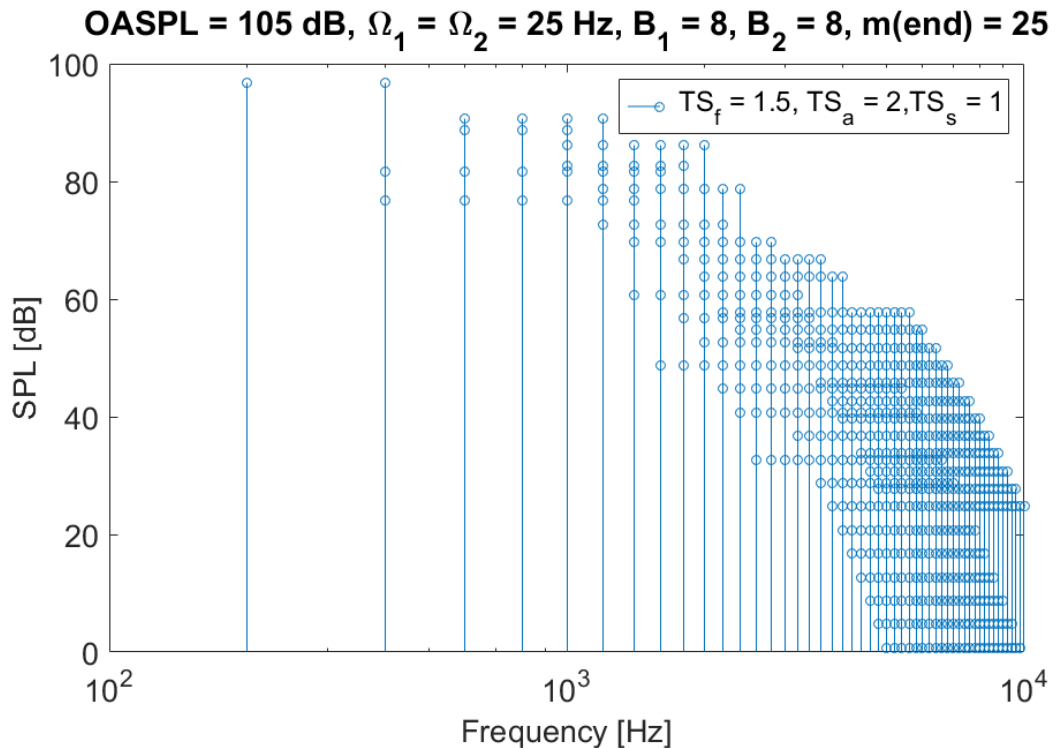


Figure B.12: Tonal noise prediction based on PARTNER for $B_1 = B_2$, $TS_f = 1.5$, $TS_a = 2$, and $TS_s = 1$

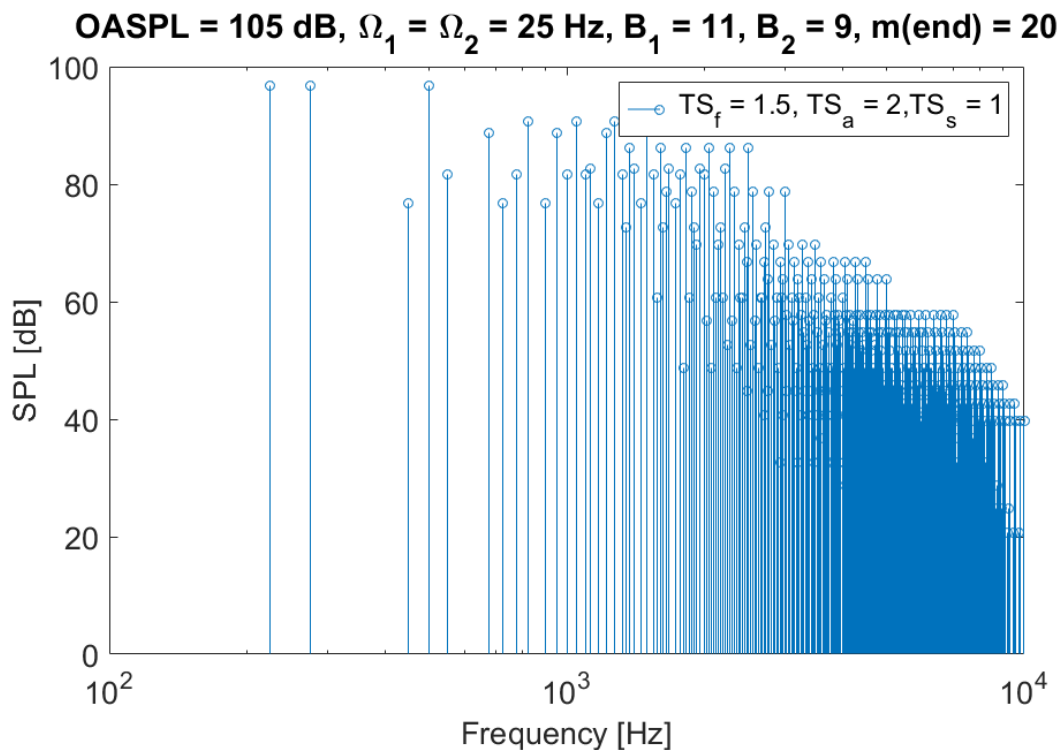


Figure B.13: Tonal noise prediction based on PARTNER for $B_1 = B_2$, $TS_f = 1.5$, $TS_a = 2$, and $TS_s = 1$